General Disclaimer

One or more of the Following Statements may affect this Document

- This document has been reproduced from the best copy furnished by the organizational source. It is being released in the interest of making available as much information as possible.

- This document may contain data, which exceeds the sheet parameters. It was furnished in this condition by the organizational source and is the best copy available.

- This document may contain tone-on-tone or color graphs, charts and/or pictures, which have been reproduced in black and white.

- This document is paginated as submitted by the original source.

- Portions of this document are not fully legible due to the historical nature of some of the material. However, it is the best reproduction available from the original submission.

EXPERIMENTAL HYPERVELOCITY IMPACT RESEARCH PROGRAM

Final Report

July 1966 - December 1967

by

Jerome Jeslis

May 1968

Prepared under Contract NAS8-20337 by

IIT Research Institute
Chicago, Illinois

for

George C. Marshall Space Flight Center
Huntsville, Alabama

ABSTRACT

A series of hypervelocity impact experiments was conducted using the light gas gun facilities at IITRI. The program was conducted in three separate phases; one dealing with microparticle impacts, one with measurement of dynamic deformation in single-plate targets above and below the ballistic limit, and one covering measurement of impact-produced radiation in a reduced atmosphere. All the test data and observations for each phase are included in separate sections of this report since each series is independent of the other.

CONTENTS

ILLUSTRATIONS

ILLUSTRATIONS (Continued)

ILLUSTRATIONS (Continued)

TABLES

TABLES (Continued)

EXPERIMENTAL HYPERVELOCITY IMPACT RESEARCH PROGRAM

SUMMARY

The general purpose of the program was to measure various physical phenomena associated with the hypervelocity impact process. The program covered a very broad spectrum of measurements and, for convenience, was divided into three phases.

In Phase I the threshold velocity for various sized borosilicate microspheres (20 to 260 microns) was determined for various aluminum and stainless steel Pegasus targets. Essentially the highest velocity with no penetration and the lowest velocity with penetration were determined for selected ball size and target combinations.

Phase II determined dynamic deformation on the rear surface of aluminum targets. In these experiments the mass of the aluminum projectile and its velocity was held constant (within the limits of the launcher) and the target thickness was varied. A range of conditions from penetration through spall and below the spallation limit was examined. Measurements on the back-face of the targets were made with sequential flash X-rays and optical lever techniques.

In Phase III, a series of measurements was made for flat impacts of a disk-type projectile. Included were sequential flash X-rays of the bubble on the back face of the target and image-converter pictures of the bubble, both self-illuminated and back lighted. In a special high-vacuum target chamber, measurements of the following were made: the charge on the projectile prior to impact (in range vacuum); the ionization charge of the fragment bubble off the back face of the target; the total integraced light; and certain other spectral bands of radiation.

INTRODUCTION

A series of hypervelocity impact experiments was conducted using the light gas gun facilities at IITRI. The program was conducted in three separate phases; one dealing with microparticle impacts, one with measurement of dynamic deformation in single-plate targets above and below the ballistic limit, and one covering measurement of impact-produced radiation in a reduced atmosphere. All the test data and observations for each phase are included in separate sections of this report since each series is independent of the other.

TECHNICAL DISCUSSION

Phase I Microsphere Experiments

The objective of Phase I was to conduct a series of experimental light-gas gun firings of various borosilicate micron-sized spheres against various aluminum (Pegasus 2024T3) and stainless steel (Type 304) targets. Table I shows the range of sphere sizes and target combinations for these experiments. For each of the seven combinations listed in the table the lowest velocity that would result in penetration of the target and the highest velocity that would not penetrate the target were to be determined. Essentially the threshold velocity for each of the combinations was to be determined. Table I also lists the expected range of velocities for each combination.

In previous studies, 380-μ-diam borosilicate spheres were fired successfully. Velocities up to 22,000 fps were obtained with .22-caliber sabot-launched projectiles. Launch techniques based on this previous experience were used for the microsphere experiments.

Before the firings could be conducted, it was necessary to:

(1) obtain adequate supplied of borosilicate spheres,

(2) select and grade microspheres for each of the five sizes selected,

(3) develop techniques for loading the smaller spheres into the sabot that minimize ball breakup during launch, and

(4) develop instrumentation methods to determine ball velocity.

These tasks were undertaken simultaneously during preliminary firing tests. Experimental firings were then made. First, at the higher velocity to determine that penetration could be made within the capabilities of .22-caliber light-gas gun; then, for the targets in which penetration was obtained, firing conditions were changed to lower the velocity to ensure no penetration. Velocity was varied between these limits to establish the actual threshold velocity.

TABLE I

SPHERE/TARGET COMBINATION REQUIREMENTS FOR MICROSPHERE FIRINGS

Combination	Sphere	Target	Expected Velocity Range, (10^3 fps)
1	50-μ-diam borosilicate	2-mil stainless steel	15 - 20
2	50-μ-diam borosilicate	1.5-mil Pegasus*	12 - 18
3	50-μ-diam borosilicate	1-mil stainless steel	8 - 15
4	40-μ-diam borosilicate	1-mil stainless steel	15 - 22
5	20-μ-diam borosilicate	1-mil stainless steel	20 - 25
6	130-μ-diam borosilicate	8-mil Pegasus*	10 - 22
7	260-μ-diam borosilicate	16-mil Pegasus*	10 - 22

*Only the outer skin of 2024T3 aluminum for Pegasus targets is to be considered in the penetration study.

Selection and Grading of Microspheres. Samples of glass spheres in the approximate size ranges were supplied by Micro Beads Incorporated. These spheres as received were a mixture of size ranges composed of hollow spheres, solid spheres, and fragments, as well as of quasispherical shapes. The object of the classification was to obtain a selected number of solid spheres within a specified size range. The initial size requirements were

100 balls:	260-μ	$\pm$ 10-μ
100 balls:	130-μ	$\pm$ 10-μ
300 balls:	50-μ	$\pm$ 5-μ
100 balls:	30-μ	$\pm$ 2-μ
100 balls:	20-μ	$\pm$ 2-μ

The samples were initially classified to eliminate the obvious nonspherical particles. Spheres of approximate size were carefully rolled back and forth in a petri dish. The solid spherical particles usually collected at one end of the dish much faster than the fragments and nonspherical particles. Observation of the particles under a microscope by simultaneous transmitted light and reflected side lighting indicated whether the particles were solid or hollow.

The 260-μ spheres were then transferred under the microscope and observed one at a time. The spheres that were symmetrical, solid, and within the specified size range were carefully transferred to a vial using a finely tipped tweezer.

The 130-μ spheres were also selected individually, using the same procedure. Later, a sieving method was used to obtain a greater number of spheres.

The 50-μ spheres were also selected individually. However, 300 50-μ balls are negligible in mass for adequate transfer from the vial to sabot. Therefore, a sieving method was initiated. A sample fraction was obtained of spheres that passed through a standard 270 mesh sieve (53-μ), and were retained on the 400 nickel mesh sieve (48.6-μ). The fraction on the 400 sieve was then tapped to plug as many openings as possible. The spheres that remained in the opening were then removed by more vigorous tapping and saved.

A sieving method for 30-μ spheres was complicated by the fact that sieve material of the desired 30-μ was not available. Instead micromesh sieves were used to obtain the fraction that passed through the 39.6-μ sieve but did not pass through the 36.0-μ sieve.

Micromesh sieves were also used to obtain the 20-μ spheres. The spheres that passed through a 21.6-μ sieve but were retained on the 18-μ sieve were saved. Polaroid pictures of the size fractions from the samples are shown in Figure 1. For the subsieve ranges (less than standard 325 mesh (44-μ)) a sieve material called electromesh or micromesh was used. This micromesh material is specially made by electrodeposition on a master sieve and results in a uniform opening without the usual twist-and-turn of regular sieve material. The desired size fraction can be obtained from two closely size microsized mesh materials. To obtain a more uniform product, a technique of purposely plugging the opening of a micromesh sieve was used. The more spherical balls would fit into the square openings and lodge quite snugly at four points corresponding to the sides of the opening. An extra sharp tap results in balls of similar size dropping out to be collected. This technique offers potential for future studies. The micromesh material (Cu or Ni) with spheres held in the openings could be selectively dissolved, either chemically or electrolytically, and the undissolved balls then collected on a membrane-type filter. Figure 1(f) shows a micromesh sieve with a few glass spheres attached to the opening.

Sabot and Sphere Loading. - Previous experience has shown that multiple loading of projectiles with diameters of 1/32 inch and less is practical for sabot launching in the light-gas gun. In addition, it was essential that the loading be made in a single layer, to prevent projectile damage or break-up during launch. Figure 2 illustrates the action of the sabot and spheres with the multilaunch technique. Before loading the balls, a thin film of light oil was placed on the flat surface of the sabot counterbore. The 260- and 130-μ spheres were individually hand-loaded into the counterbore and retained by the oil film. Handling spheres of 50-μ or smaller diameters in this manner proved impractical, hence these were loaded by a simple transfer method. A 0.050-in. diameter (diameter of counterbore) rod was ground square and polished. Wiping this end with a finger left enough oil on the surface to permit picking up the micron spheres. When the end of the rod was coated with a layer of spheres it was inserted into the cavity of the sabot. The relatively thicker oil film on the sabot then retained most of the spheres when the rod was removed. It is reasonable to assume that the minute amount of oil on the sphere is burned off in the flight down the range, or, at least, the mass of the oil is insignificant when the ball impacts the target.

As illustrated in Figure 2, the balls lagged behind the sabot and were dispersed along the centerline of the range. The poor ballistic density of the microspheres caused this,

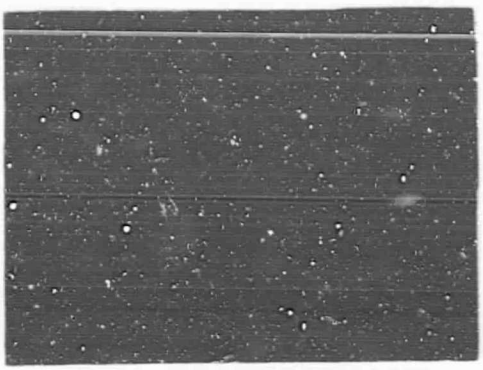

Mag: 120X

(a) 260-μ-diam Spheres

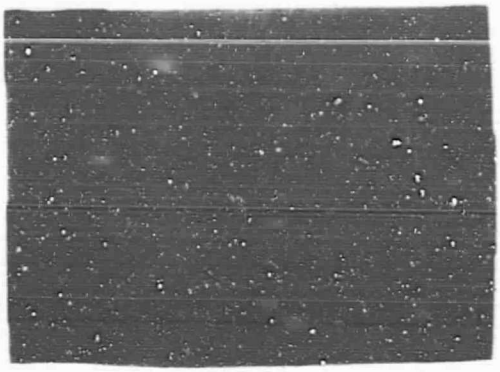

Mag: 100X

(b) 130-μ-diam Spheres

Mag: 100X

(c) 48.6-μ-diam Spheres

Mag: 100X

(d) 39-6-μ-diam Spheres

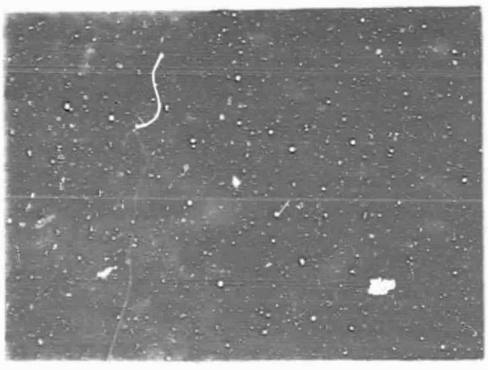

Mag: 100X

(e) 21.6-μ-diam Spheres

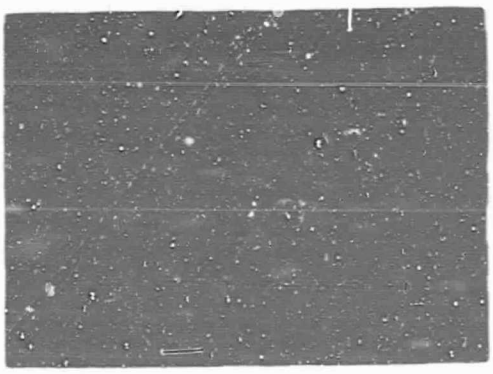

Mag: 100X

(f) 39.6-μ-diam Spheres in Micromesh Sieve

Figure 1 Typical Borosilicate Projectiles after Screening

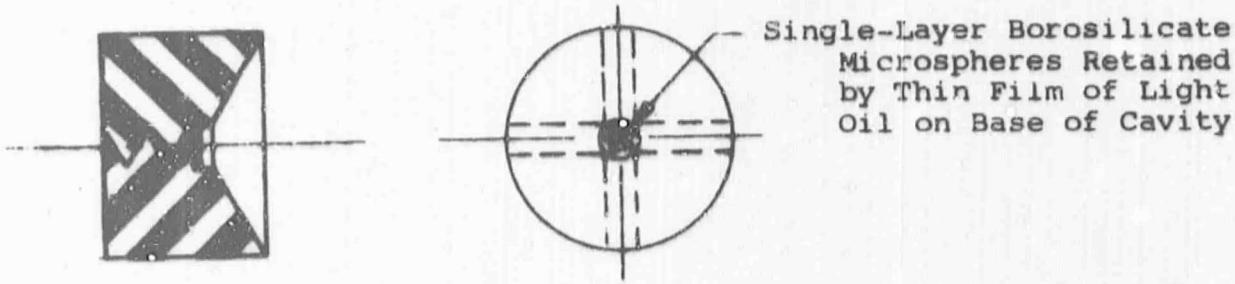

Sabot Consists of Four Separated Serrated Sections

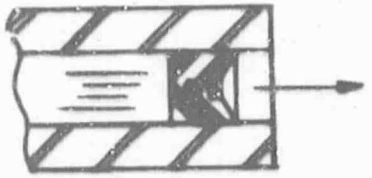

Sabot Has Two Main Functions:

1) It acts as an obturator while carrying the projectiles down the launch tube, and
2) Protects projectile from Erosive Gases

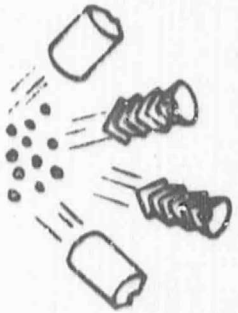

Sabot Separates from Projectiles. Note: Smaller Projectiles Lag Further behind Sabot

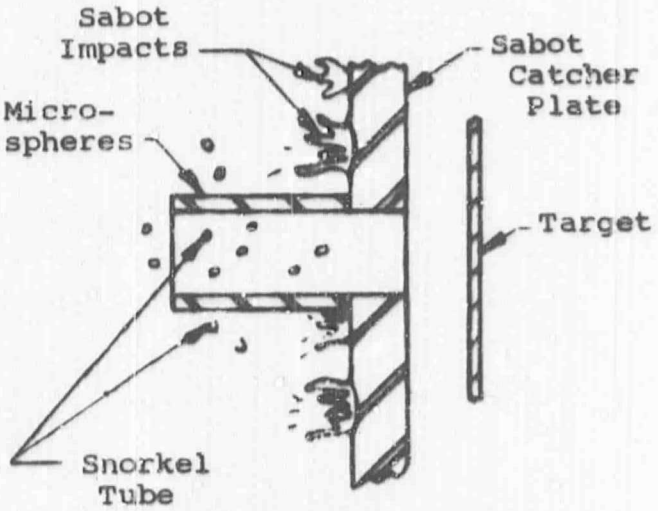

Sabot Impact on Catcher Plate. Note: Some Spheres Pass through Snorkel and Impact on Target

Figure 2 Sabot Launch of Multiple Microspheres

with the result that the sabots impacted the catcher plate ahead of the spheres. The ejection from the sabot impacts formed a screen of particles which intercepted the spheres. This resulted in ball breakup and few, if any, spheres survived to impact intact on the target. This problem was overcome by the addition of a snorkel tube on the catcher plate. The snorkel tube, extending up the range, provided a protective shield through which the balls could pass, without danger of interaction with the particles generated from the sabot impact.

This technique was successful in obtaining clean ball impacts on the target. Some shots were lost, however, when an odd or poor separation of the sabot took place. This caused the sabot to enter, or impact on the end of, the snorkel tube, which resulted in ball breakup and heavy debris impact on the target.

Range and Launcher. - The hypervelocity range facility and launcher are shown schematically in Figure 3. The launcher was an accelerated reservoir-type light-gas gun consisting of a gun powder chamber, a 20mm pump section, a high-pressure section and a smoothbore .22-caliber launch tube.

The range section had three basic components; a blast tank, a range section, and a target chamber. The blast tank served to expand the gun gases following the projectile and provided space for aerodynmaic separation of sabot sections. The range section was equipped with regularly spaced viewing stations at which were located the velocity detectors and image converters. The target chamber contained the sabot catcher target and was equipped with ports for measuring the ball velocity.

Instrumentation. - The basic instrumentation used for these firings is shown schematically in Figure 4. The system employed five photomultiplier tube detectors to measure the flight time between fixed stations for the calculation of sabot and ball velocity. A pair of image converters was employed for verification of the sabot velocity. Photographs made with the image converter do not resulve projectiles much smaller than 1/64-in. diameter, thus direct verification of ball velocity for the very small sizes could not be made. For these firings, the range was evacuated to 400-μ, which was sufficient to render the Zelux sabot sections luminous as they travel past the detector stations. The photomultipliers at A, B, and C were triggered by this signal.

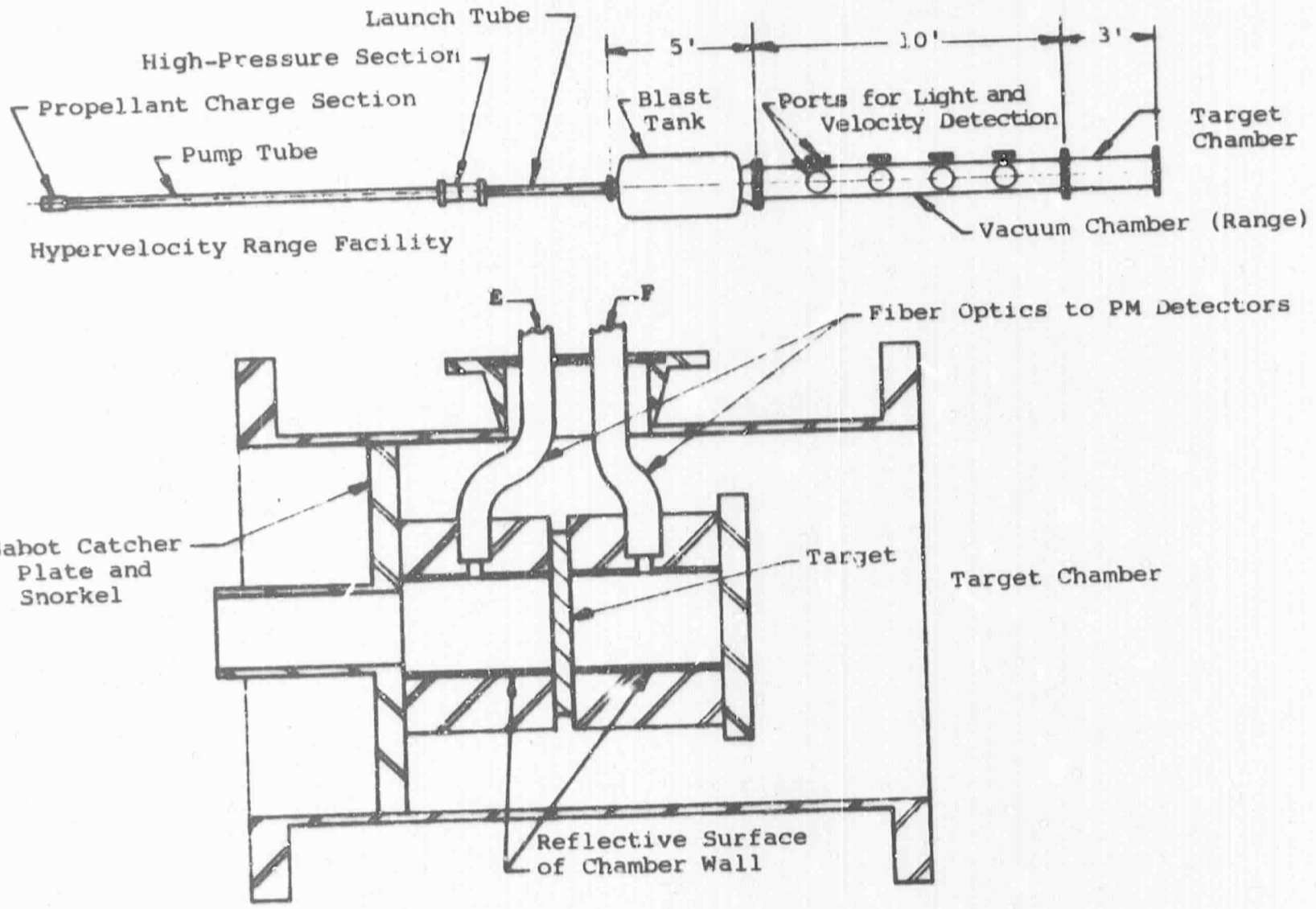

Figure 3 Hypervelocity Range and Target Chamber

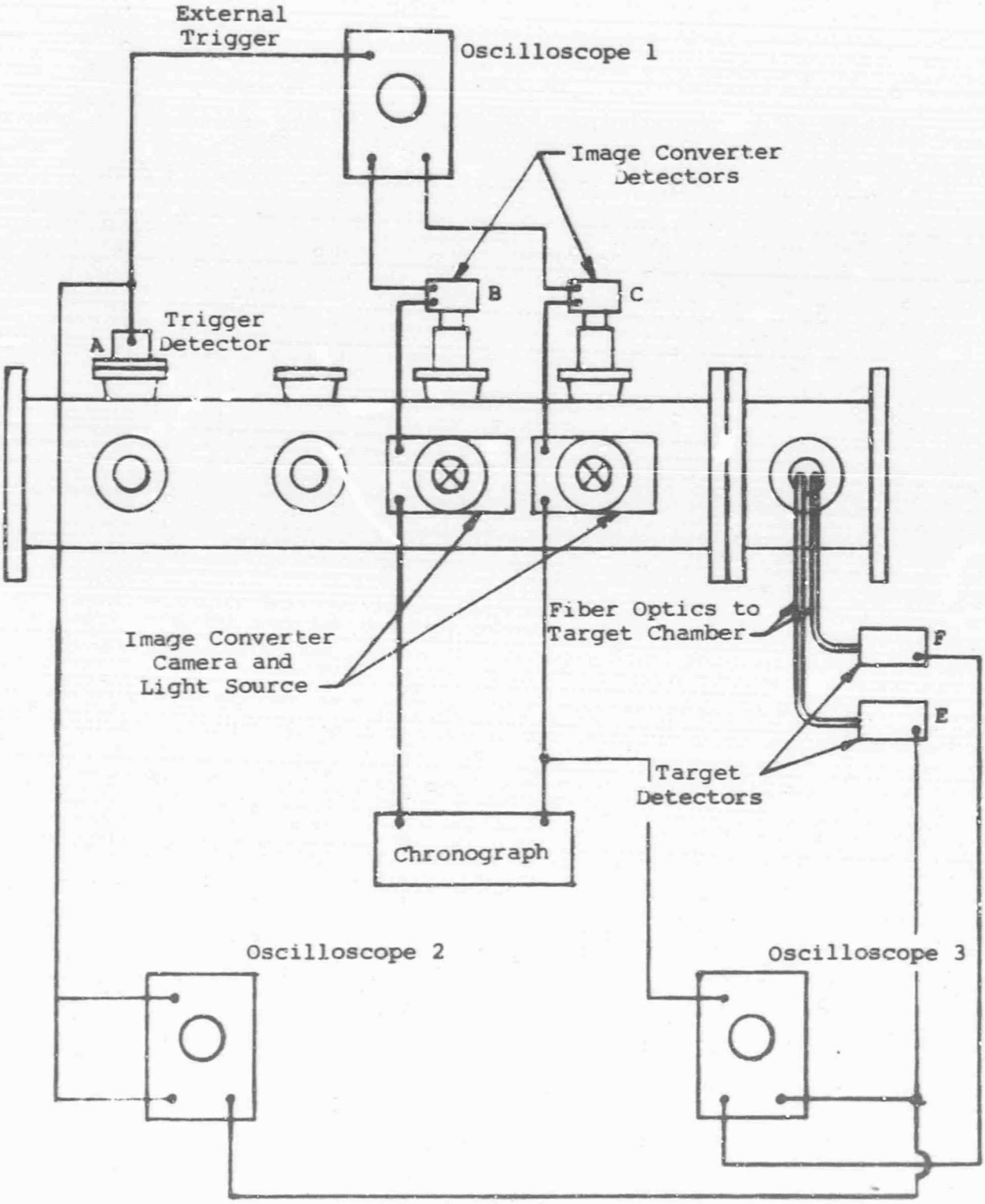

Figure 4 Schematic for Hypervelocity Range Instrumentation

The verified velocity of the sabot was obtained when both image converters photograph the sabot at stations B and C. The field of view on the image view converter was approximately 2 in. in diameter, which means that at a velocity of 20,000 fps the projectile was in the field of view for 8 μsec. This meant that, to record the sabot at the station, the trigger time had to be within ± 4 μsec. The trigger level was a function of both the bias in the trigger circuit and the luminosity of the sabot.

Since the microspheres could not be resolved on the timage converter photographs, direct verification of the ball velocity could not be made. An indirect means had to be devised to measure the ball velocity. For this purpose the ball impact flash in the target chamber was monitored by fiber optics and a photomultiplier, as shown in Figure 3 and 4. The time between when the sabot was at the image converter station and the impact flash on the target was recorded on oscilloscope 3. This time and the sabot velocity was the basis for calculating the ball velocity. Two assumptions were made: (1) the average sabot velocity measured at the image converter stations is equal to the muzzle velocity, and (2) the sabot and balls leave the muzzle at the same time. The ball velocity is then calculated using the equation:

$$V_B = \frac{D_{M-T}}{\frac{V_S}{D_{M-B}} + \Delta t_{B-T}}$$

where

D_{M-T} = distance muzzle to target

D_{M-B} = distance muzzle to image converter at B,

V_B = ball velocity,

V_S = sabot velocity, and

t_{E-T} = time between trigger of image converter at B and impact flash on target.

This technique for obtaining ball velocity was satisfactory. However, this was notable variance in the difference between sabot and ball velocity. It is felt that this variance was not a result of instrumentation or calculation technique, but was attributable to the manner in which the spheres and sabot separate. The exact mode of separation of micron spheres and sabot is not known. However, photographs

taken with the image converter camera show that 0.015-in.-diameter spheres form an irregularly spaced pattern following the sabot segments. This would indicate that actual separation of the balls from the sabot progressed as the sabot moved down range. This may be attributed to the fact that the oil film used to retain the balls has a relatively high binding force with the micron spheres, and it is a random ablative-type action that causes separation. Thus, in some cases when the balls were, in essence, given a piggy-back ride far down range the ball velocity was near that of the sabot velocity. At the other extreme, when the balls separate near the muzzle, a larger velocity difference occurred because of the poor ballistic density of the spheres. Between these extremes, anywhere along the sabot flight down range, the spheres may have separated resulting in the noted variance of the ball velocity.

Target Damage Analysis. - Each of the targets fired in this phase was subjected to microscopic examination. In the examination the following type of impacts were noted on the surface of the targets:

- round circular penetrations (Figure 5) with a typical crater lip, normally found on hypervelocity impacts;
- round circular craters (Figure 6) with a typical hypervelocity lip found around the crater on aluminum and Pagasus targets;
- round circular pitted surface on the stainless steel targets;
- irregularly shaped holes and craters; and
- a few low-velocity type-dents in the surface.

The target was considered penetrated only if there was a round clean hole through the target with the typical hypervelocity lip. If an irregularly shaped hole but no round penetration holes appeared in the target it was considered that this size ball did not penetrate the target. Figure 5 shows typical penetrations made on the various targets by the microspheres studied.

A calibrated retical in the eye piece of the microscope was used to measure the diameters of the holes and craters. These values are tabulated in Table II. There appears to be a wide distribution in the diameters for each particular ball and target combination. The variation is larger than

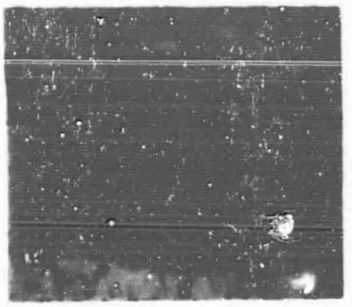

Mag: 120X

(a) 1-mil Stainless Steel Target; 20-30-μ-diam Sphere; Round 27

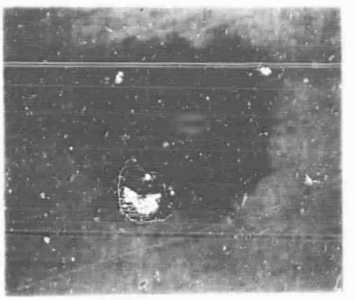

Mag: 120X

(b) 1-mil Stainless Steel Target; 38.6-μ-diam Sphere; Round 36

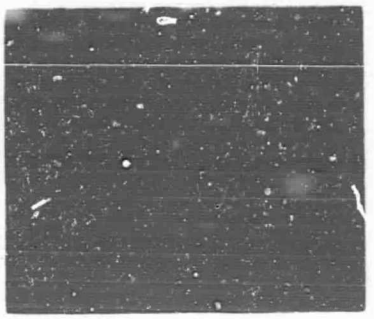

Mag: 42X

(c) 8-mil Pegasus Target; 130-μ-diam Sphere; Round 45

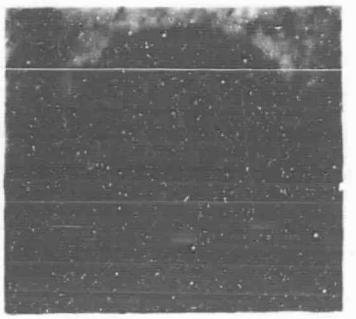

Mag: 120X

(d) 2-mil Stainless Steel Target; 48.6-μ-diam Sphere; Round 48

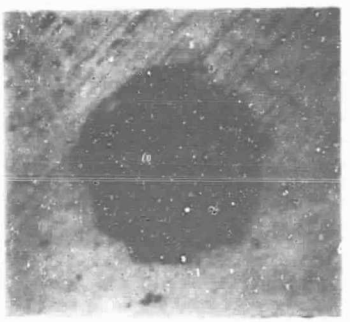

Mag: 120X

(e) 1-mil Stainless Steel Target: 48.6-μ-diam Sphere; Round 49

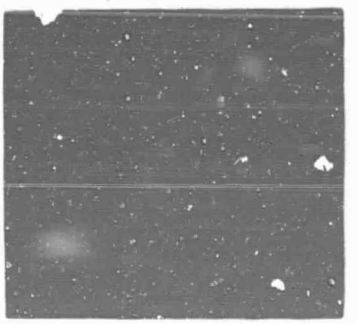

Mag: 120X

(f) 1.5-mil Pegasus Target 48.6-μ-diam Sphere; Round 56

Figure 5 Typical Target Damage Resulting from Perforating Projectile

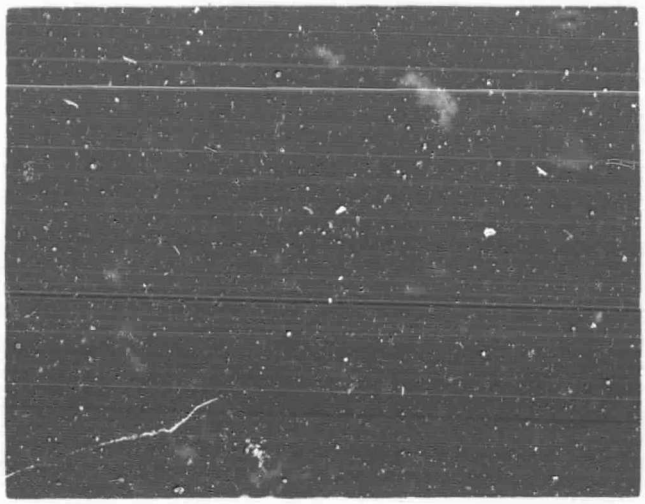

Mag: 42X

(a) 16-mil Pegasus Target
260-μ-diam Sphere
Round 42

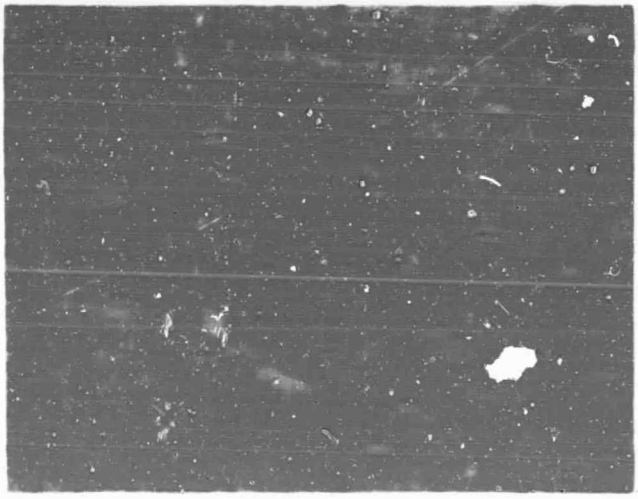

Mag: 42X

(b) 16-mil 2024T3 Aluminum Target
240-μ-diam Sphere
Round 29
No Penetration

Figure 6 Comparison of Perforation and Crater on 16-mil Aluminum Target

TABLE II

RESULTS OF MICROSPHERE FIRINGS

Combination	Description	Round Number	Sabot Velocity (fps)	Sphere Velocity (fps)	Hole Diameter (microns)	Crater Diameter (microns)
1	48.6-μ-diam sphere against 2-mil stainless steel target	48	21,100	No data	143 143 143 135 127 127 112	
		60	22,000*	21,300*	159 143 143 112 112 96	
		61	22,000*	21,000*	143 127	
2	48.6-μ-diam sphere against 1.5-mil Pegasus target	52	20,600	18,300	127 80	
		54	No data	No data	302 286	
		55	18,000*	No data	222 222 191 159	
		56	16,000*	No data	334 238 238 159	
		57	11,500*	No data	No clean circular penetration	286 143
		58	13,700*	No data	286	127 112
3	43.6-μ-diam sphere against 1-mil stainless steel target	43	21,000	19,800	143 143	
		49	19,400	19,350	143 143 127 127 127 112 112 96 96 88	
		59	18,200*	15,000*	159	
4	38.6-μ-diam sphere against 1-mil stainless steel target	36	21,500	19,[illegible]	143	
5	20-μ-diam sphere against 1-mil stainless steel target	26	22,000*	(Irregular shape, no circular holes -- possible conglomerate impacts)		
		27	22,500	(Irregular shape, no circular holes -- possible conglomerate impacts)		
6	130-μ-diam sphere against 8-mil Pegasus target	130	21,700	No data	445 430	
7	260-μ-diam sphere against 16-mil Pegasus target	260	21,900	20,950	716	
		240	19,000	No data		396 350 315 254 239 222

*Not verified with image converter data.

could be attributed to the velocity distribution and the tolerance on the ball diameter. Further, the spread in hole size is more pronounced for the balls 50-μ and smaller, and for the thinner targets. The 260 and 130-μ balls were individually selected eliminating all hollow balls, however, in the screening of 50-μ balls and smaller, this was not the case. As a result, the samples included a certain number of hollow spheres with various wall thicknesses. It is felt that this was the major factor in the large variance in the hole sizes for these impact conditions.

Results. - Table II contains tabulation of the microsphere experiments, including measurements of crater and hole diameter on the targets. The lowest velocity at which penetration occurred, the highest velocity at which the spheres failed to penetrate the target, and the corresponding round for each value are listed in Table III for the seven combinations. Penetration was obtained for six of the seven combinations; only the 20-μ spheres failed to penetrate the one-mil stainless steel target, within the velocity capability of the system. No data were obtained for below the threshold velocity for combinations 1 and 4. The effort of this phase has shown that multiprojectile methods of launching micro-size projectiles in light-gas guns are practical in micrometeoroid impact studies.

Phase II X-ray and Optical Lever Measurements

During Phase II experiments were conducted to measure (1) dynamic deformation on the target rear surface using sequential flash X-rays and (2) using optical lever techniques, shock wave breakout and pressure data for five hypervelocity impact conditions:

- Finite target impact with several hundreds kilobar pressure at the rear surface.
- Above the ballistic limit of the target, (penetration through the target).
- Below the ballistic limit of the target (no penetration through the target).
- Above the spallation limit of the target (complete detachment of a portion of the rear surface of the target).
- Below the spallation limit of the target (rear surface bubbled and fractured below the surface but no detachment from the target).

TABLE III

SUMMARY OF MICROSPHERE FIRINGS

Combination	Lowest Velocity with Penetration (fps)	Round Number	Highest Velocity without Penetration (fps)	Round Number
1	21,100 (sabot velocity)	48	No data	---
2	20,600 (sabot velocity) 18,300 (sphere velocity)	52	11,500 (sabot velocity)*	57
3	19,400 (sabot velocity) 19,350 (sphere velocity)	49	18,200 (sabot velocity)* 15,000 (sphere velocity)*	59
4	21,500 (sabot velocity) 19,800 (sphere velocity)	36	No data	---
5	No data	---	22,000 (sabot velocity)*	27
6	21,700 (sabot velocity)	45	21,300 (sabot velocity) 20,500 (sphere velocity)**	46
7	21,900 (sabot velocity) 20,950 (ball velocity)	42	19,000 (sabot velocity)	29***

* Not verified by image converter data.

** No penetration on target. However, craters on target did not appear to be typical hypervelocity impacts (i.e., spheres may not have impacted on target).

*** Round 29 was a 240-μ sphere against a 16-mil 2024T3 aluminum target.

Aluminum 2024-T4 spherical projectiles (5/32-in. diameter) were to be used against aluminum 2024-T3 targets. To achieve the required impact conditions, the velocity was to be held constant (within the limits of the gun) and the target thickness varied.

The experiments were set up so that both X-ray measurements and optical lever data would be obtained simultaneously. The experiments conducted are summarized in Table IV. Based on a nominal velocity of 20,000 fps, target were selected to meet the required impact condition, and ordered with one side polished for the optical lever experiments. If, in the course of the experiment, it was found that an improper target thickness was selected, corrections could be made by machining off the unpolished surface to obtain the desired impact condition.

Range and Launcher. - The hypervelocity range facility and launcher, shown in Figure 7, were used for these experiments. The launcher is an accelerated reservoir-type light-gas gun consisting of a gun powder chamber, a 20mm pump section, a high-pressure section and a smooth-bore .22-caliber launch tube. The range section has three basic components; a blast tank, a range section, and a target chamber. The blast tank serves to expand the gun gases following the projectile and provides space for aerodynamic separation of sabot sections. The range section is equipped with regularly spaced viewing stations at which the velocity detectors and image converters are located.

The special target chamber for these experiments mounts the target outside the range. The vacuum is maintained in the range by using the target and O-rings to provide the seal. This allows the X-ray and optical-lever measurements to be made on the back face of the target outside of the range.

Velocity Instrumentation. - A schematic diagram of the velocity instrumentation is shown in Figure 8. The system employed photomultiplier light detectors to determine the time of arrival at the velocity stations. The luminous projectile triggers each of the PM detectors as it passes. The time that it takes the projectile to travel the distance between the velocity stations is recorded both on dial-beam oscilloscopes and chronographs.

The photomultiplier (PM) detector at station A is used as a trigger source for oscilloscopes 1 and 2. Oscilloscope 1 monitors the image converter detectors at C and D, from which the projectile time between the station is determined. Oscilloscope 2 monitors stations B and D to obtain

TABLE IV

PRELIMINARY RESULTS PHASE II EXPERIMENTS
X-RAY AND OPTICAL LEVER MEASUREMENTS

Round Number	Target Thickness (inch)	Velocity (fps)	Crater or Hole Diameter (inch)	Crater Depth (inch)	X-Ray Data	Optical Lever Data	COMMENTS
1		20,000			Not Covered	Not Covered	Alignment shot
2		21,000					Hit snorkel tube
3	.750	20,000	.610	.294	Good	Poor - Too Sensitive	Adjusted target location - target bulged .023-inch
4		20,000					Hit snorkel tube
5	.750	21,000	.632	.316	Good	Good	Readjusted target location target bulged .023-inch
6	.600	20,000	.605	.430	Pre-Triggered	No Data	Partial spall, poor optical alignment
7	.600	21,100	.620	.314	Good	Good	Partial spall
8	.600	20,100	.630	.320	Good	No Data	Partial spall, poor optical alignment
9	.500	20,200	.590	Penetrated	Good	No Data	Complete spall
10	.500	21,500	.625	Penetrated	Good	Good	Complete spall
11	.375	20,400	.480	Penetrated	Good	Good	Just penetrated
12	.375	19,900	.475	Penetrated	Trig-gered late	Good	Just penetrated
13	.125	20,000	.496	Penetrated	Trig-gered late	Good	Penetrated
14	.125	19,900	.500	Penetrated	Pre-Triggered	Good	Penetrated
15	.750	19,500	.600	.293	Pre-Triggered	Excellent	Target bulged .074-inch
16	.650	19,900	.605	.310	Good	No Data	Bulged (.203-inch) split and cracked; camera not running; no spall (spall limit)
17	.650	20,000	.605	.311	Good	No Data	Bulged (.198-inch) split and cracked; low light level; no spall (spall limit)
18	.188	20,900	.569	Penetrated	Pre-Triggered	Good	Penetrated
19	.188	19,500	.555	Penetrated	Good	Not Covered	Penetrated

NOTES: Target material 2024-T4 aluminum.
Projectile 5/32" spheres - 2024-T3 aluminum.
Rounds Nos. 3, 5 and 6 made from bar stock;
all other targets made from rolled plate).

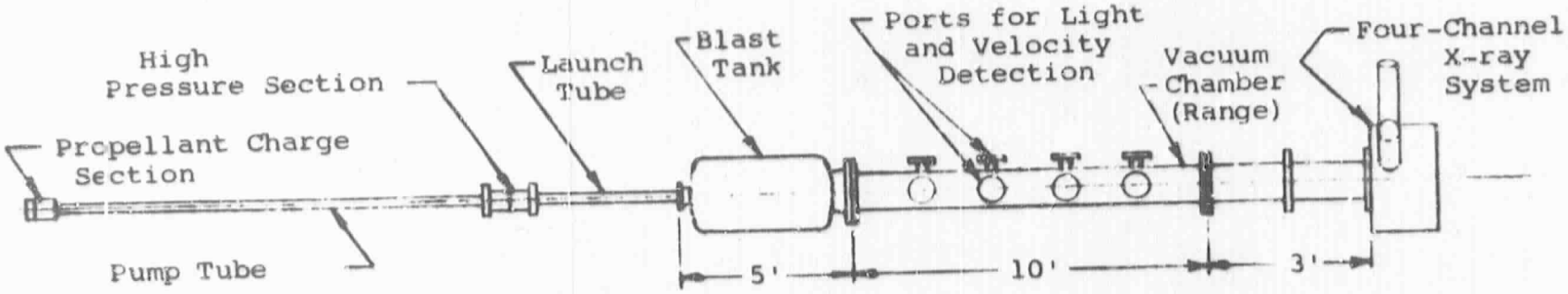

Hypervelocity Range Facility

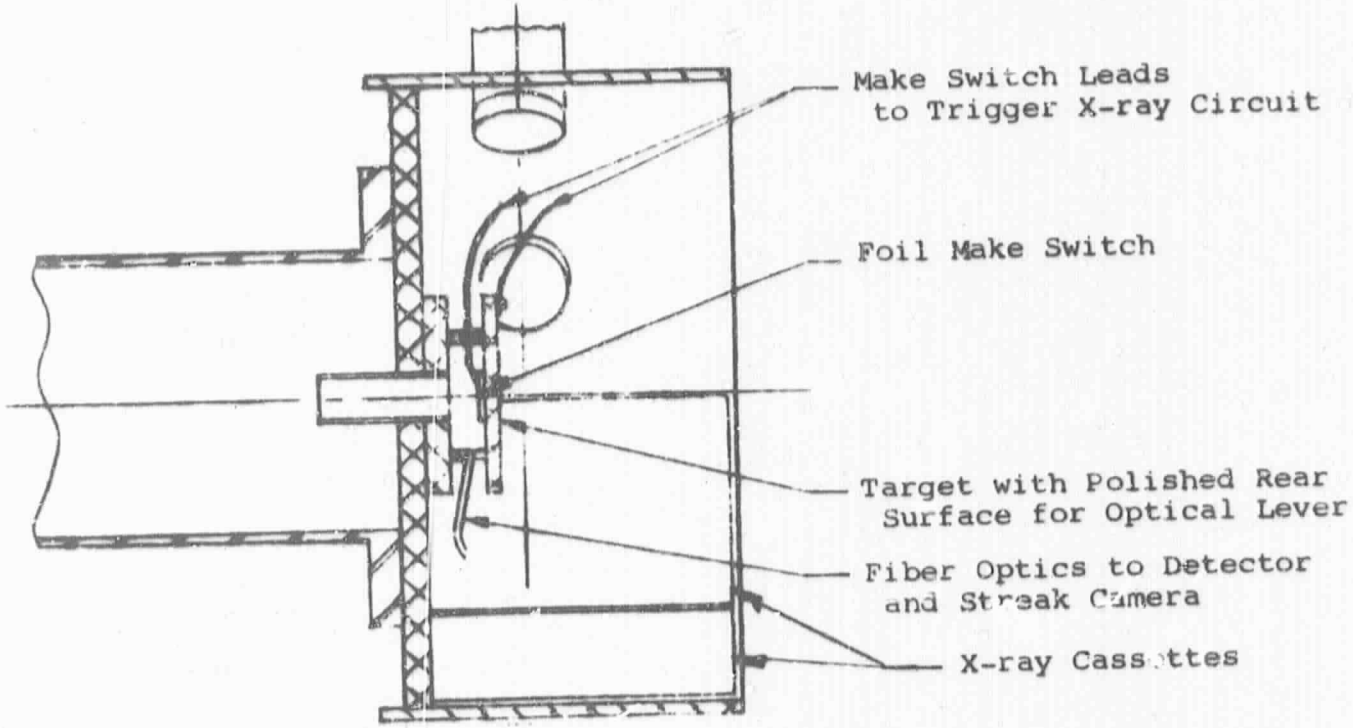

Figure 7 Range and Special Target Chamber

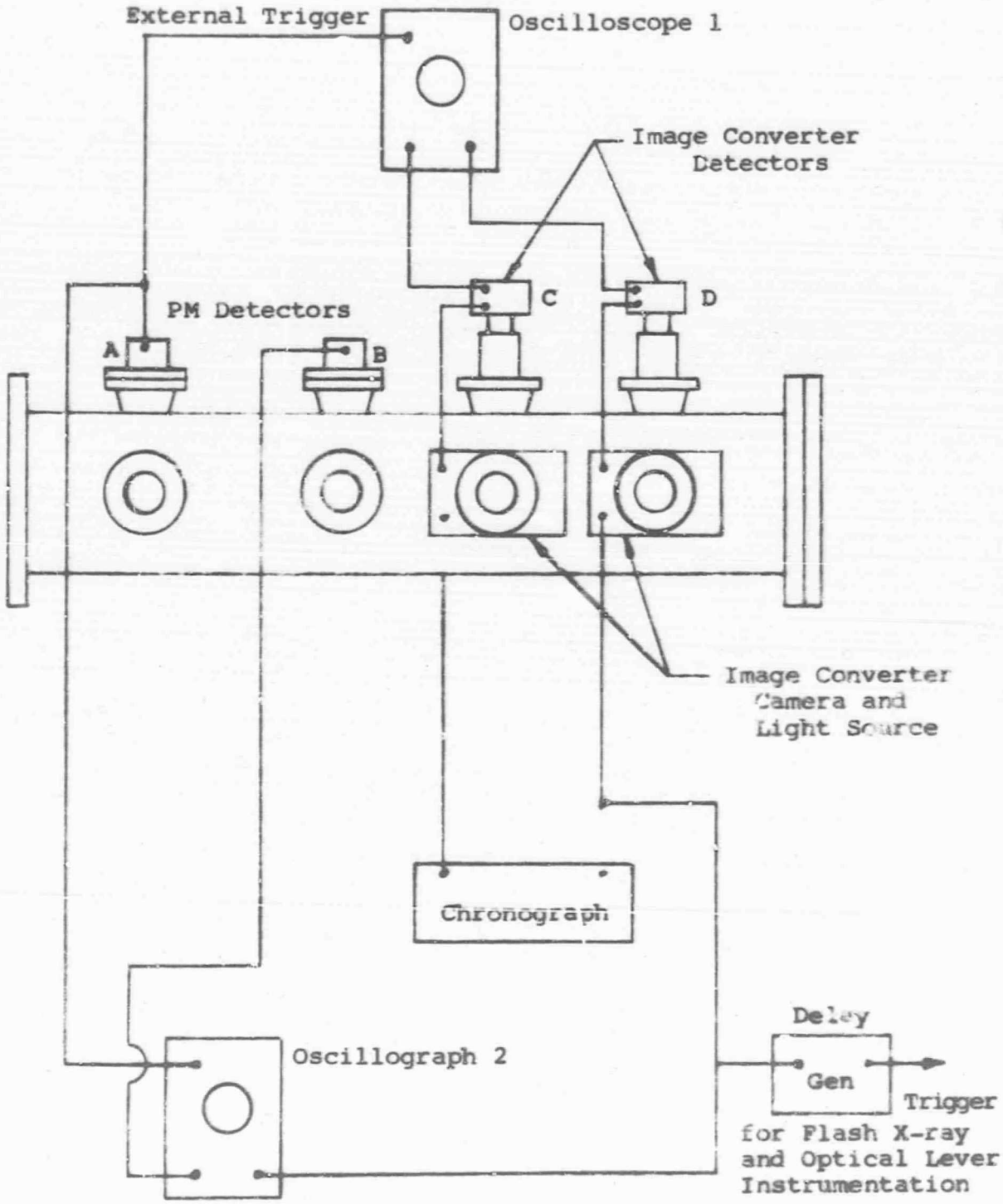

Figure 8 Schematic, Velocity Instrumentation

the flight time between these stations. Since oscilloscopes 1 and 2 are triggered from a common source, the time between stations B and C can also be determined. The most accurate time elapse measurement is obtained from the chronograph which incorporates a precise timing generator which can be read directly. The chronograph is started when the image converter camera at station C is triggered and stopped when the camera at D is triggered.

Due to sensitivity and slight variations in signal from the sabot the projectile as viewed on the Polaroid record shows a small variation in position from station to station. This slight variation is corrected for each velocity calculated, and thus very accurate and verified data are obtained. The other elapsed time measurements are used as back-up to the image converter camera setup. The velocity calculated from back-up instrumentation was found to be within 5 per cent of the verified velocity.

Targets. - The first three targets fired in this phase were made from round bar stock, in which the grain runs normal to the target surface. Examination of the target for Round 6 indicated that the failure was influenced by the direction of the grain (Figure 9). In normal bumper materials the grain runs parallel to the surface, since it was apparent that the failure mode was influenced by the grain direction, it was felt that the results would be more applicable with targets having the grain running parallel to the surface. Hence, all additional experiments used targets made from rolled plate which does have the normal grain orientation.

Figure 9 shows typical target damage as a function of target chickness and the effect of the grain direction. The impacted surface, a section through the impact, and the back surface of the target is shown for each target. Figure 10 shows a plot of the depth of penetration as a function of target thickness as determined in these experiments. Also indicated in this figure are the zones for which penetration, spall and no spall occur. Data from the bar stock targets are included on this figure, which indicates that the effect of grain direction is largest in the spallation zone, and would no doubt affect its upper and lower limit.

X-ray Measurements. - A four-channel sequential flash X-ray arrangement was used to obtain data on the dynamic deformation on the rear surface of aluminum targets for various impact conditions. A field emission model 730 flash X-ray system was adapted to the target chamber shown schematically in Figure 11. This arrangement was used to obtain four sequential radiographs at the rear surface of the targets. A trigger pulse at projectile impact was obtained from a simple

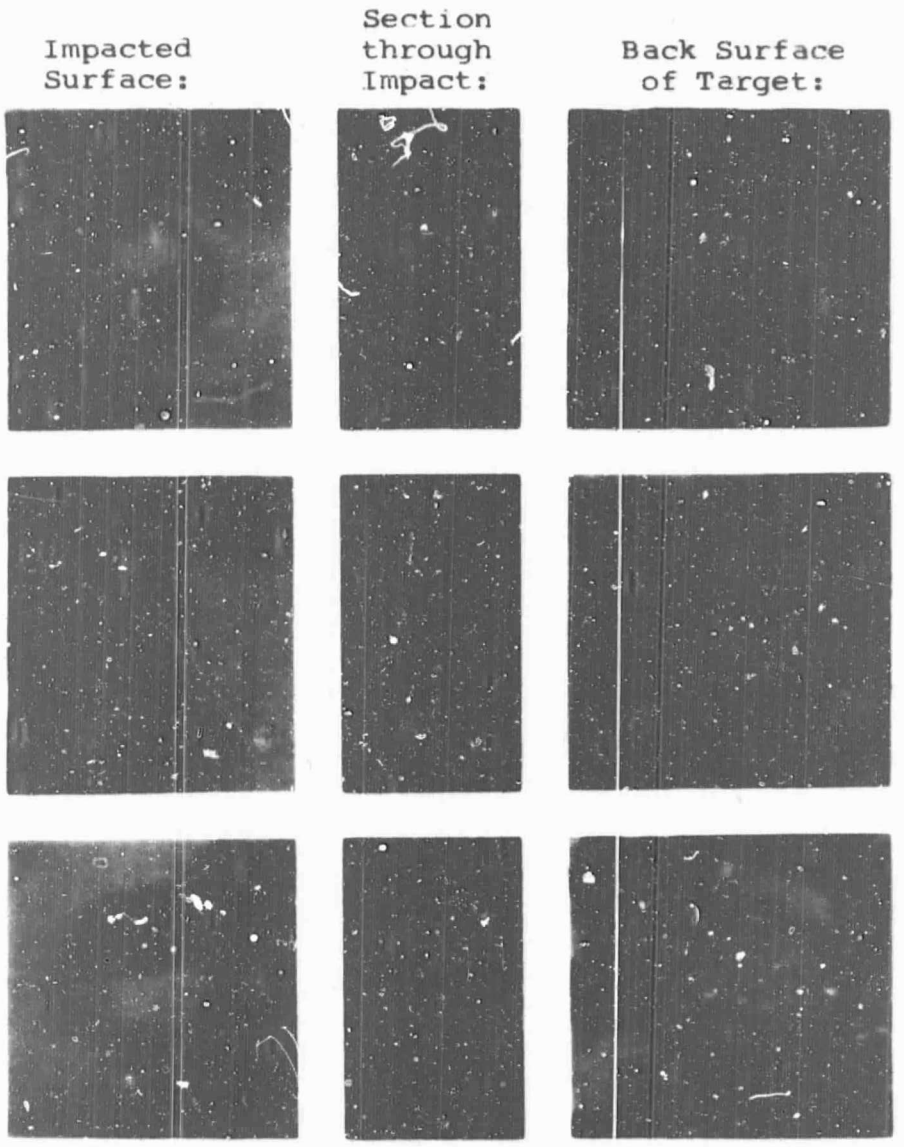

Figure 9 Results of Impacts on Aluminum Targets

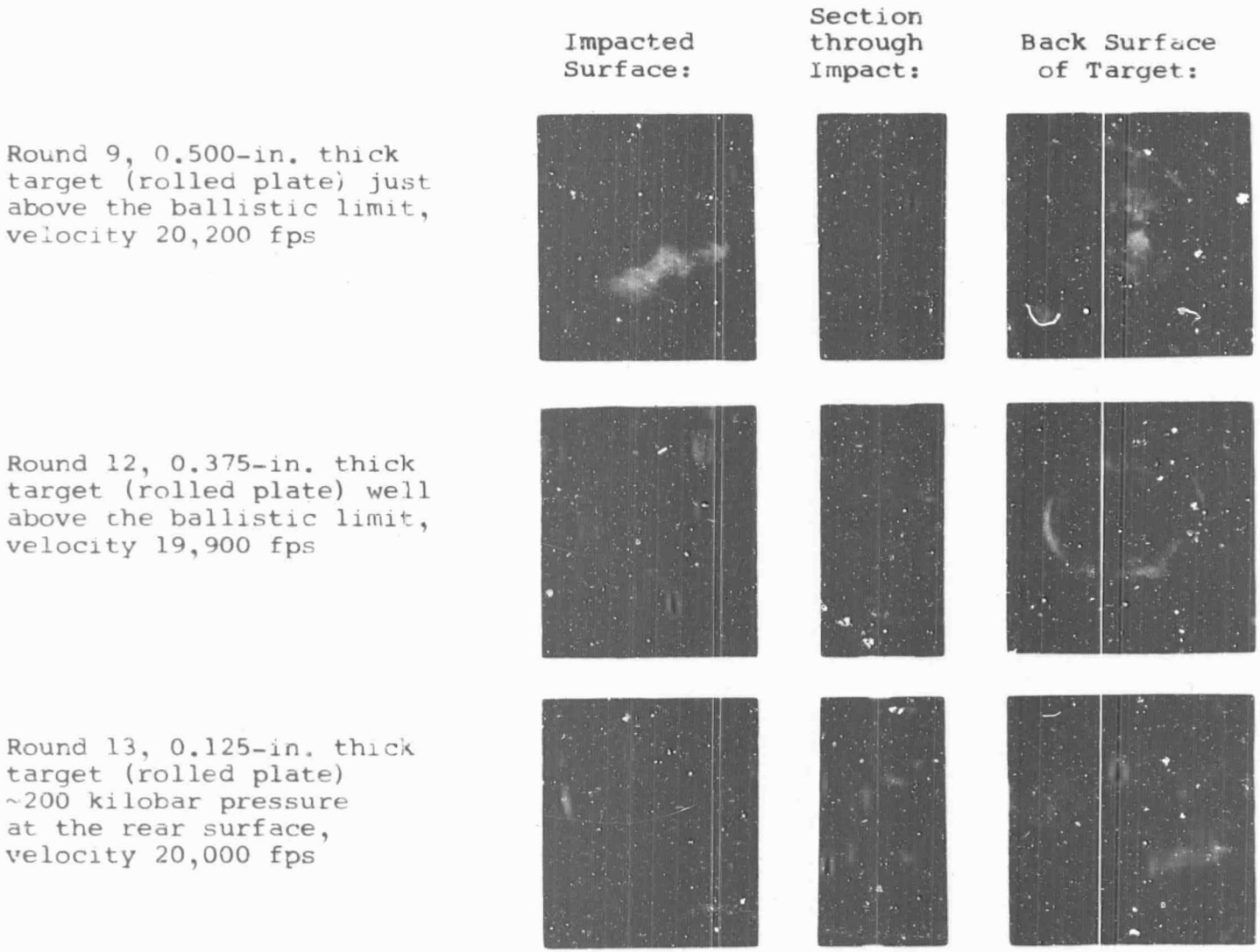

Figure 9 (Continued) Results of Impacts on Aluminum Targets

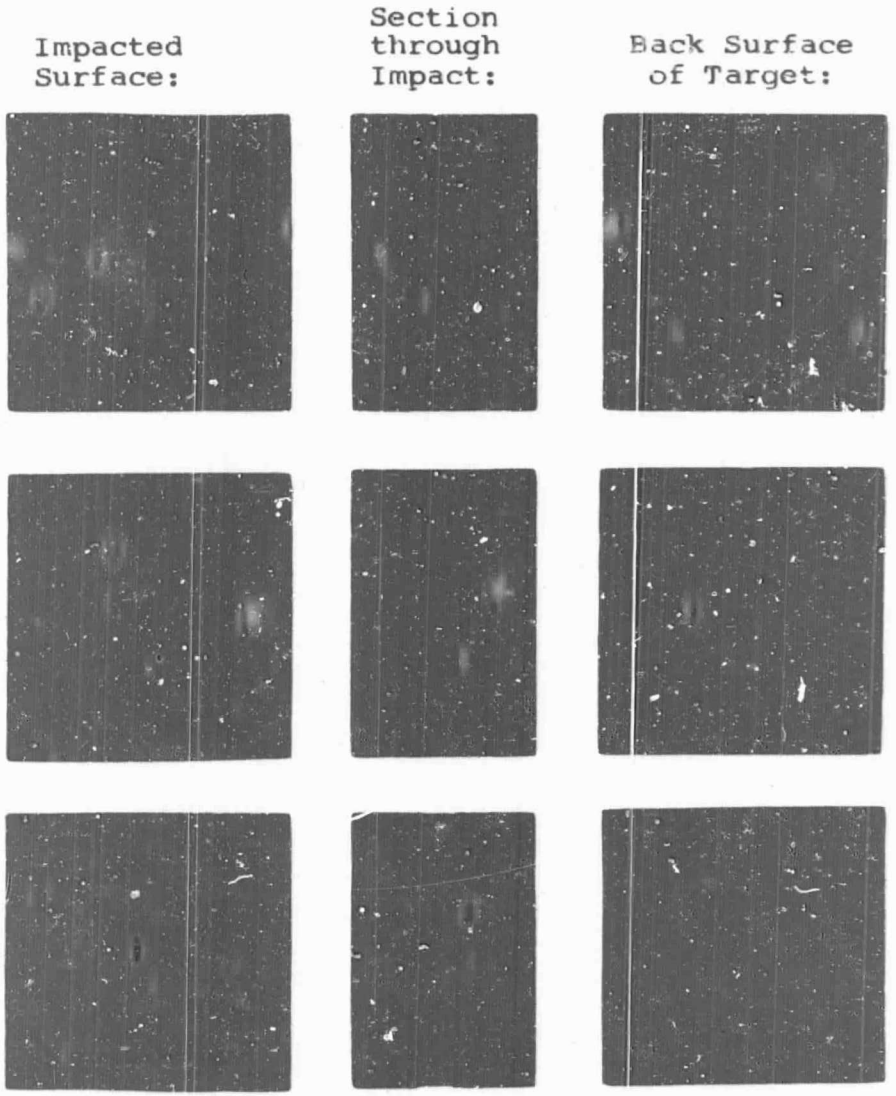

Figure 9 (Concluded) Results of Impacts on Aluminum Targets

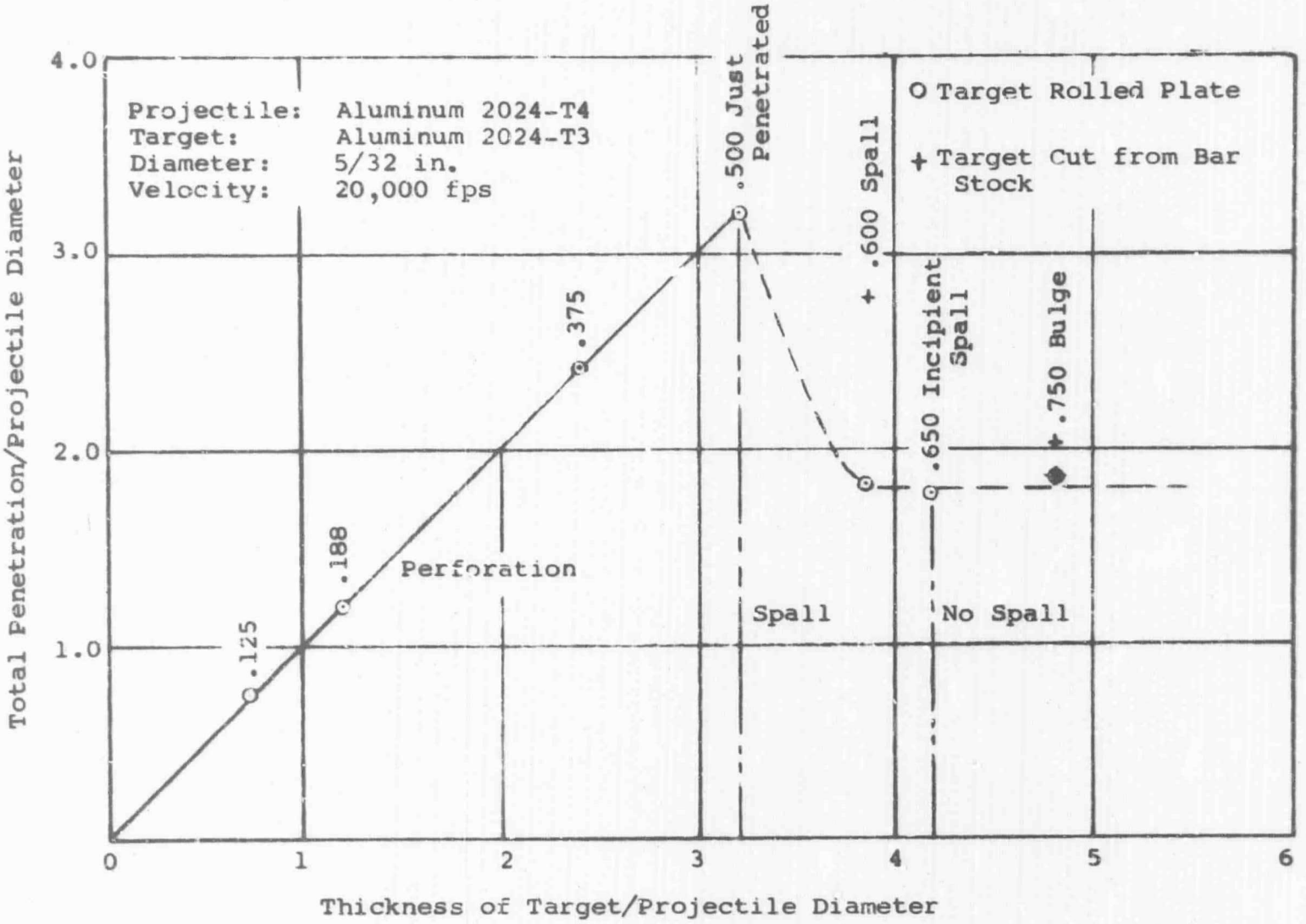

Figure 10 Depth of Penetration as a Function of Target Thickness

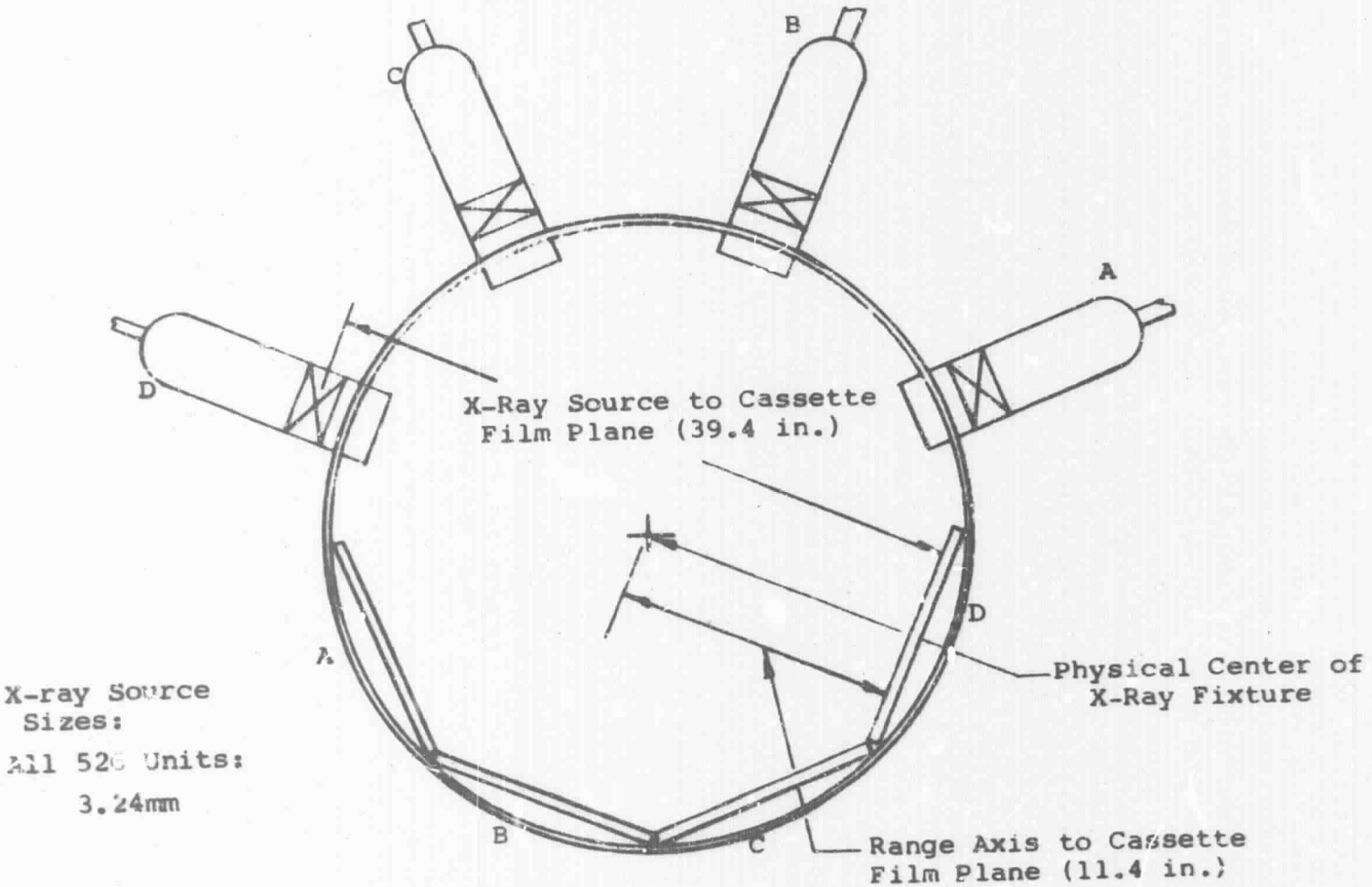

Figure 11 Four-Channel X-ray Fixture (Rear View)

foil make-switch mounted on the front surface of the target (Figure 7). One side of the switch was a 1-mil-thick disk of aluminum foil insulated from the target by a 3-mil-thick disk of paper. The target was the second side of the switch and when the projectile impacted, the switch would be shorted and a trigger pulse formed to trigger the X-ray units. A block diagram of the X-ray instrumentation is shown in Figure 12.

The third oscilloscope was used to set up the X-ray delay times and also monitored the delay times during the test. Results showed that the delays are accurate within the nanosecond range. The fourth oscilloscope monitored the output signal from the R.C. circuit of the make-box and the output from the target detector.

Although the foil switch circuit worked on every test fired, there was considerable scatter in the signal. The variation was large enough to result in cases where (1) the circuit would be pretriggered and the X-rays did not show any deformation on the rear surface of the trigger, and (2) late triggers which would occur after the event or bubble growth was over. Pretriggering may have resulted from small debris from the sabot arriving ahead of the sphere on target. The delayed trigger must have resulted from circuit malfunctions, but repeated manual tests of circuits show the function time of the circuit to be reproducible. Variation was less than $\pm$ 1 μsec.

The bubble height growth was measured from the sequential X-rays. Height on the X-ray film was measured directly off the film. A stepped cone was radiographed (Figure 13) to provide a means of calibrating both the height and diameter of the bubble. A 0.75 calibration factor was used to obtain the actual bubble height. Copies of the X-rays are shown in Figure 13. Table V lists the measurement of the bubble size for which sequential X-ray data were obtained. The times listed in the table are the delay times set on the X-ray delay unit. These data are plotted on Figure 14 through 19 as solid lines.

As mentioned, there was considerable scatter in the function of the trigger circuit, and no correction could be determined from the records. To compare the effect of target thickness on bubble growth, a common time base had to be established. This was done by the following method:

(1) The measured heights were plotted as a function of time (solid lines on the curves).

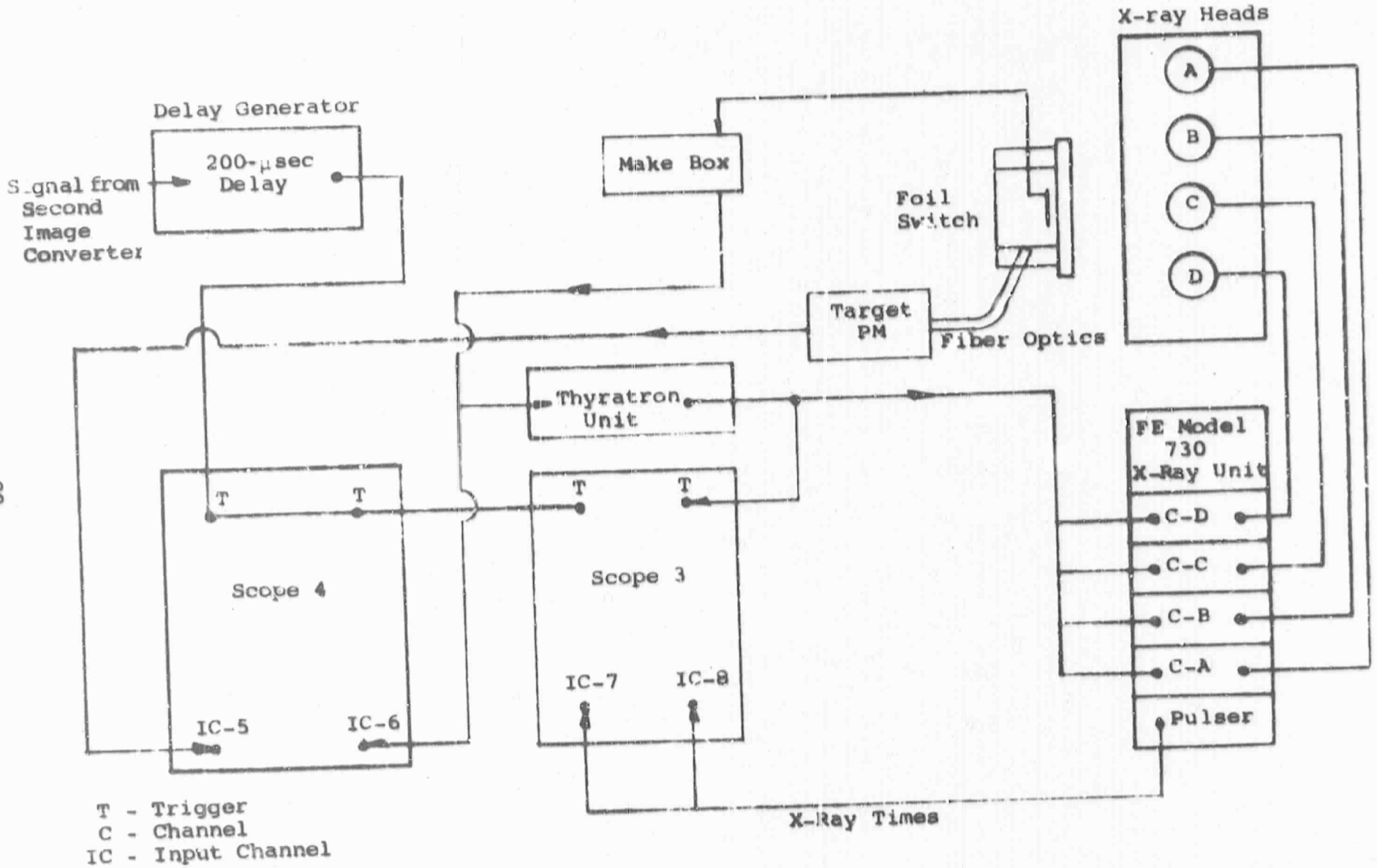

Figure 12 X-Ray Instrumentation

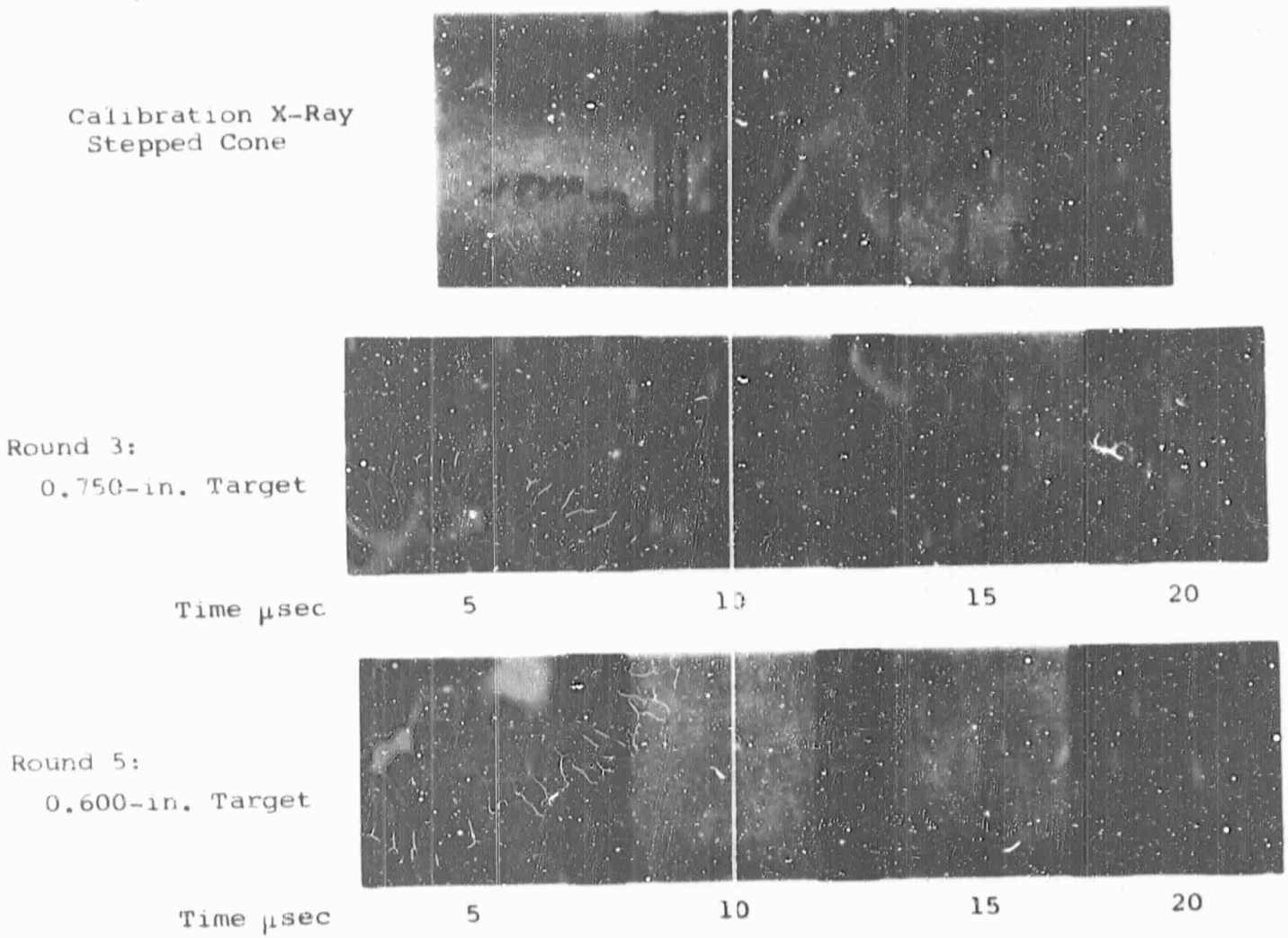

Figure 13 X-Ray Records

Round 16:
0.650-in. Target

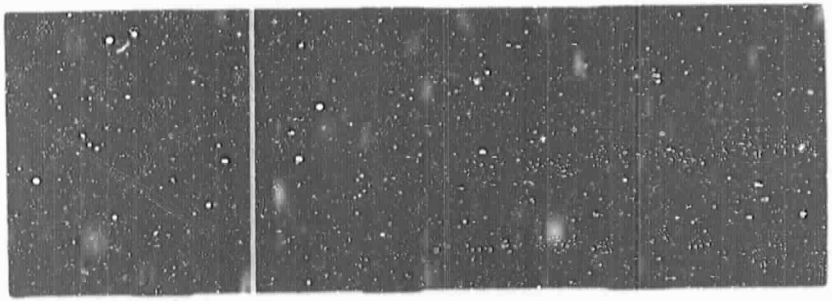

Time μsec 15 20 25 30

Round 17:
0.650-in. Target

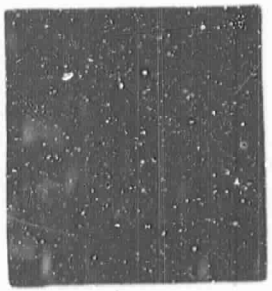

Time μsec 35

Round 19:
0.188-in. Target

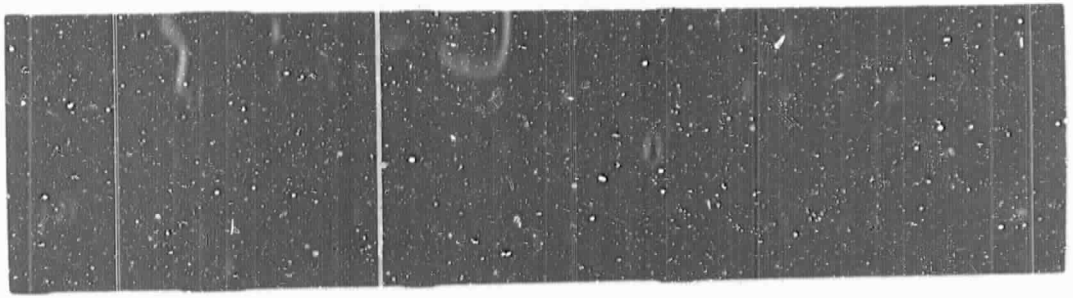

Time μsec 5 10 15 20

Figure 13 (Continued) X-Ray Records

Round 10:
0.500-in. Target

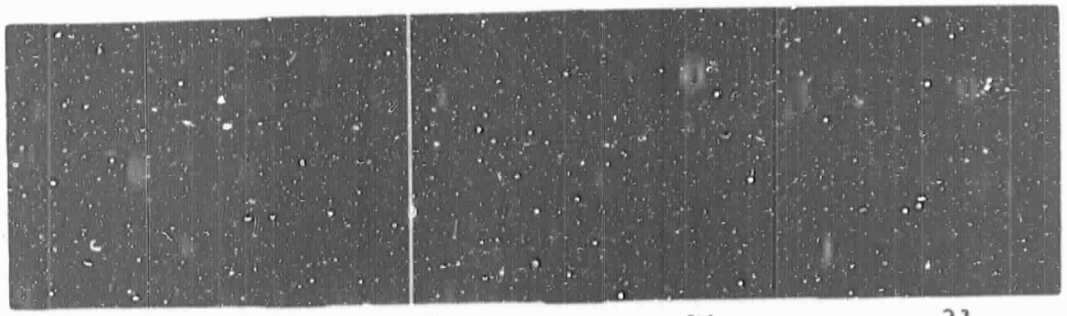

Round 11:
0.375-in. Target

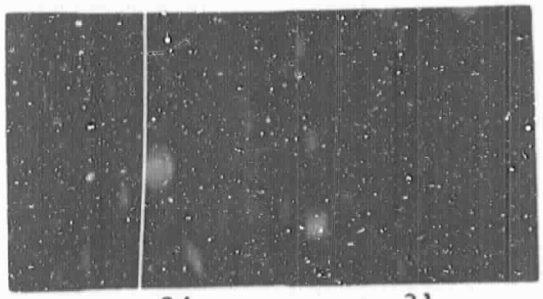

Round 15:
0.375-in. Target

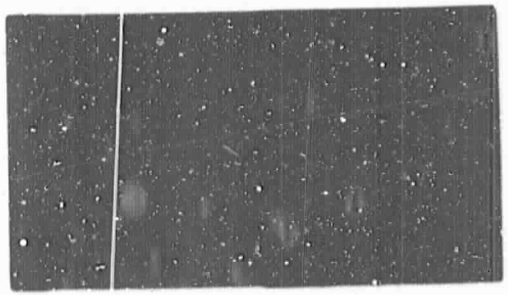

Figure 13 (Continued) X-Ray Records

Round 7:
0.600-in. Target

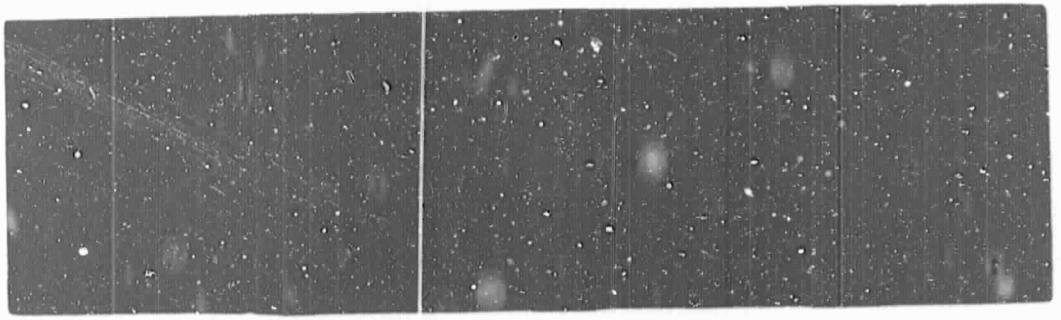

Time μsec 5 10 15 20

Round 8:
0.600-in. Target

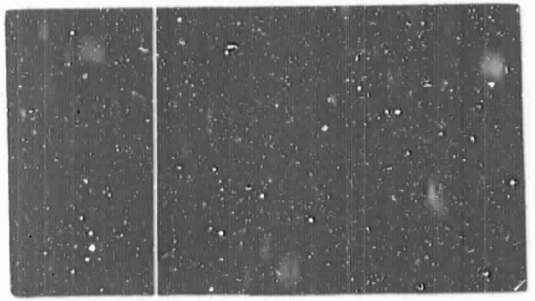

Time μsec 19 26

Round 9:
0.500-in. Target

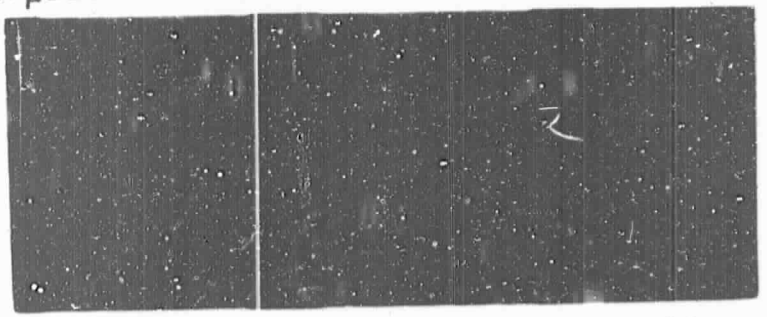

Time μsec 12 19 26

Figure 13 (Concluded) X-Ray Records

TABLE V

X-RAY MEASUREMENT BUBBLE GROWTH

Round Number	Target Thickness (in.)	Velocity (fps)	Station A			Station B			Station C			Station D		
			Height (in.)	Diameter (in.)	Time (μsec)	Height (in.)	Diameter (in.)	Time (μsec)	Height (in.)	Diameter (in.)	Time (μsec)	Height (in.)	Diameter (in.)	Time (μsec)
3	0.750	20,000	---	---	5	0.026	---	15	0.019	---	10	0.030	---	20
5	0.600	21,000	0.041	0.90	20	0.026	0.75	15	0.011	---	10	0.008	---	5
7	0.600	21,100	0.270	1.05	20	0.135	1.05	10	0.205	1.125	15	0.052	0.75	5
8	0.600	20,100	0.210	1.05	26	---	---	12	0.110	0.90	19	---	---	5
9	0.500	20,200	0.350	0.90	26	0.100	0.75	12	0.245	0.98	19	---	---	5
10	0.500	21,500	0.675	0.98	31	0.345	0.98	17	0.500	0.98	24	0.225	0.98	10
11	0.375	20,400	0.425	0.86	31	---	---	17	0.164	0.75	24	---	---	10
15	0.375	19,500	0.075	0.90	25	---	0.71	15	0.038	---	20	---	---	10
16	0.650	19,900	0.190	0.050	30	0.094	0.975	20	0.140	1.01	25	0.030	0.45	15
17	0.650	20,000	0.037	0.90	35	---	---	25	---	---	30	---	---	20
19	0.188	19,500	1.60	1.140	20	0.75	0.81	15	0.300	0.61	5	0.490	0.70	10

Height and diameter are corrected values = measure x 0.75.

Time is measured delay time, not corrected for trigger scatter.

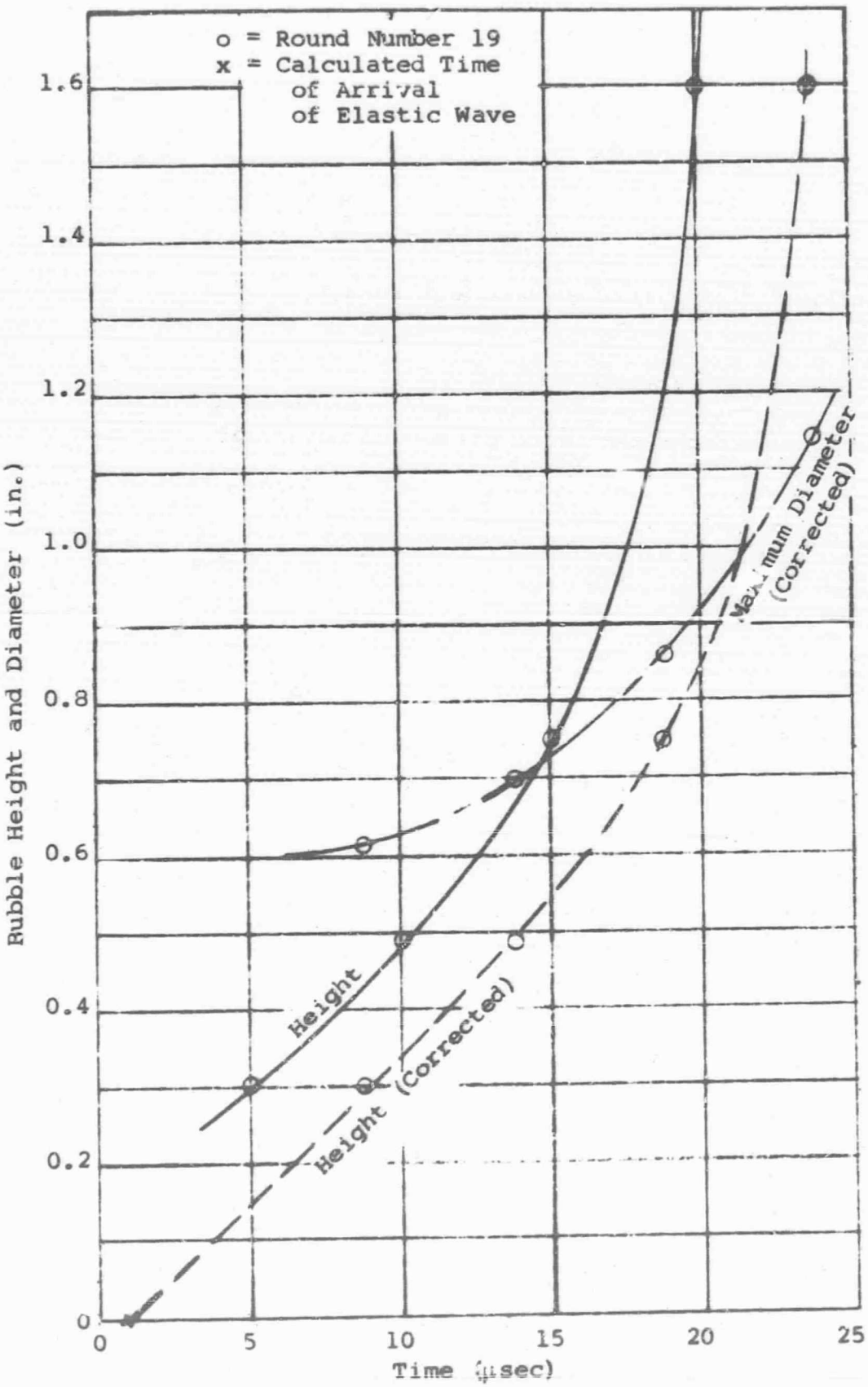

Figure 14 Bubble Growth, 0.188-in. Target

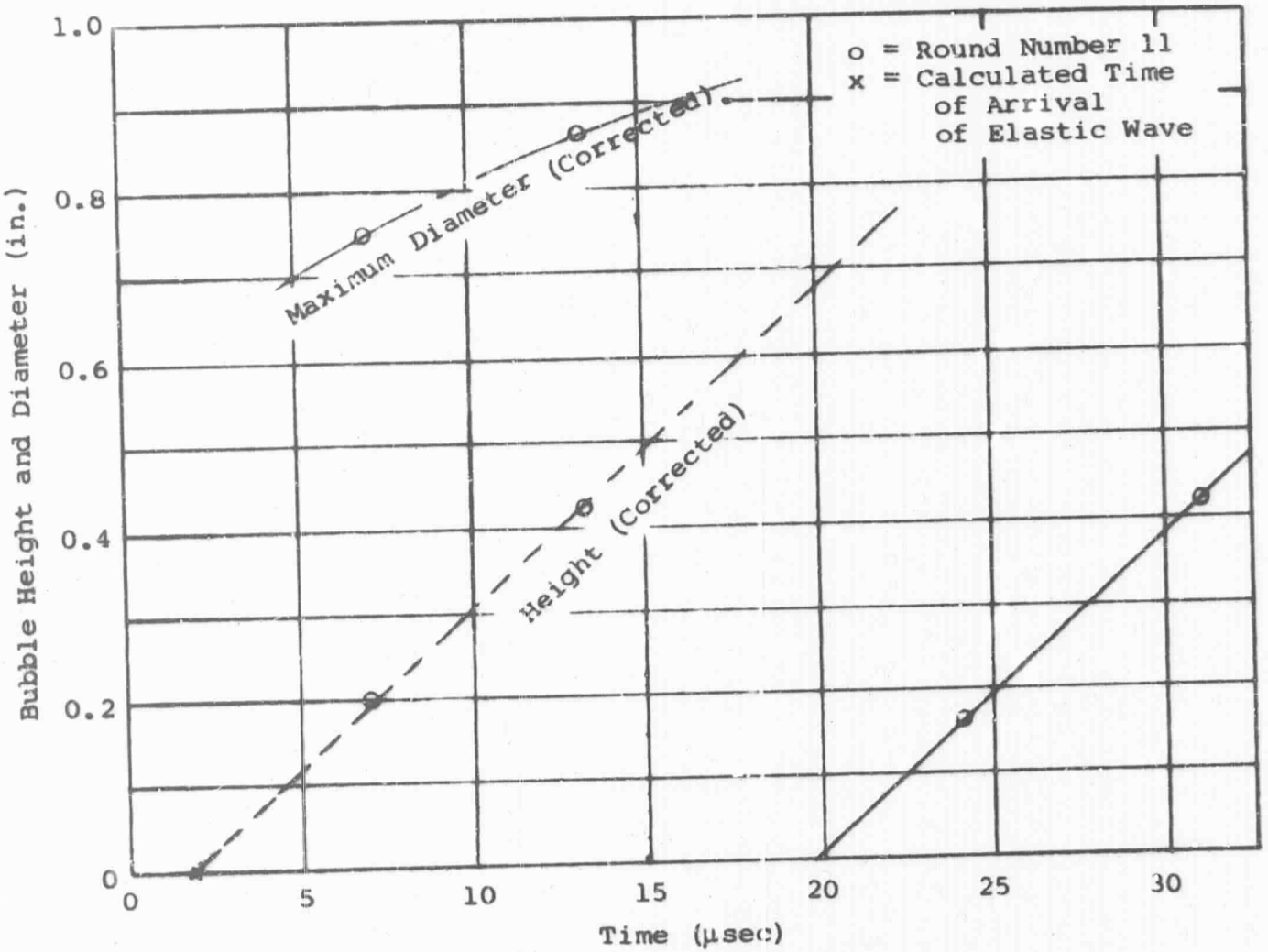

Figure 15 Bubble Growth, 0.375-in. Target

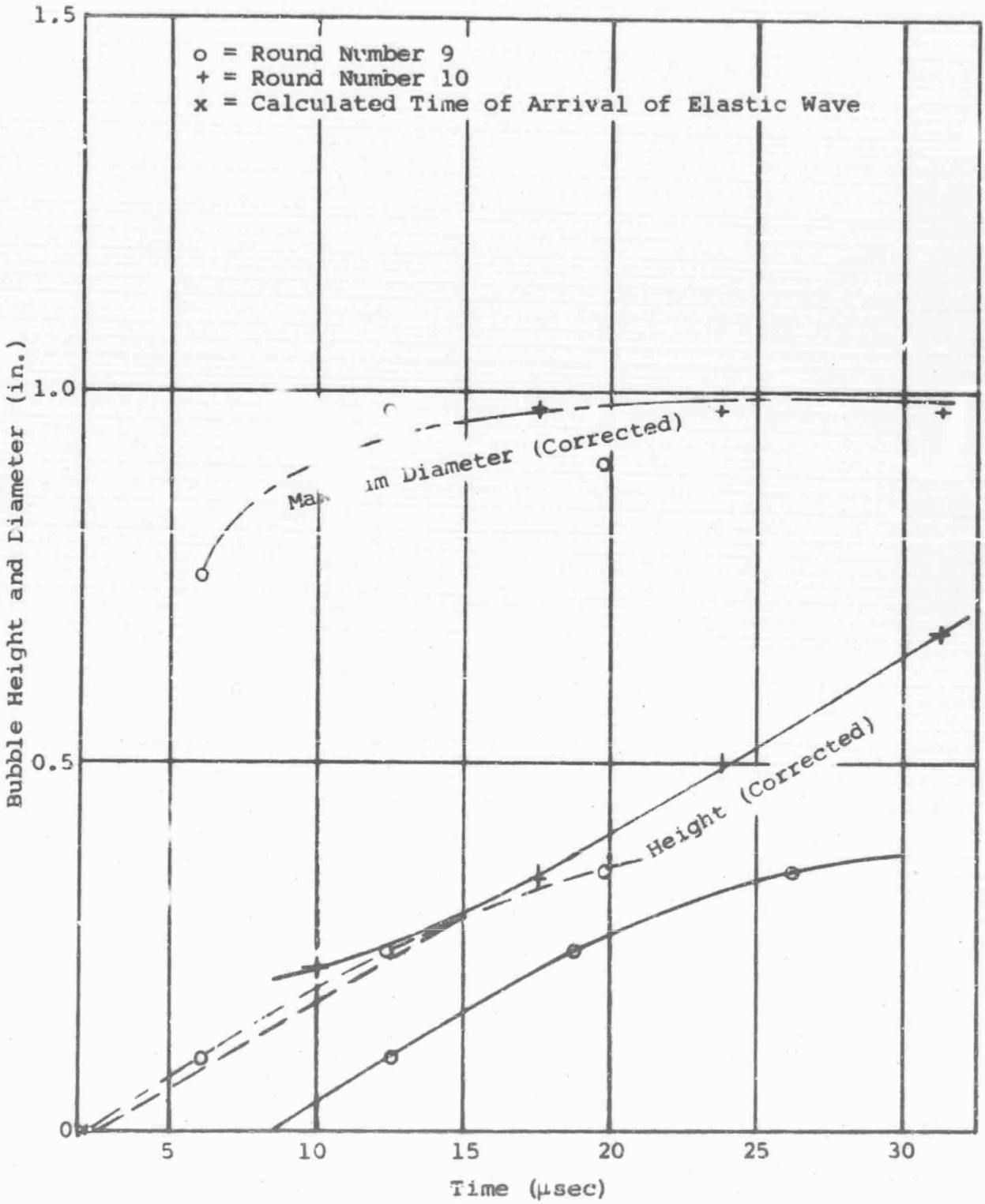

Figure 16 Bubble Growth, 0.500-in. Target

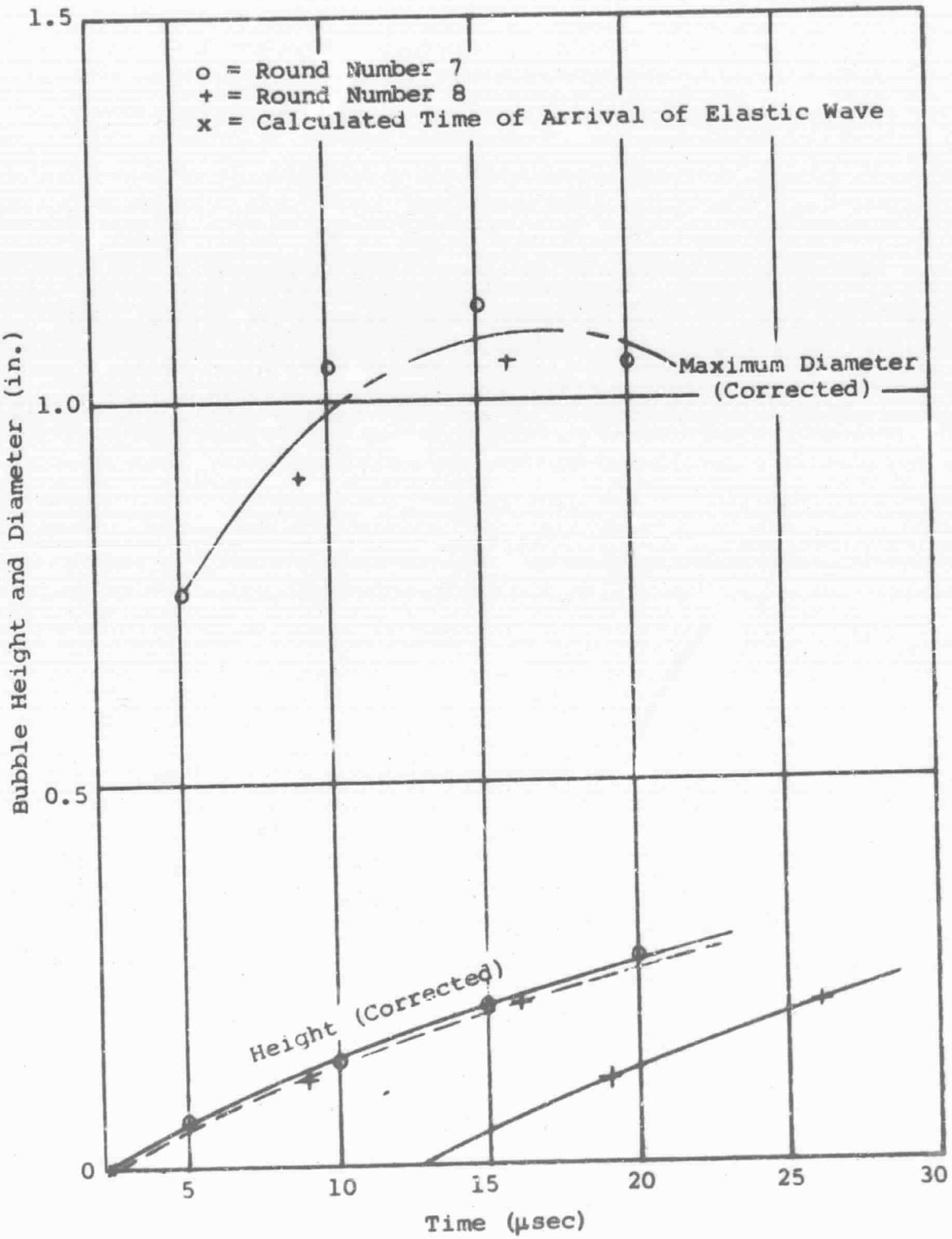

Figure 17 Bubble Growth, 0.600-in. Target

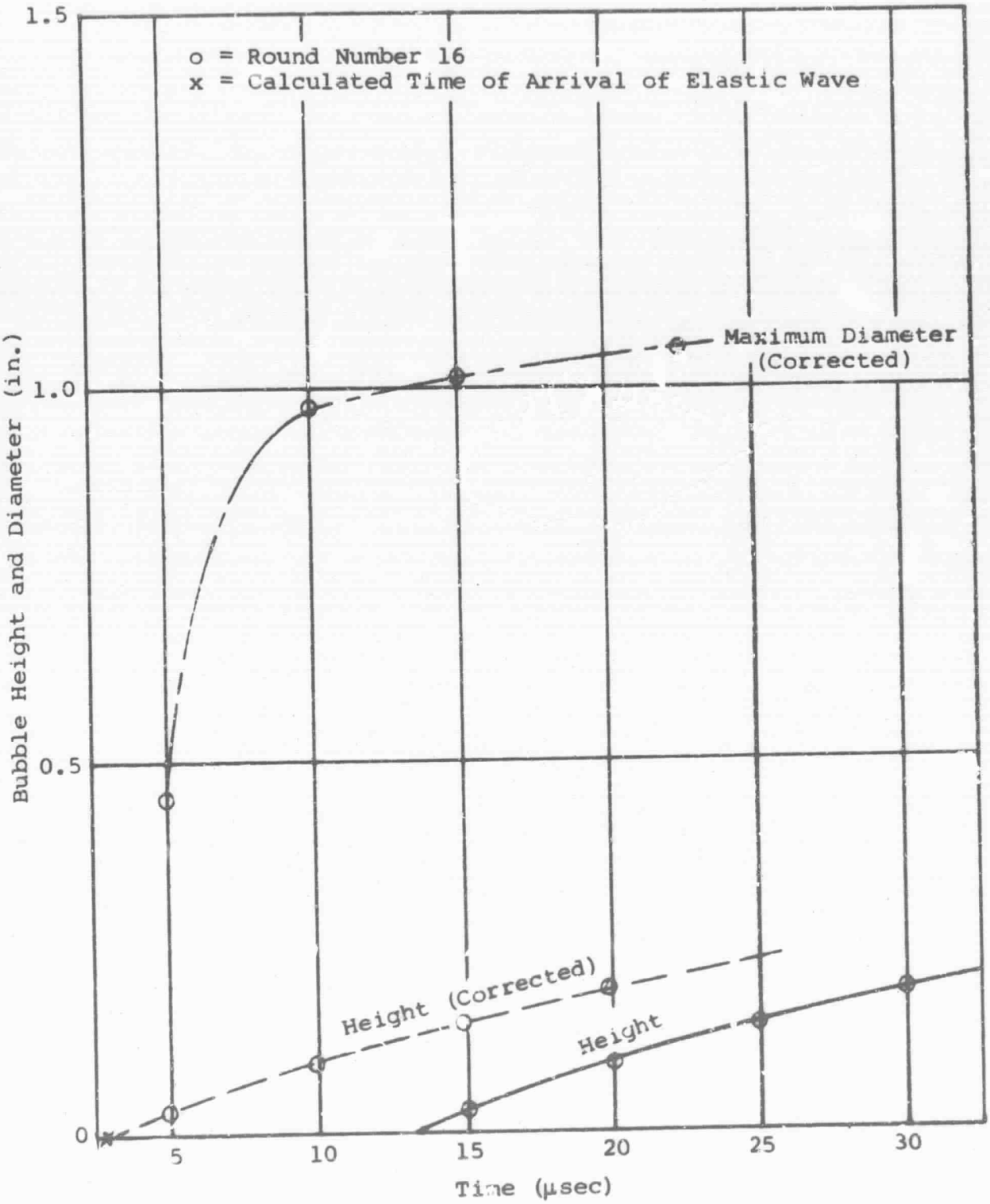

Figure 18 Bubble Growth, 0.650-in. Target

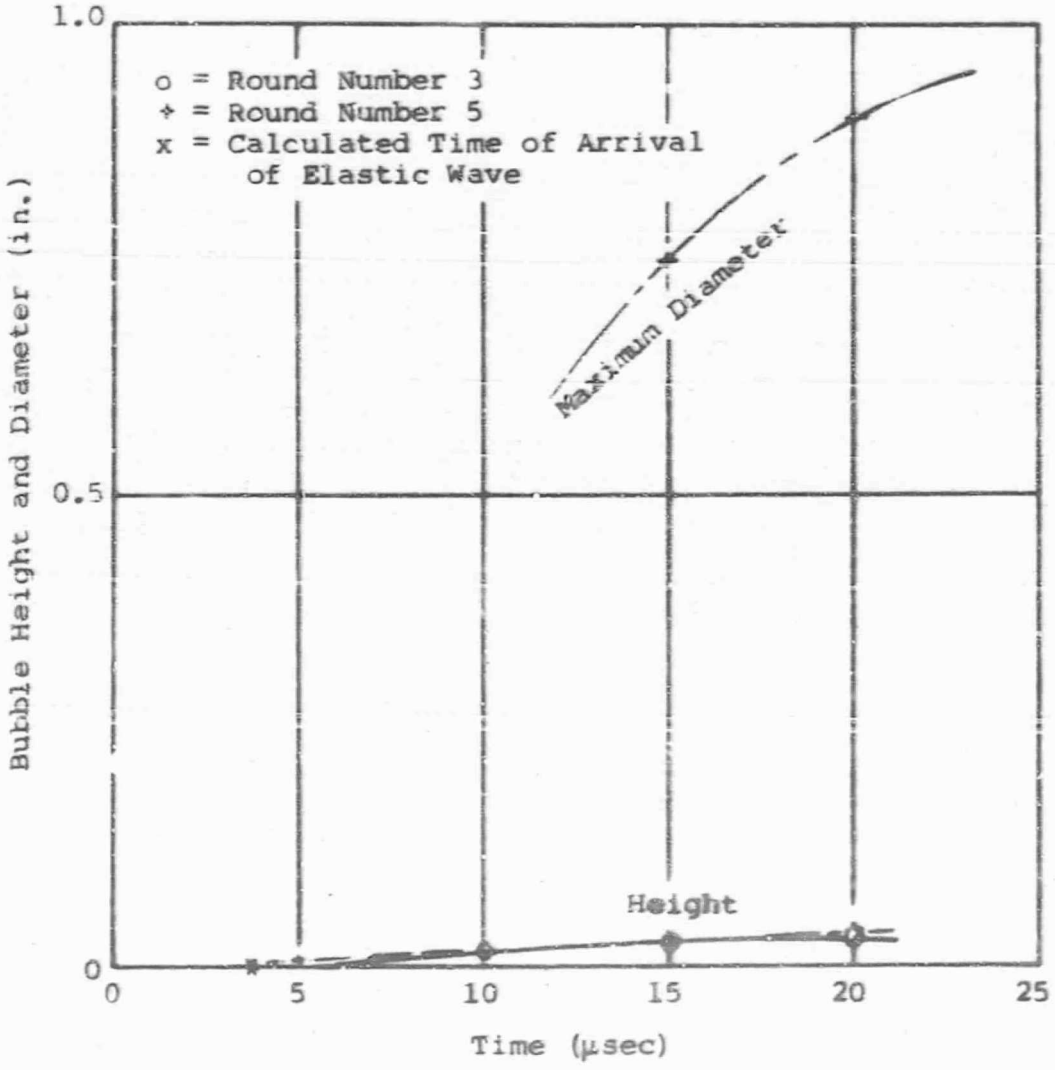

Figure 19 Bubble Growth, 0.750-in. Target

(2) They were then extrapolated to a zero height.

(3) Then the time for the elastic wave velocity to (6.2mm/μsec) travel through the target was computed.

(4) It was then assumed that this time corresponds to the first deformation on the back surface of the target, or the time from impact when the height as a function of time was equal to zero.

(5) The extrapolated curve was then shifted so that the height equal to zero occurred at this time. The correct curve was plotted as a dashed line on Figures 14 through 19.

The results of the corrected curves for all target thicknesses are plotted on Figure 20. Although these curves were generated by a relatively simple method of obtaining a common time base, the plots whos with amazing consistency the effect of target thickness on bubble height growth.

The bubble diameter was measured in the same manner as the height. For the shallow height ubbbles, it was very difficult to determine the diameter accurately, because of the shallow slope of the curve. The diameters as measured and corrected for magnification are also shown in Table IV. The results are plotted as a scmidashed line on Figures 14 through 19, corrected to the common time base as previously determined.

Optical-Lever Experiments. - The optical lever experiments were designed to meet three objectives:

(1) Obtain shock arrival times, velocities, and pressures at the rear surface of a finite target within the pressure region from 100 to 300 kb.

(2) Obtain shock arrival times, velocities, and pressures at the rear surface of a finite target above and below the ballistic limit.

(3) Obtain shock arrival times, velocities, and pressures at the rear surface of a finite target above and below the spallation limit.

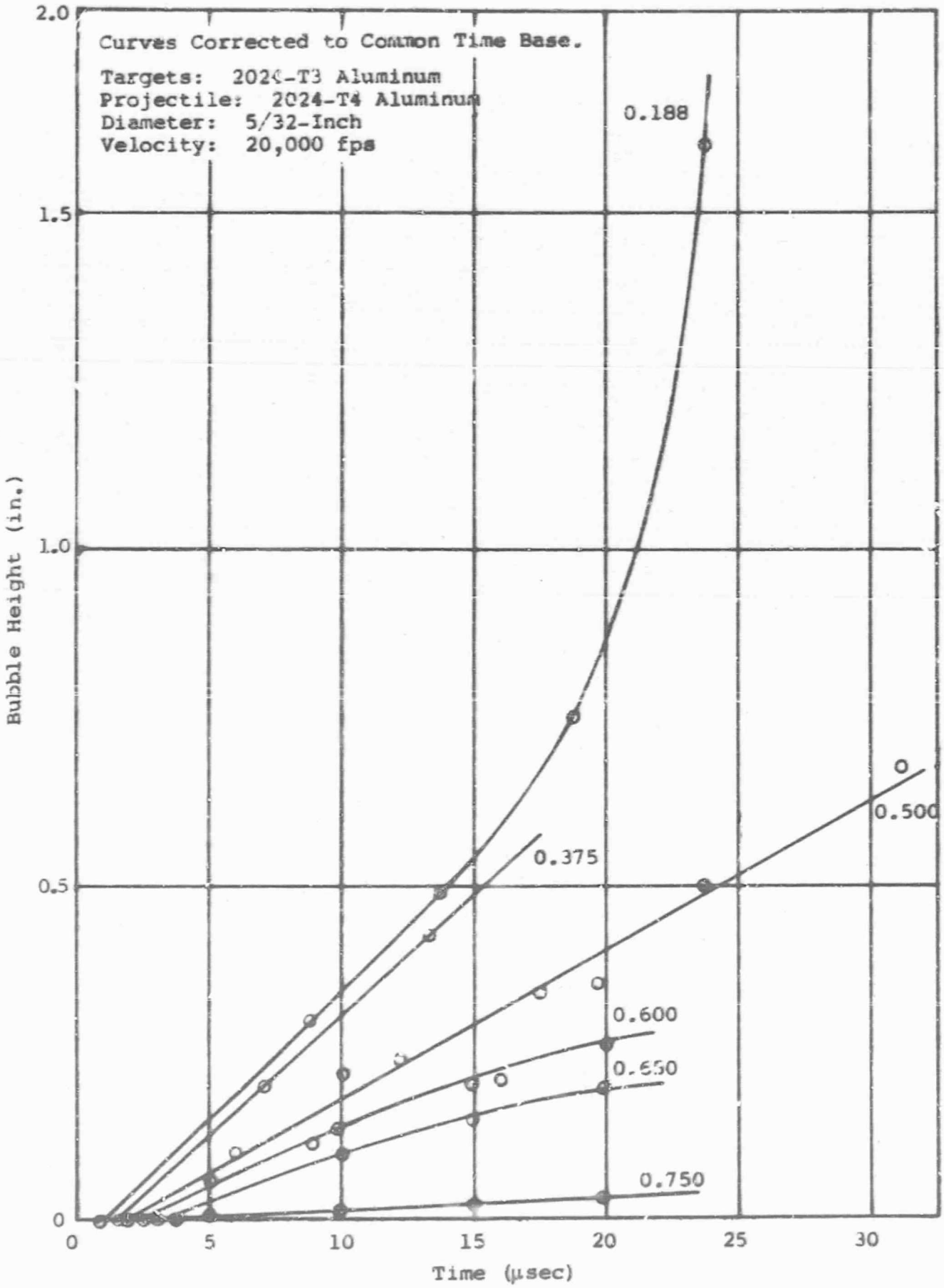

Figure 20 Effect of Target Thickness on Bubble Growth (Height)

Experiments were designed with constraints that:

(1) The projectile impacting the target should have a velocity within 20,000 to 23,000 feet per second and attempts should be made to maintain a constant velocity throughout the series.

(2) The target and projectile must be of the same material.

(3) The target and projectile must be a material that exhibits a simple shock behavior.

Data from these experiments will serve as a basis to compare results from elaborate computer codes simulating the impact process and subsequent shock decay.

Figure 21 illustrates the optical lever technique.* The polished target is placed at the end of a hypervelocity range and the light source grid is placed a fixed distance d from the target. An objective lens is used to focus the grid onto the slit plane. A second lens, internal to the camera, focuses the slit onto the film. Lines of light passed by the grid are cut into dots of light by the slit. These dots of light are streaked across the film.

As the projectile strikes the target, the shock wave radiates to the polished surface and is reflected. Because the shock strikes the polished surface at an angle, the surface is turned. This turning angle depends upon the shock strength as well as the emergence angle, and results in an optical lever deflection on the film. Multistepped shock waves produce successive deflections as each step arrives at the polished surface. From the film record, shock velocity and particle velocity can be measured for each step. These values are used with the Rankine-Hugoniot jump conditions to compute shock strength, density, and energy.

Shock velocity is claculated as

$$U = U_{app} \sin c.$$

The apparent velocity U_{app} is measured as the local cotangent of b. The emergence angle c is measured by knowing the individual line position on the polished surface relative to impact and by assuming a direct ray path between impact and arrival at the line position.

---

* V. G. Gregson, Jr. "Optical Lever Observation of Hypervelocity Impact Shock Waves," Journal of Applied Physics, Vol. 38, pp. 1798-1802, 1967.

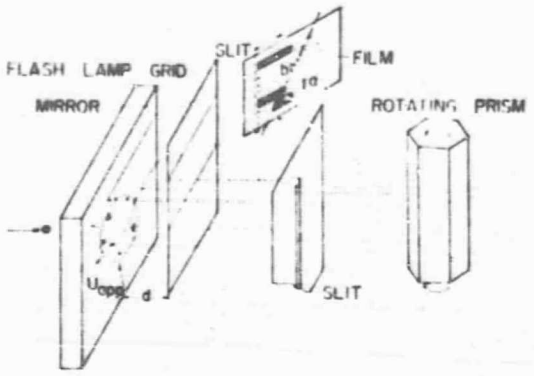

Figure 21 Optical Lever Technique

Particle velocity is calculated as

$$u = \left[U_{app} \sin(a/4d)\right] / \left\{\cos\left[c - \ldots 4d)\right]\right\},$$

where a is the deflection corrected for film demagnification. The usual free-surface approximation is used in computing the particle velocity for the main shock and ramp and is included in this relation.

The free-surface approximation is generally used to compute the amplitude of the elastic shock. This assumes a fluid behavior of the material. The term "pressure" is usually redefined as a "stress" which is normal to the wavefront. Errors in using this assumption for the elastic wave may be as much as 10% of the true stress amplitude. The free-surface approximation has not been used to compute particle velocity and stress of the elastic shock for this experiment. Instead an analysis is used which considers an incident elastic shock reflecting at a free boundary as another dilatational shock and a shear stress shock.

The energy of the incident compressional shock is proportioned between the two reflected shocks as a function of the incidence angle. From energy considerations of any shock, the total energy is partitioned equally between internal and kinetic energy. For most elastic shocks, the stresses are such that the slight temperature increase behind the shock front results in little of the available internal energy lost to propagate the shock. Assuming no energy is lost, the kinetic energy of an incident elastic shock can be proportioned between the kinetic energy of the two reflected shocks. The kinetic energy of a unit volume for the incident shock is

$$E = 1/2\rho_o u_1^2,$$

where E is the kinetic energy, u_1 is the particle velocity, and ρ_o is the material density before the shock arrival. The kinetic energy of a unit volume of the reflected shock is

$$E = 1/2\rho_o (u_2 + u_3)^2$$

where u_2 and u_3 are particle velocities of the dilatational and shear-stress shock respectively. If it is assumed that errors in an infinitesmal-amplitude-elastic-wave analysis, the reflected shock particle velocities can be described in terms of the incident particle velocity as

$$u_2^2 = (A_2/A_1)^2 u_1^2,$$

and

$$u_3^2 = (B_2/A_1)^2 (\phi/\psi) u_1^2.$$

A_2/A_1 is the amplitude ratio of the reflected compressional wave to the incident compressional wave. B_2/A_1 is the amplitude ratio of the reflected shear wave to the incident compressional wave. C_p and C_s are velocities for the compressional and shear waves respectively in

$$\phi \left[(U_{app}^2/C_p^2) - 1 \right]^{1/2} = \tan (\pi/2 - e),$$

and

$$\psi = \left[(U_{app}^2/C_s^2) - 1 \right]^{1/2} = \tan (\pi/2 - f).$$

The angle e is the angle between the free-surface and the incident compressional wave. The angle f is the angle between the free-surface and the reflected shear wave. The amplitude ratios are

$$\frac{A_2}{A_1} = \frac{4\mu\phi\psi - (\psi^2 - 1)\left[\lambda + \phi^2(\lambda + 2\mu)\right]}{4\mu\phi\psi + (\psi^2 - 1)\left[\lambda + \phi^2(\lambda + 2\mu)\right]}$$

and

$$\frac{B_2}{A_1} = \frac{-4\mu\phi\left[\lambda + \phi^2(\lambda + 2\mu)\right]}{4\mu^2\phi\psi + (\psi^2 - 1)\left[\lambda + \phi^2(\lambda + 2\mu)\right]}$$

where λ and μ are Lame' constants.

The optical lever deflection can be related to the particle velocity u_1 by extending the flow diagram of a hydrodynamic shock as shown in Figure 22. This extension will not depend upon the usual approximation that the free-surface velocity is twice the particle velocity. Instead, the optical lever deflection is equated to the surface rotations produced by each of the three shocks

$$1/2ad^{-1} = \delta_1 + \delta_2 + \delta_3,$$

where δ_1, δ_2, and δ_3 are the rotations associated with the incident compressional shock, the reflected dilatational shock, and the reflected shear stress shock respectively.

From the geometry of Figure 22,

$$\delta_1 = \tan^{-1}\left[u_1 \cos e/(U_{app} - u_1 \sin e)\right].$$

The surface rotation of the reflected compressional rarefaction is

$$\delta_2 = \tan^{-1}\left\{u_2 \cos(e + \delta_1)/\left[S_1 - u_2 \sin(e + \delta_1)\right]\right\},$$

where the streamline S_1 has a magnitude

$$S_3 = \left[(U_{app} - u_1 \sin e)/\cos\delta_1\right].$$

The surface rotation of the reflected shear stress rarefaction is

$$\delta_3 = \tan^{-1}\left[\frac{u_3 \cos(\pi/2 - f - \delta_1 - \delta_2)}{S_2 - u_3 \sin(\pi/2 - f - \delta_1 - \delta_2)}\right],$$

where the streamline S_2 has a magnitude

$$S_2 = \left\{\left[S_1 + u_2 \sin(e + \delta_1)\right]/\cos\delta_2\right\}.$$

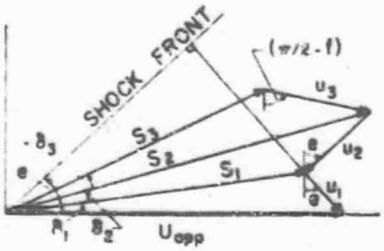

Figure 22 Two-Dimensional Flow Diagram for Incident and Reflected Elastic Shocks

One additional technique was added to the experiments. An optical fiber from the slit plane and viewing the target impact surface recorded the impact flash on the same film as the optical lever record. This permitted the total time for shocks to travel through the target to be measured.

The measured experimental values obtained are listed in Tables VI through XVI. Line numbers are simply relative numbers attached to the lines in the optical lever records. More important is the line spacing shown on each table. Distance traveled is the ray path distance from impact through the target to a specific line number.

The first and second time arrivals of the elastic and main shock fronts are measured from the time of impact. Several of the records had poor impact fiducials, thus show time arrivals relative to the back target surface only.

Particle velocity, shock velocity, and pressure are listed for each line that could be measured. The shock velocity of the peak ramp pressure and the main shock is taken to be the same value. The distinction between the elastic shock, ramp, and main shock is as follows.

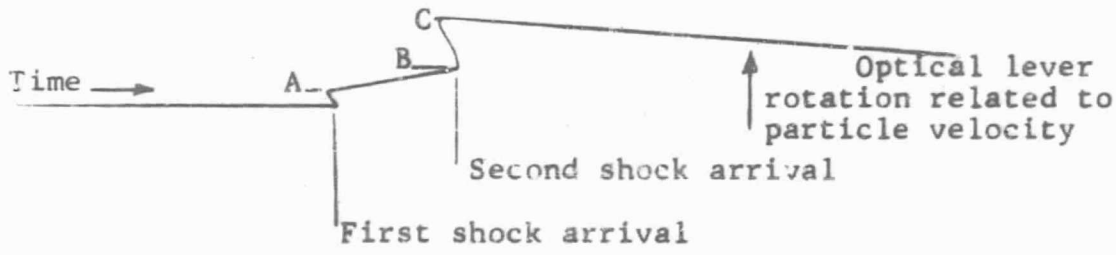

A - Elastic shock amplitude

B - Ramp amplitude

C - Main shock amplitude.

TABLE VI

EXPERIMENTAL VALUES ROUND 3 (IITRI 31)

Line Number	First Arrival ± 0.035 (μsec)
1	5.03
2	---
3	4.41
5	3.88
6	3.74
7	3.58
8	3.38
9	3.24
10	3.16
11	3.10
12	3.105
14	
15	
16	3.38
17	3.52
18	3.745
19	3.93
20	4.15

Line spacing 2.34mm
Off axis 5.5mm
Target - 0.754", 2024-T4 bar stock
Projectile - 5/32" diam, 2024-T3
@ 20,000 ft/sec.

TABLE VII

EXPERIMENTAL VALUES, ROUND 5 (IITRI 33)

		Elastic Shock				Ramp			Main Shock	
Line Number	Distance Traveled ±0.1 mm	1st Arrival ± 0.035 (μsec)	Particle Velocity (mm/μsec) ± 3%	Shock Velocity (mm/μsec) ± 3%	Pressure ± 6% (kb)	2nd Arrival ± 0.035 (μsec)	Particle Velocity (mm/μsec) ± 3%	Pressure ± 6% (kb)	Particle Velocity (mm/μsec) ± 3%	Shock Velocity (mm/μsec) ± 3%	Pressure ± 6% (kb)
1		3.09									
2		2.80									
3		2.59									
4		2.265				2.675					
5	25.4	2.055	0.0132	6.30	2.2	2.360	0.0234	3.7	0.0524	5.26	8.0
6	23.9	1.845	0.0212	6.34	3.6	2.085	0.0314	5.1	0.0750	5.41	11.7
7	22.5	1.652	0.0214	6.15	3.7	1.838	0.0324	5.3	0.0979	5.22	14.8
9	20.8	1.275	(0.0123)	(6.01)	(2.1)	1.462	0.0393	6.1	(0.0784)	5.27	(12.1)
10	19.7	1.150	(0.0073)	(5.88)	(1.3)	1.312	0.0311	4.8	(0.0932)	5.30	(14.1)
11		(1.075)				1.210					
12		-				(1.150)					
13		(1.035)				(1.150)					
14		(1.010)				1.175					
15	20.8	1.112				1.225	0.0323	5.3	0.1538	(5.32)	(22.8)
16	21.4	1.175	0.0140	(6.05)	(2.4)	1.308	0.0319	5.3	0.1068	(5.40)	(16.4)
17	22.5	1.312	0.0124	(6.02)	(2.1)	1.525	0.0361	6.1	0.1182	(5.45)	(17.2)
19	25.4	1.625	0.0170	6.35	2.9	1.862	-	-	0.0924	5.32	13.9
20	27.1	1.875	0.0159	6.23	2.7	2.155	0.0300	4.9	0.0637	5.38	9.8
21	28.8	2.100	0.0161	6.15	2.7	2.475	0.0265	4.2	0.0440	5.22	6.8
22	30.6	2.342	0.0144	6.08	2.5						
23		2.615									
24		2.922									
25		3.178									
26		3.525									
28		4.10									

Line spacing 2.39 mm. Off Axis 9.5mm.
Target - 0.754", 2024-T4 barstock
Projectile - 5/32" diam. 2024-T3 @ 21,000 ft/sec.

TABLE VIII

EXPERIMENTAL VALUES, ROUND 7 (IITRI 35)

		Elastic Wave				Ramp		Main Shock		
Line Number	Distance Traveled ± 0.1 mm	1st Arrival ± 0.017 (μsec)	Particle Velocity (mm/μsec) ± 3%	Shock Velocity (mm/μsec) ± 3%	Pressure ± 6% (kb)	2nd Arrival ± 0.017 (μsec)	Particle Velocity (mm/μsec) ± 3%	Pressure ± 6% (kb)	Particle Velocity (mm/μsec) ± 3%	Shock Velocity (mm/μsec) ± 3%	Pressure ± 6% (kb)
1		1.175									
2	27.2	0.846	0.0181	(6.05)	(3.1)	1.109	0.0238	(3.8)	0.0608	4.75	8.8
3	25.3	0.585	0.0111	(6.27)	(1.9)	0.795	0.0209	3.4	0.0767	5.65	12.2
4	23.4	0.389	0.0096	(6.15)	(1.6)	0.640	0.0179	2.9	0.0808	5.78	13.1
5	21.6	0.232				0.398			0.0893	5.69	14.2
6	19.9	0.095				0.299			0.0895	5.80	14.5
8		0.000				0.219					
9		0.000				0.212					
10	15.4	0.055				0.286			(0.1458)	5.96	(24.3)
11	15.1	0.137				0.373			(0.0947)	6.00	(15.8)
12	15.1	0.317	0.0113	(6.20)	(1.9)	0.568	0.0265	4.5	(0.0848)	6.20	(14.6)
13	15.6	-				0.810			0.0752	6.15	12.9
14	16.1	0.709	0.0063	(6.15)	(1.1)	0.997	0.0342	5.7	0.0802	5.93	13.3
15	17.2	1.013	0.0066	(6.25)	(1.1)	1.297	0.0337	5.6	0.0789	5.96	13.3
17	19.9	1.600									

Line spacing 2.39mm
Arrivals relative to back surface
Off Axis 2.0mm
( ) indicate less accurate value
Target - 0.590", 2024-T4 plate
Projectile - 5/32" diam. 2024-T3 @ 21,000 ft/sec.

TABLE IX

EXPERIMENTAL VALUES. ROUND 10 (IITRI 38)

		Elastic Shock				Ramp			Main Shock		
Line Number	Distance Traveled ± 0.1 mm	1st Arrival ± 0.017 (μsec)	Particle Velocity (mm/μsec) ± 3%	Shock Velocity (mm/μsec) ± 3%	Pressure ± 6% (kb)	2nd Arrival ± 0.017 (μsec)	Particle Velocity (mm/μsec) ± 3%	Pressure ± 6% (kb)	Particle Velocity (mm/μsec) ± 3%	Shock Velocity (mm/μsec) ± 3%	Pressure ± 6% (kb)
1	31.2	(3.015)									
2	29.0	(2.555)				2.800	0.0311	4.5	0.0387	5.20	5.7
3	26.9	2.175	(0.0228)	6.15	(3.9)	2.400	0.0304	5.0	0.0534	5.38	8.5
4	25.0	1.837	(0.0226)	6.08	(3.9)	2.018	0.0296	5.0	0.0661	5.50	10.6
6	20.9	1.231	(0.0228)	6.05	(3.9)						
7	19.1	0.928	(0.0228)	6.34	(3.9)						
8	17.5	0.629	(0.0224)	6.25	(3.8)						
9	15.9	0.408	(0.0189)	6.35	(3.2)						
10		0.246									
11		0.118									
12		0.047									
13		0.0									
14		0.092									
16		0.348									
17		0.642									
18		0.846									
19	18.9	1.120	(0.0255)	6.22	(4.4)	1.225	0.0259	4.5	(0.0813)	(5.38)	12.8
20	20.8	1.395		6.31		1.537	0.0270	(4.1)	(0.0867)	(5.42)	(13.2)
21	22.8	1.741	(0.0164)	6.17	(2.8)	2.005	0.0280	4.6	(0.0945)	(5.47)	(14.7)
22	24.8	2.095	(0.0144)	6.12	(2.5)	2.252	0.0294	4.8	(0.0594)	(5.45	(9.3)
23	26.8	(2.400)				2.680	0.0309	4.7	(0.0382)	(5.48)	(5.8)

Line spacing 2.38 mm
Off axis 2.5 mm

Time arrivals are relative to back surface.
( ) indicate less accurate values.

Target - 0.496", 2024-T4 plate.
Projectile 5/32" dia, 2024-T3, @ 21,500 ft/sec

TABLE V

EXPERIMENTAL VALUES, ROUND 11 (IITRI 39)

	Elastic Shock					Ramp		Main Shock		
Line Number	Distance Traveled ± 0.1 mm	1st Arrival ± 0.035 (μsec)	Particle Velocity (mm/μsec) ± 3%	Shock Velocity (mm/μsec) ± 3%	Pressure ± 6% (kb)	2nd Arrival ± 0.035 (μsec)	Particle Velocity (mm/μsec) ± 3%	Pressure ± 6% (kb)	Particle Velocity (mm/μsec) ± 3%	Shock Velocity (mm/μsec) ± 3%	Pressure ± 6% (kb)
1	27.7	4.455	0.0184	6.29	3.2						
2	25.4	4.085	0.0184	6.32	3.2						
3	23.2	3.725	0.0174	6.35	3.0						
5	18.7	3.040	0.0259	6.23	4.4	3.365	0.0309	5.1	0.0976	5.45	14.8
6	16.6	2.675	0.0260	6.15	4.5	2.862	0.0324	5.5	0.101	6.11	17.0
7	14.5	2.344	0.0255	6.25	4.4	2.463	0.0256	4.4		6.04	
8	12.6	2.052	0.0261	6.17	4.5	2.148					
9	10.9	1.767	0.0288	6.05	4.9	1.850					
10		1.522									
11		1.375									
12		1.315									
13		1.347									
15		1.636									
16	12.6	1.886	0.0268	6.38	4.6	1.992					
17	14.5	2.171	0.0242	6.42	4.3	2.326					
18	16.6	2.493	0.0248	6.22	4.4	2.707	0.0268	4.6	0.1095	5.43	17.4
19	18.7	2.850		6.17		3.100	0.0378	(5.6)		5.34	
20	20.9	3.205		6.10		3.515	0.0381	(5.2)	0.0770	4.92	10.6
21		3.575		6.22							

Line spacing 2.41 mm. Target-0.318", 2024 - T4 plate.
Off axis 3.0 mm. Projectile-5/32" dia, 2024 - T3, @ 20,400 ft/sec.

TABLE XI

EXPERIMENTAL VALUES, ROUND 12 (IITRI 40)

		Elastic Shock				Ramp		Main Shock		
Line Number	Distance Traveled ± 0.1 mm	1st Arrival ± 0.035 (μsec)	Particle Velocity (mm/μsec) ± 3%	Shock Velocity (mm/μsec) ± 3%	Pressure ± 6% (kb)	2nd Arrival ± 0.035 (μsec)	Particle Velocity (mm/μsec) ± 3%	Pressure ± 6% (kb)	Particle Velocity (mm/μsec) ± 3%	Shock Velocity (mm/μsec) ± 3%	Pressure ± 6% (kb)
1	20.8	3.275				3.640	0.0375	6.1	0.0844	5.67	13.3
2	18.2	2.920				3.202	0.0389	6.1	0.118	5.65	15.5
3	16.1	2.562	0.0155	(6.22)	(2.7)	2.862	0.0336	5.4	0.125	5.35	19.1
4	14.1	2.169	0.0134	(6.25)	(2.3)	2.432	0.0339	5.2	0.160	5.25	23.4
6		1.574				1.772					
7		1.401				1.574					
8		1.390				1.515					
9		-				1.517					
10		1.416				1.603					
11	10.7	1.616				1.828			0.201	5.20	29.2
12	12.2	1.885				2.126	0.0397	5.9	0.175	5.34	26.0
13	14.1	2.197				2.481	0.0358	5.2	0.154	5.22	22.4
15		2.960				3.218					

Line spacing 2.46 mm. Target-0.344", 2024-T4 plate. Projectile-5/32" dia, 2024-T3 @ 19,900 ft/sec.
Off axis 5.5 mm. ( ) indicate less accurate data.

TABLE XII

EXPERIMENTAL VALUES, ROUND 13 (IITRI 41)

Main Shock

Line Number	Distance Traveled ± 0.1 mm	1st Arrival ± 0.026 (μsec)	2nd Arrival ± 0.026 (μsec)	Particle Velocity (mm/μsec) ± 3%	Shock Velocity (mm/μsec) ± 3%	Pressure ± 6% (kb)	1st Reverberation ± 0.026 (μsec)	2nd Reverberation ± 0.026 (μsec)	3rd Reverberation ± 0.026 (μsec)	4th Reverberation ± 0.026 (μsec)
1									5.50	6.15
2									5.16	
3							3.617	4.28	4.84	
4		2.974					3.274	4.01	4.54	
5		2.534	2.604				2.994	3.64		
6		2.116	2.184				2.651	3.36		
7		1.774	1.814				2.304			
8	10.4	1.426	1.494	0.293	6.27	51.2				
10		0.794								
11		0.580								
12		0.501								
13		0.594								
14		0.872								
15		1.149					1.309			
16	10.4	1.564		(0.093)	(5.55)	(15.2)	1.744			
17		1.979					2.256			
19		2.799					3.092	3.834	4.28	
20								4.174	4.63	
21									5.00	
22									5.35	
23									5.72	
24									6.13	

Line spacing 2.48 mm.
Off axis 2.5 mm.

Target - 0.128", 2024-T4 plate.
Projectile - 5/32" dia, 2024-T3 @ 20,000 ft/sec.

TABLE XIII

EXPERIMENTAL VALUES, ROUND 14 (IITRI 42)

Main Shock

Line Number	Distance Traveled ± 0.1 mm	1st Arrival ± 0.026 (μsec)	2nd Arrival ± 0.026 (μsec)	Particle Velocity (mm/μsec) ± 3%	Shock Velocity (mm/μsec) ± 3%	Pressure ± 6% (kb)	1st Reverberation ± 0.026 (μsec)	2nd Reverberation ± 0.026 (μsec)	3rd Reverberation ± 0.026 (μsec)
1								6.494	
2								6.044	6.744
3								5.694	6.354
4							4.014	4.954	5.364
5							3.634	4.404	
6		2.754					3.244	3.934	
7	15.4	2.294		0.0979	6.02	16.5	2.864	3.604	
8	13.0	1.879		.173	6.02	29.0	2.444		
9	10.5	1.479	1.592	0.234	6.06	39.6	1.664		
10	8.2		1.142	0.447	6.06	75.6			
11		0.699					1.109		
12		0.554							
13		0.491							
14		0.646							
15		0.981							
16	8.2	1.341		0.342	6.3	60.4			
17	10.5	1.674		0.224	(6.6)	(43.0)	(2.067)		
18		2.084					2.629		
20		3.139					4.094		
21							4.654		
22							5.474		
23							5.814		
24							6.134		

Line spacing 2.51 mm.
Off axis 2.0 mm.

Target - 0.127" 2024-T4 plate
Projectile 5/32" dia, 2024-T3, @ 19,900 ft/sec.

TABLE XIV

EXPERIMENTAL VALUES, ROUND 14 (IITRI 43)

		Elastic Shock				Ramp			Main Shock		
Line Number	Distance Traveled ± 0.1 mm	1st Arrival ± 0.026 (μsec)	Particle Velocity (mm/μsec) ± 3%	Shock Velocity (mm/μsec) ± 3%	Pressure ± 6% (kb)	2nd Arrival ± 0.026 (μsec)	Particle Velocity (mm/μsec) ± 3%	Pressure ± 6% (kb)	Particle Velocity (mm/μsec) ± 3%	Shock Velocity (mm/μsec) ± 3%	Pressure ± 6% (kb)
1		(7.40)		6.17							
2		7.04		6.17							
3		6.695		6.19							
4	40.5	6.340	0.0187	6.16	3.2						
5	38.4	6.015	0.0181	6.15	3.1						
6	36.4	5.665	0.0181	6.16	3.1						
7	34.4	5.272	0.0179	6.12	3.1	5.680	0.0257	4.3	0.0382	5.45	6.2
9	30.5	4.598	0.0178	6.19	3.1	4.970	0.0228	3.8	0.0455	5.42	7.1
10	28.7	4.298	0.0171	6.14	2.9	4.615	0.0241	3.9	0.0630	5.46	9.9
11	27.0	4.002	0.0179	6.28	3.1	4.322	0.0324	5.4	0.0636	5.34	9.9
12	25.4	3.724	0.0149	6.14	2.6	3.970	0.0342	5.6	0.0796	5.52	12.6
13	23.6	3.495	0.0198	6.28	3.4	3.708	0.0364	6.0	0.0902	5.66	14.5
14	22.5	3.257	0.0157	6.26	2.7	3.456	0.0267	4.4	0.107	5.50	16.7
15	21.8	3.070	0.0133	6.26	2.3	3.252	0.0287	4.6	0.111	5.37	16.8
16	20.8	2.956	0.0156	6.30	2.7	3.063	0.0253	4.2	0.110	5.40	18.4
17	19.7	2.818	0.0138	-	2.4	2.956					
19		2.750				2.880					
20	-					2.891					
21	19.7	2.813		6.22		2.924			0.1005	5.70	16.0
22	20.8	2.880	(0.0110)	6.29	(1.9)	3.031	(0.0214)	(3.5)	0.1070	5.65	17.0
23	21.8	3.036	0.0159	6.27	2.7	3.182	0.0304	4.9	0.1220	5.50	19.0
24	22.5	3.206	0.0168	6.26	2.9	3.375	0.0318	5.2	0.1215	5.56	19.2
25	23.6	3.432	0.0152	6.35	2.6	3.608	0.0319	5.2	0.0988	5.55	15.5
26	25.4	3.658	0.0161	6.00	2.8	3.885	0.0278	4.5	0.0914	5.10	13.4
28	28.7	4.222	0.0095	6.10	1.6	4.505	0.0265	4.0	0.0485	5.08	7.1
29	30.5	4.510	0.0099	6.10	1.7	4.910	0.0280	4.4	0.0525	5.28	8.0
30	32.4	4.801	0.0090	6.01	1.5	5.200	0.0286	4.4	0.0472	5.26	7.1
31	34.4	5.160	0.0092	6.16	1.6	5.590	0.0228	3.6	0.0315	5.40	5.0
32	36.4	5.480	0.0054	6.16	0.9	5.990					
33	38.4	5.840	0.0058	6.06	1.0						
34		6.255		6.12							

Line spacing 2.38 mm. Target 0.753", 2026-T4 plate. Projectile 5/32", 2024-T3 @ 19,500 ft/sec.
Off axis 2.0 mm. ( ) indicate less accurate value

TABLE XV

EXPERIMENTAL VALUES, ROUND 15 (IITRI 43)

Reverberations

Line Number	1st Reverberation ± 0.026 (μsec)	2nd Reverberation ± 0.026 (μsec)	3rd Reverberation ± 0.026 (μsec)
12	5.915		
13	5.125	5.940	
14	4.470	5.315	
15	4.095	4.800	
16	3.920	4.550	
17	3.845		
19	3.860		
20	3.870		
21	3.960		4.910
22	4.020	4.375	5.000
23	4.110	4.660	5.355
24	4.360	5.220	5.845
25	4.840	5.540	6 460
26	5.665	6.415	

TABLE XVI

EXPERIMENTAL VALUES, ROUND 18 (IITRI 46)

Main Shock

Line Number	Ray Path ± 0.1mm	1st Arrival ± 0.026 (μsec)	2nd Arrival ± 0.026 (μsec)	Particle Velocity (m/μsec) ± 5%	Shock Velocity (m/μsec)	Pressure ± 10% (kb)
1		2.195				
2		1.822				
3	12.7	1.421	1.506	0.255	(6.6)	47
4		1.111				
5		0.786				
6	6.4	0.525		(1.00)	---	(184)
8	5.2	0.442		(1.03)	---	(187)
9		0.559				
10		0.820				
11		1.120	1.181			
12	12.7	1.463	1.596	0.218	5.57	33.8
13		1.890	2.050			
14		2.225				
15		2.595				

Line spacing 2.50mm. Off axis 2.0mm from center line.
Fiber optic data uncertain - time too short. High pressure shock velocity uncertain because of high apparent velocity with large reading error.
Target - 0.189", 2024-T4, plate.
Projectile - 5/32" diam, 2024-T3, @ 20,900 ft/sec.

Later plate reverberations are listed for the experiments that record such behavior. An estimate of the reverberation amplitudes indicate that they do not exceed the dynamic yield amplitude of the material (~6.0 to 6.5 kb). For plates thin enough to be perforated, the origin of the reverberation occurs at the lip of the perforation at both the front and back slides of the plate. For plates thick enough to spall, the origin of the reverberation is the shock trapped within the spall.

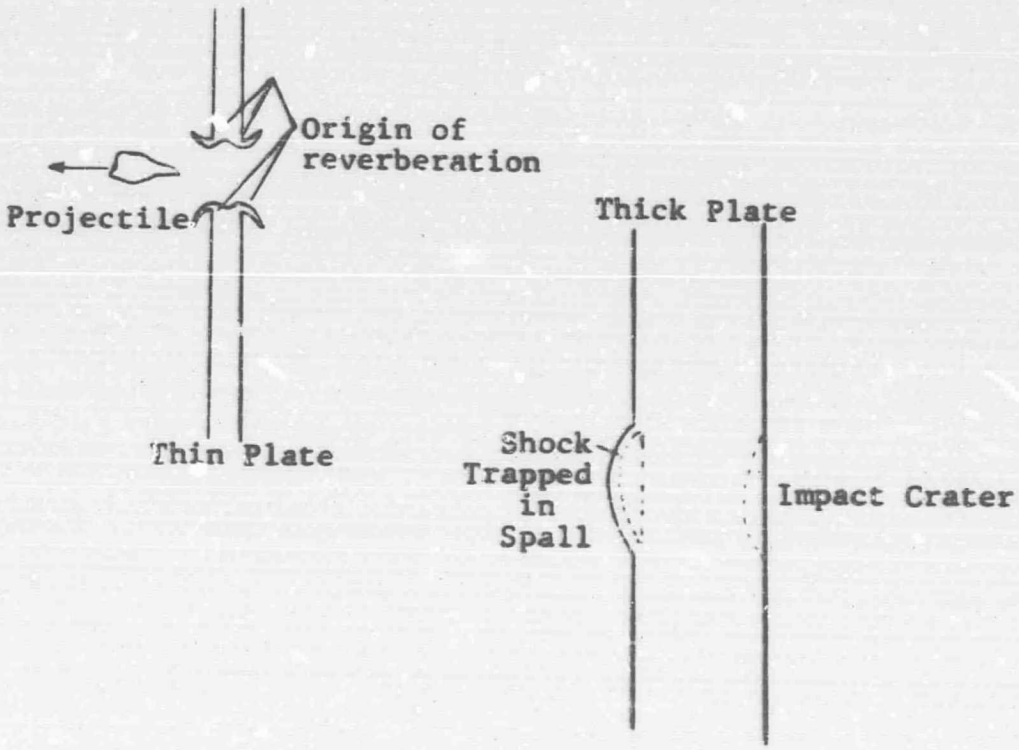

Experiments for which no data were recorded or experiments with extremely poor data recovery are not included in the tabulations, or further discussed. Such failures ranged from poor optical alignment to premature projectile firing before streak camera attained adequate recording speed. In general, data recovery was quite good.

Figure 23 is a copy of the best optical lever record taken in hypervelocity experiments (Round 15) and clearly shows the impact flash fiducials together with the optical lever deflections and later spall reverberations.

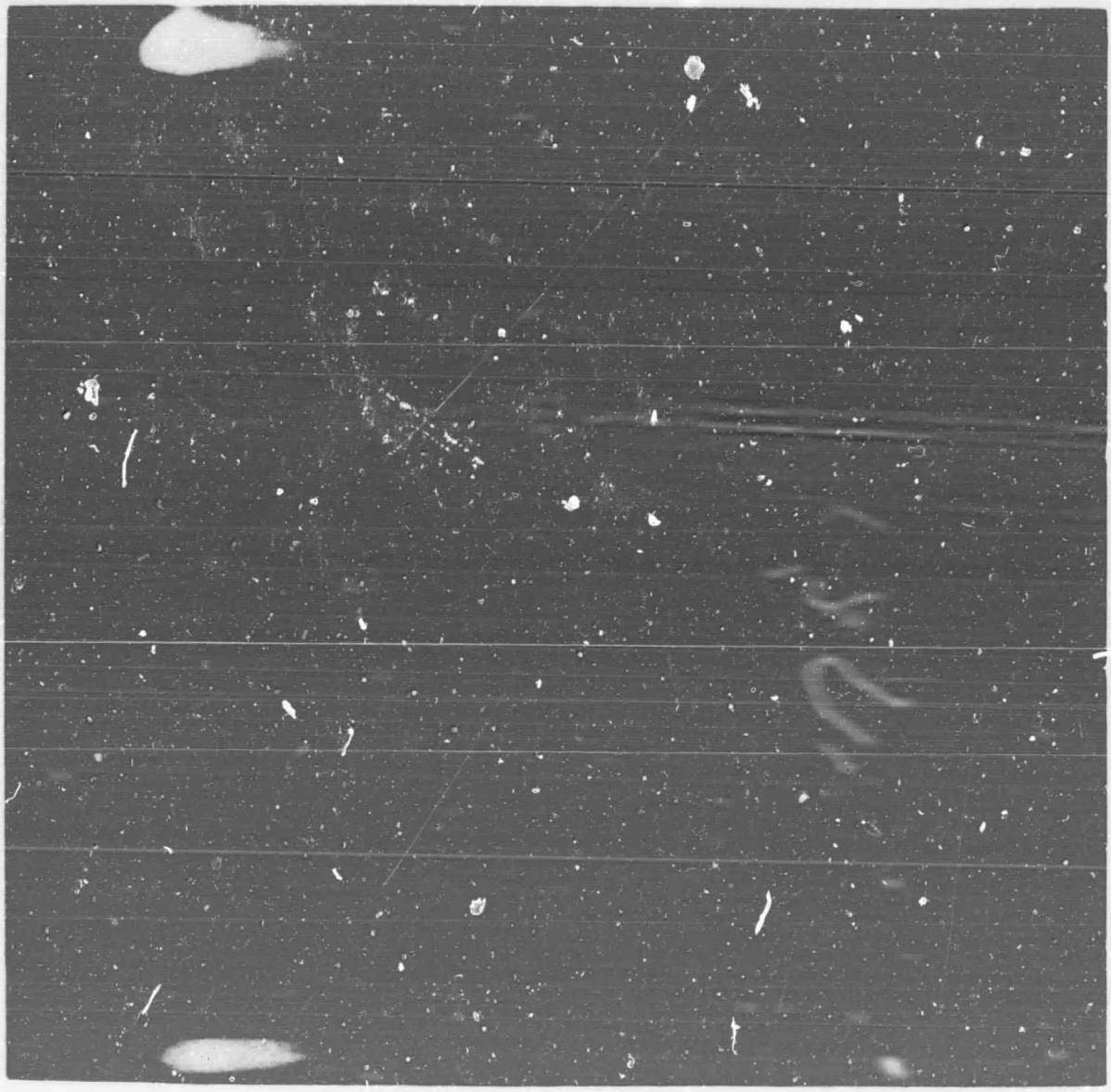

Figure 23 Round 15 (IITRI 43) Photograph Showing Projectile Impact Flash (at Top and Bottom) and Time for Shock Travel through Target

Also shown is the optical lever deflections related to the elastic shock, ramp, and main shock. Reverberations in the spall follow the main shock. Time horizontal - 1mm = 0.567 μsec. Line spacing vertical - 1 space = 2.38mm.

Figure 24 shows the arrival times of three target thicknesses (Round 12, 14, and 15). Figure 25 is a pressure-particle velocity plot of the data together with data by Fowles.*

Three experiments (Round 13 (IITRI 41), Round 14 (IITRI 42), and Round 18 (IITRI 46) were designed to try and measure pressures within the range of 100 to 300 kb. These are thin targets and the arrival times of Round 14 (IITRI 42) are shown in Figure 24 to illustrate this group of experiments. To obtain the desired pressures, optical lever deflections would have to be observed very near the direct ray path through the target. This occurred on one experiment Round 18 (IITRI 46), however, there were rather larger error limits attached to the apparent shock velocity, thus reducing the accuracy of the data. The other two experiments resulted in optical lever deflections a few millimeters to either side of the direct ray path. This longer travel time resulted in shock decay (which is quite rapid) such that the recorded pressures of 40 to 80 kb were not within the desired range even though pressures of ~300 kb did occur along the direct ray path. These experiments demonstrate the feasibility of using this technique within the pressure region of several hundred kilobars. However, any additional experiments should be performed with a streak camera capable of a faster writing rate so that a more accurate measure of the apparent shock velocity is obtained.

The experiments designed to obtain shock arrival times, velocities, and pressures above and below the ballistic limit were Round 11 (IITRI 39), Round 12 (IITRI 40), Round 9 (IITRI 37), Round 10 (IITRI 38), and Round 7 (IITRI 35), Round 8 (IITRI 37), respectively. The arrival times of these experiments are designated by Round 12 (IITRI 40) in Figure 24. No deviation could be measured in the shock decay as a function of travel nor in the pressure levels or arrival times between penetration and no penetration. Some difference might be detected if the analysis were extended to include a total time history of the pulse as it decayed.

The experiments designed to obtain shock arrival times, velocities, and pressures above and below the spall limit were Round 7 (IITRI 35), Round 8 (IITRI 36), and Round 3 (IITRI 31), Round 5 (IITRI 33), Round 15 (IITRI 43), respectively.

---

* R. Fowles, Shock Wave Compression of Hardened and Annealed 2024 Aluminum, Journal of Applied Physics, Vol. 32, p. 1475-1487, 1961.

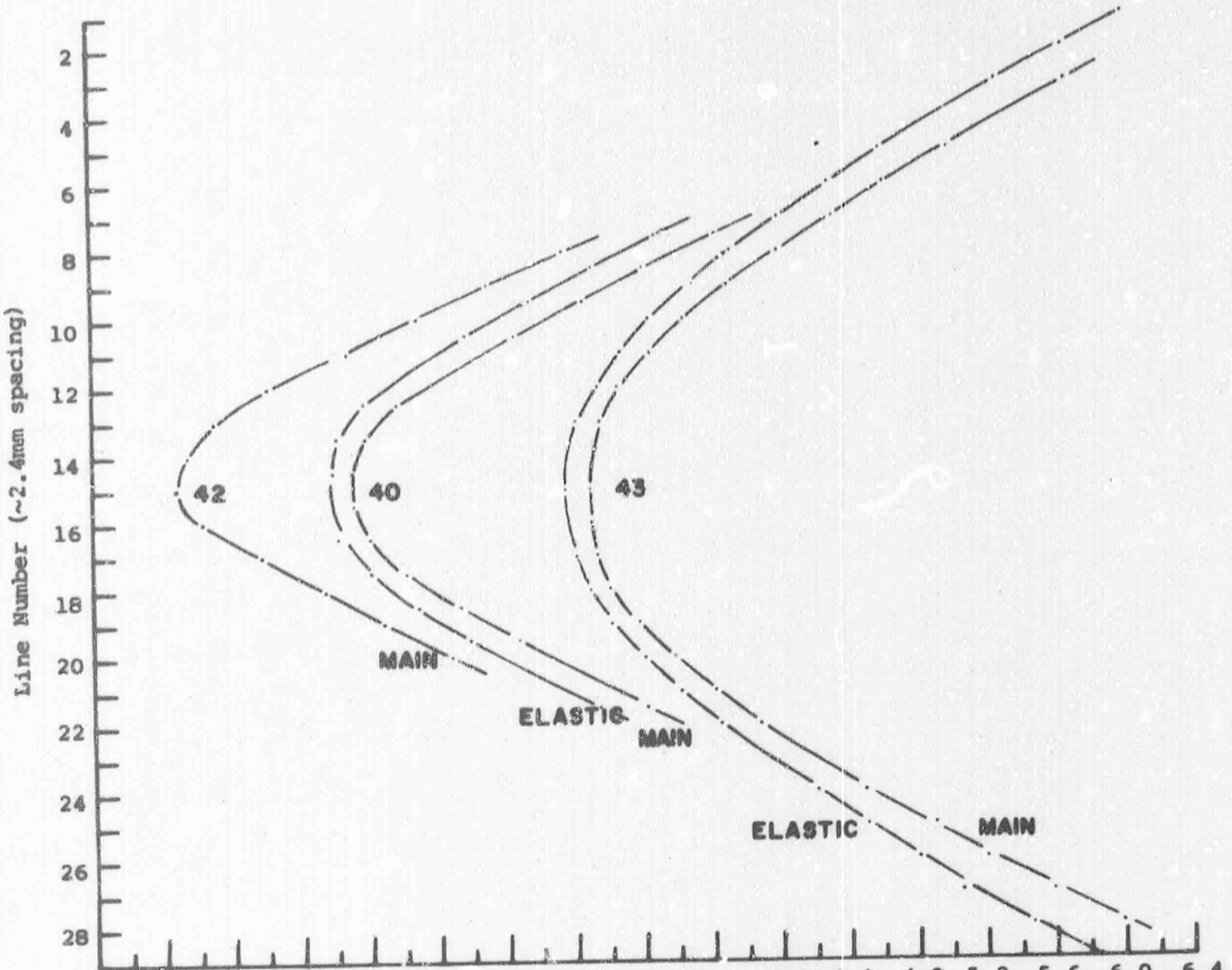

Figure 24 Arrival Time

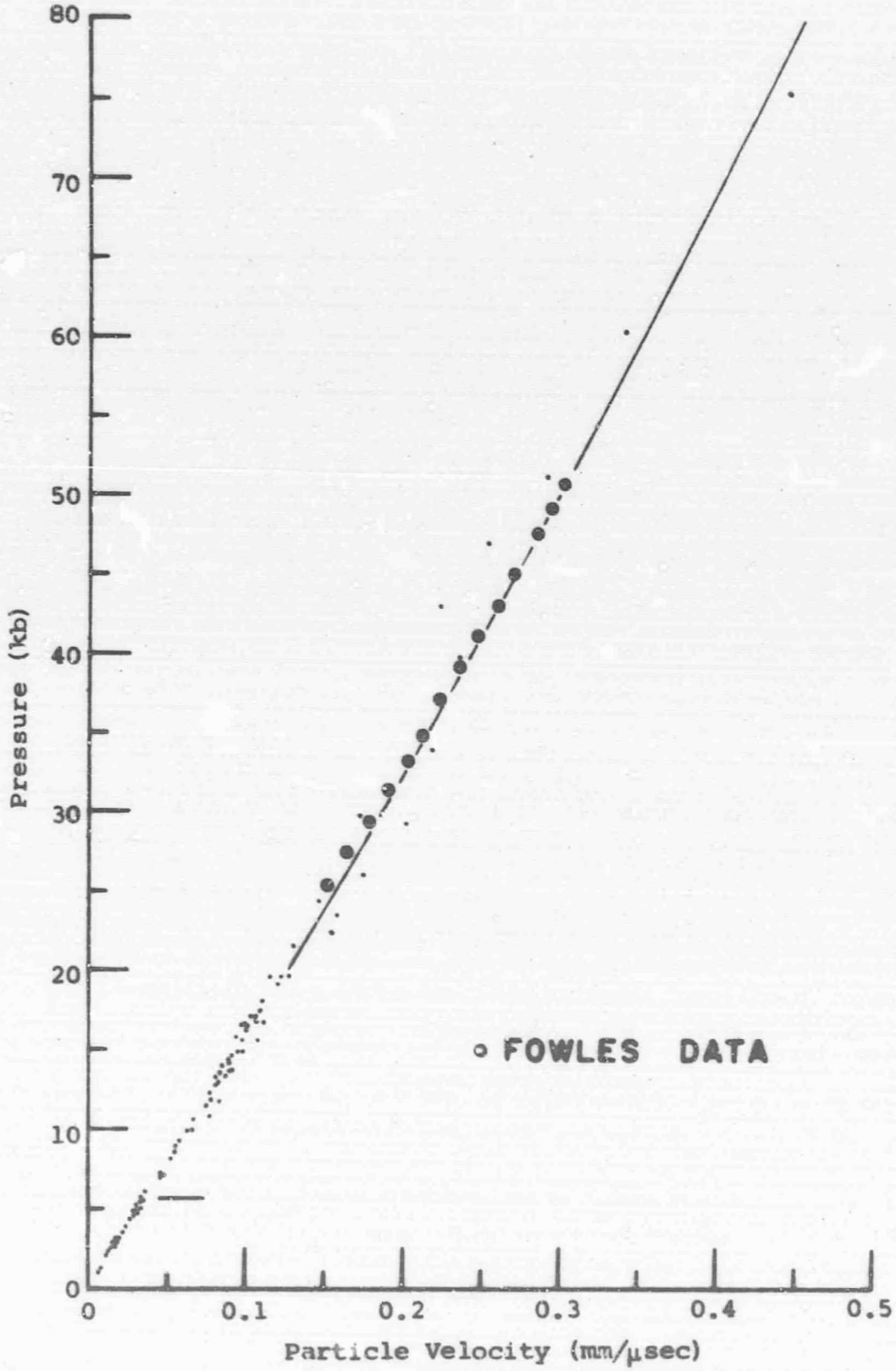

Figure 25 Pressure as a Function of Particle Velocity

Round 16 (IITRI 44), and Round 17 (IITRI 45) were considered to be at the spall limit. The arrival times of these experiments are illustrated by Round 15 (IITRI 43), in Figure 24. No deviation could be measured in the shock decay as a function of travel nor in the pressure levels and arrival times between spall and no spall. Again some difference might be detected if the analysis were extended to include a total time history of the pulse.

Round 3 (IITRI 31) and Round 5 (IITRI 33) were bar stock while Round 17 (IITRI 45) was plate stock aluminum. Differences in spall were detected between bar stock and plate stock for thinner targets as well as differences in bulge characteristics for these thicknesses. It was hoped that this would be expressed in the pressure levels and decays but none were detected. Some difference might be apparent if a total time analysis were made. However, some experiments should be repeated because the experiments were keyed to the peak pressures resulting in less precise measurements of the elastic wave. The repeated experiments should concentrate on the elastic wave because small difference between plate and bar stock should be evident in the elastic wave pressures and decays.

Phase III Ionization Experiments

The main objective of this phase was to make a series of experimental light-gas gun firings, designed to obtain measurements of the bubble growth, ionization and radiation resulting from the impact. The effort was divided into three parts:

1. Establishment of Projectile Design for Experiments

2. Bubble Growth (Photographic and Radiographic) Measurement

3. Ionization Measurement

A series of three experiments was covered with additional instrumentation furnished by NASA. In particular, sequential self-illuminated pictures of impact bubbles, using NASA's TRW image-converter framing camera, were sought.

Before beginning on the experimental firings, a special high-vacuum chamber and instrumentation had to be fabricated. This task was undertaken early in the program and accomplished concurrently with the Phase I and II experiments. The high-vacuum chamber was designed, fabricated and checked out before the completion of the Phase II

experiments. Special instrumentation for the charge measurement was also designed early in the program. Circuits were assembled, checked out, and calibrated prior to any experimental firings.

It was originally suggested that the high-vacuum chamber be sealed from the range vacuum by a thin Mylar diaphragm. The projectile would penetrate the diaphragm, then impact on a target within the high-vacuum chamber. The measurements were to be made on the ejecta from the impact side of the target. However, the program was revised to eliminat the Mylar diaphragm. Instead a thin target was used to provide the required seal between the high-vacuum section and range. The measurements were made on the bubble growth on the backface of the target. This change required minor revisions in the method of retaining the target. These changes were made with no difficulty and aided in obtaining better data. It assured that no projectile break-up would occur from hitting the Mylar diaphragm, and that contaminated particles from the Mylar would not enter into the ionization of spectro measurements.

The hypervelocity range facility and launcher used for these experiments are shown schematically in Figure 26. The launcher is an accelerated reservoir-type light-gas gun consisting of a propellant chamber a 20mm pump section, a high-pressure section, and a 22-caliber launch tube. Although smooth bore and rifled launch tubes were employed in the initial experiments, the majority and meaningful experiments were made with the rifled launch tube. The range section has three basic components: the blast tank, a range section, and the special high-vacuum target chamber. The blast tank serves to expand the gun gases following the projectile. The range section is equipped with regularly spaced viewing stations at which are located the velocity detectors and image converter cameras. The special target chamber is sealed from the range by the target, has its own vacuum system and is provided with four ports for instrumentation.

A schematic for the velocity instrumentation is shown in Figure 27. The system employs photomultiplier light detectors to determine times of arrival at the velocity stations. Luminousity from the projectile causes a current flow in the PM detectors reaching a peak directly under the detector. Time between stations is measured from peak to peak of the respective stations from the record of the oscilloscope.

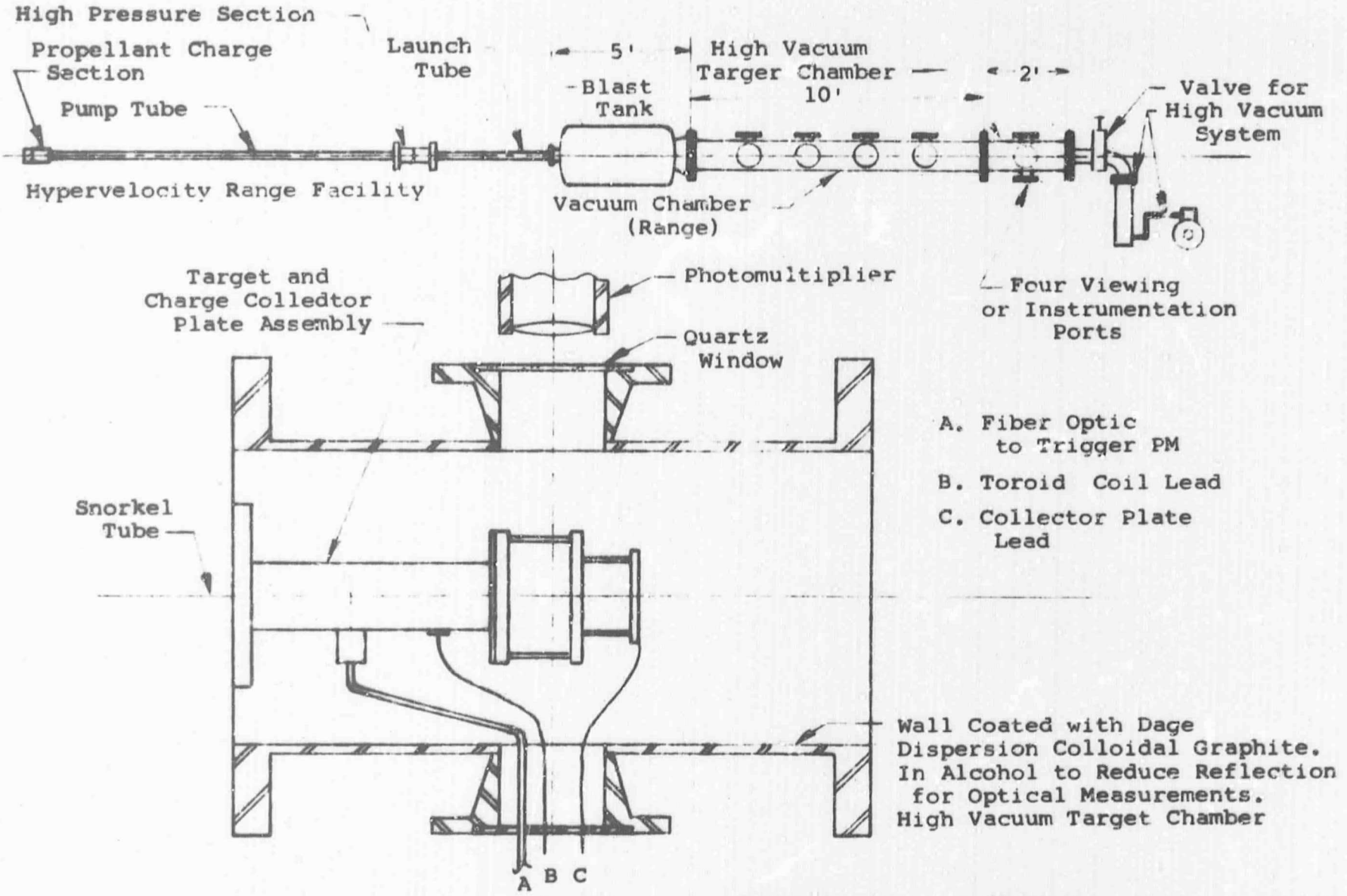

Figure 26 Hypervelocity Range and High-Vacuum Target Chamber

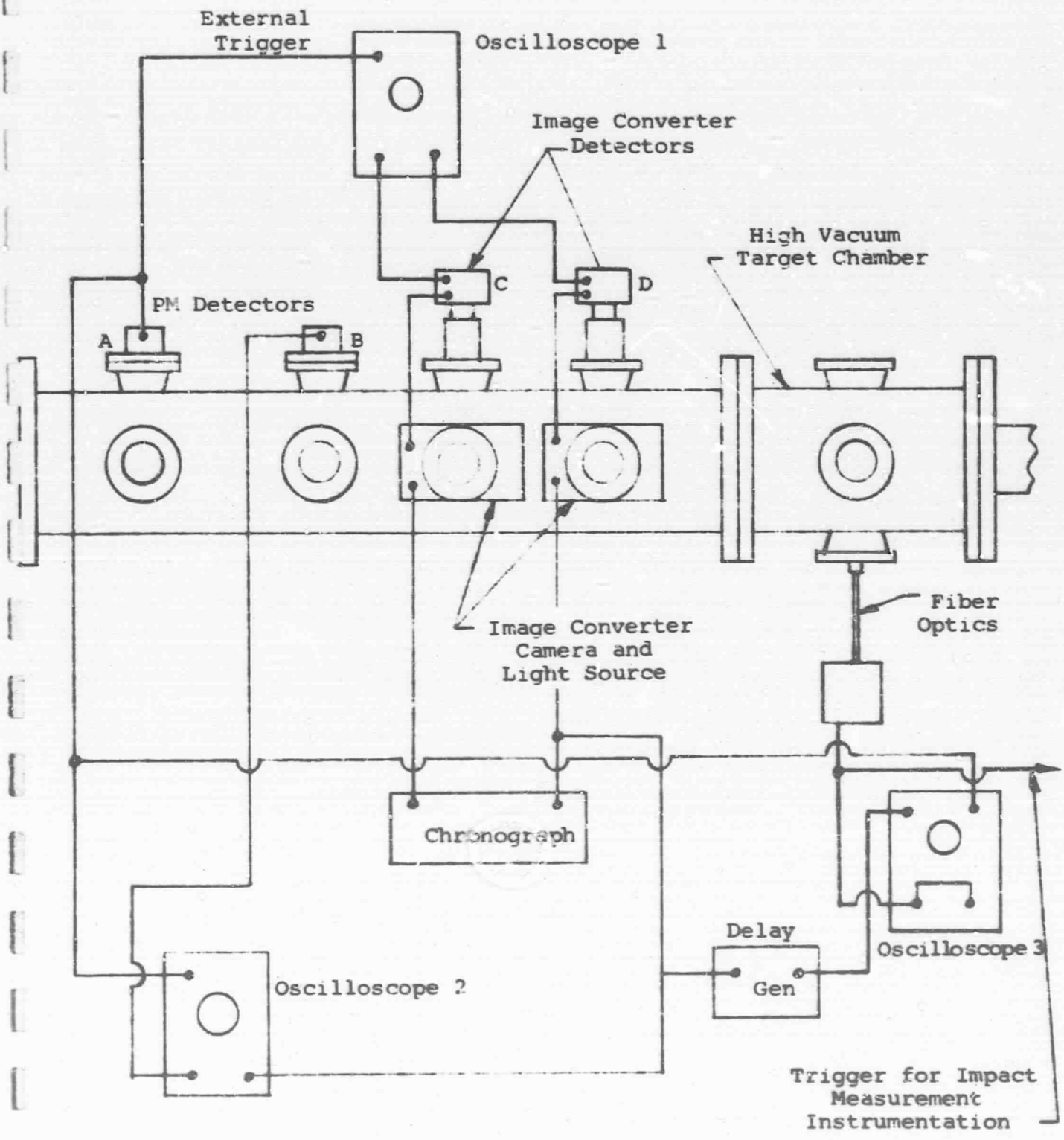

Figure 27 Velocity Instrument

The photomultiplier detector at station A is used as a trigger source on oscilloscopes 1 and 2 and also triggers one channel on oscilloscope 3. Oscilloscope 1 monitors the image converter at C and D from which projectile time between the stations is determined. Oscilloscope 2 monitors stations B and D to obtain flight time between these stations. The photomultiplier at location E is triggered by means of a fiber optic light pipe. It monitors the projectile 6 in. ahead of target. Output from this PM records on oscilloscope 3. One channel is triggered by the PM at A and the other by the image converter camera trigger pulse. The primary purpose of the E target PM is to provide a trigger for the target measurement instrumentation, but it is monitored also to provide back-up velocity measurements of the projectile. Since the scopes have a common trigger (A) then flight time between any of the stations can be determined.

The most accurate time-lapse measurements are obtained from the chronograph that incorporates a precise timing generator that can be read directly. The chronograph is started when the image converter camera at C is triggered and stopped when camera at D is triggered. Because of the sensitivity and slight variation in signal from the projectile, the Polaroid record from the image converter shows a small variation in position from station to station. Correction for the slight variation in distance is made and, using the accurate time from the chronograph is used to calculate the projectile velocity. The other elapse time measurements are used as back-up to the image converter camera setup for the occasions when some of the image converter data are missed. The velocity calculated from the back-up instrumentation has been found to be within 5 percent of the verified velocity.

A special target chamber was designed to meet the vacuum requirements for Phase III. An existing 2-ft-long piece of range section was modified for this design. The target chamber and its own vacuum system are shown in Figure 28. There are three basic elements to the system; a target chamber, a vacuum pump system, and target mounting assembly. The chamber is 1-ft ID by 2-ft long and contains four 4-in. ports for instrumentation, spaced 90 degrees apart at the center of the section. To minimize the outgassing problem during pump-down, the chamber was nickel-plated.

The vacuum pump system was a very simple and practical design, consisting of a mechanical pump, a diffusion pump, a vacuum valve and a flange with baffle assembly for mounting onto the target chamber. The entire unit is mounted on

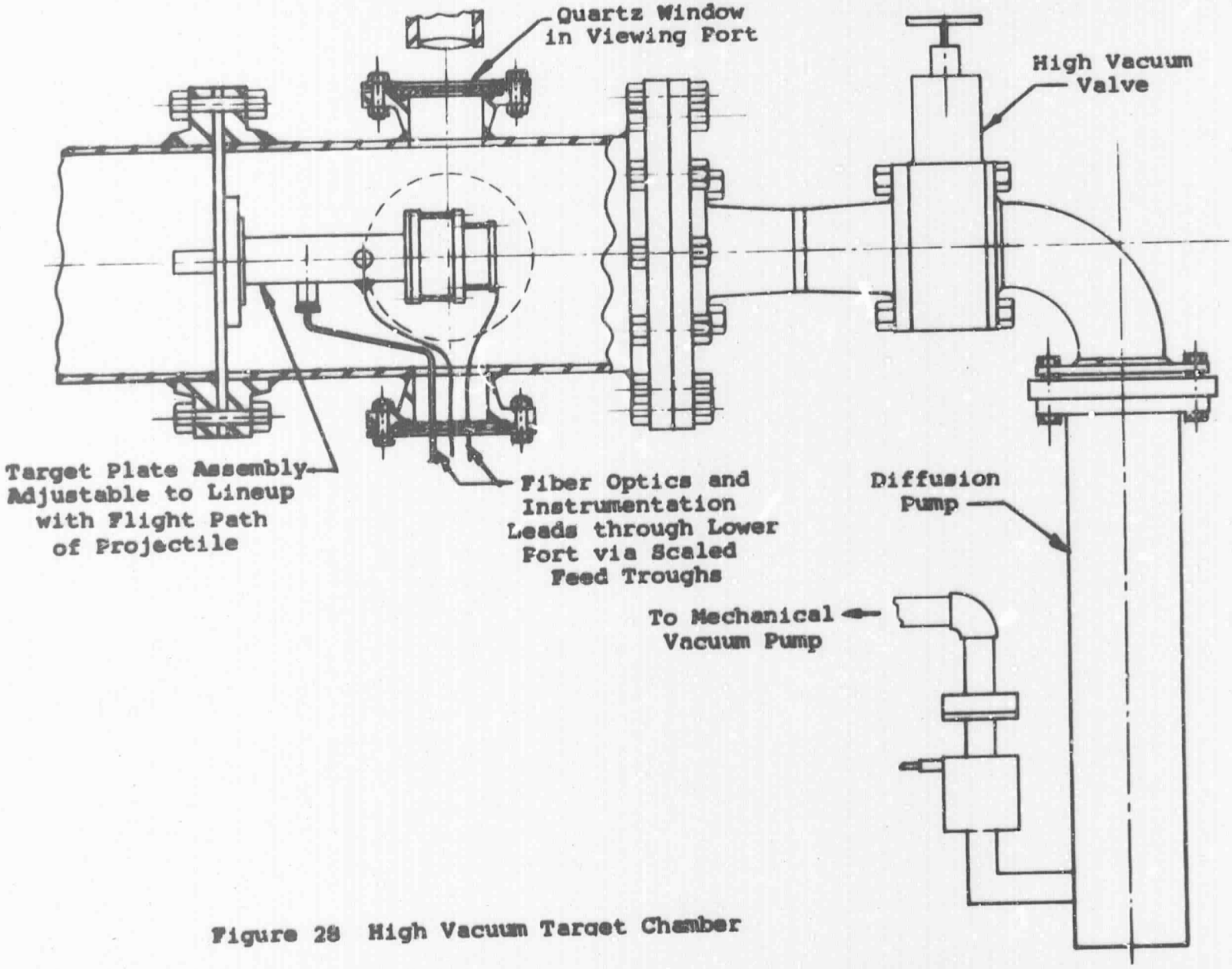

Figure 28 High Vacuum Target Chamber

casters to facilitate movement and permit clear access for inserting the target-mounting assembly. A pump-down time of approximately 12 hours was required to obtain a vacuum in the chamber of 2.5 to 4.0 x 10^{-5} torr. A longer pump-down time over a weekend resulted in lowering the pressure to 3.5 x 10^{-6} torr. All of the test data were in the 2.5 to 4.0 x 10^{-5} torr range.

The target mounting assembly is shown in Figure 29. It is mounted to a 1/2-in. thick aluminum bulkhead between the range and test chamber. The mounting design permits the assembly to line up with the flight path of the projectile. It has been found, in bore sighting, that the on-aim point for any launch tube is not necessarily the impact point. Further it has been found that the impact point will remain constant if the relative location of the launch tube is held constant from shot to shot. It is possible to adjust the location of the launch tube to hit a particular aim point, but it has been found to be more practical to locate the target at the impact point.

The target mounting assembly also contains a viewing port 6 in. ahead of the target. The viewing port is monitored by a photomultiplier tube via a fiber optic light pipe. The radiated light from the projectile provides a signature via the PM tube to trigger the instrumentation for monitoring the impact phenomena. By adjusting the aperature, a trigger signal with response time of several microseconds was obtained, and remained constant from shot to shot.

Approximately 3 in. ahead of the target is located the toroid coil assembly to measure the charge on the projectile before impact. The grid for the charge collection measurement also is monitored on the target assembly. It is designed to employ either a cylindrical grid as shown in Figure 29 or a flat-plate grid parallel to the target plate.

The target plate was insulated by mounting the target on lucite rings. The O-ring between the target and lucite mounting ring maintains the pressure differential between the high-vacuum chamber and the range.

To facilitate the assembly operation when replacing the target, charge collection grid, and other components that may be damaged during the test firings, the entire mounting assembly was removed from the chamber. Exact relocation of the assembly was obtained by piloting on the aluminum tube at the forward end of the assembly.

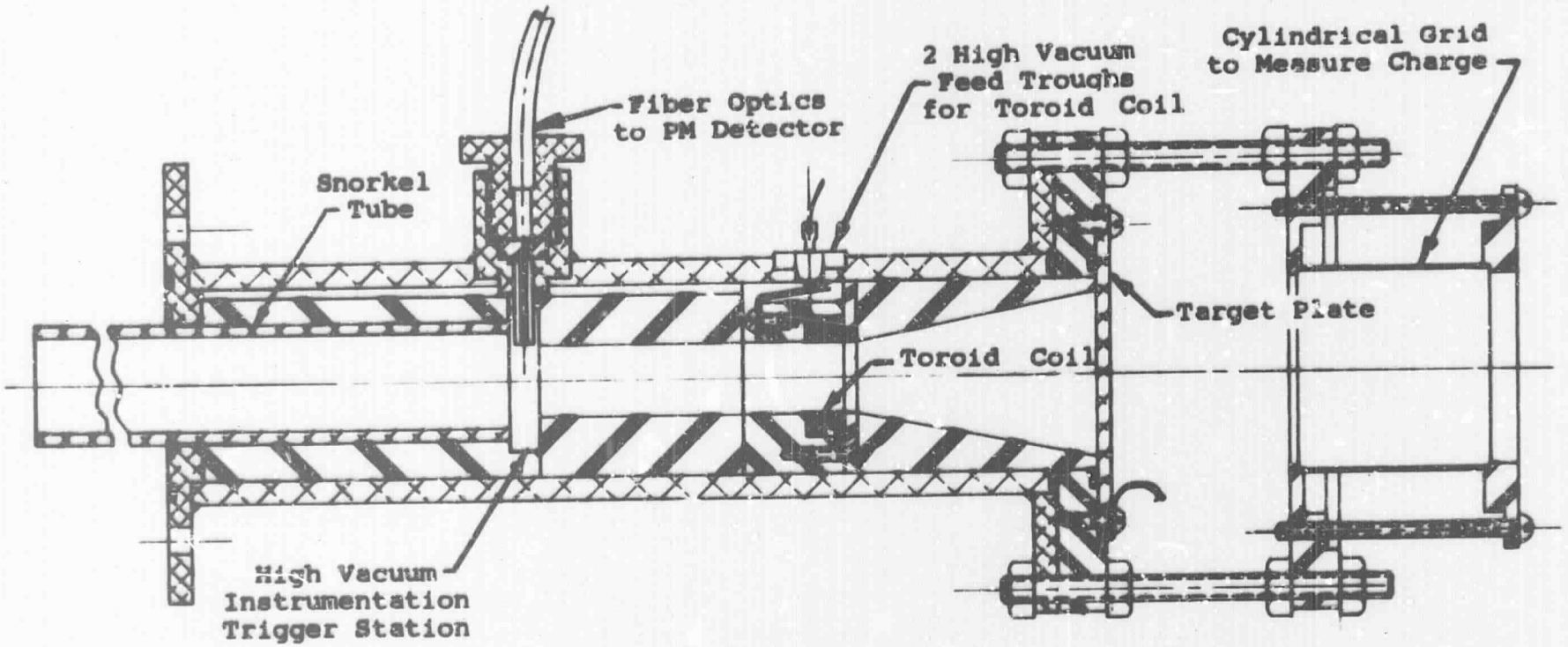

Figure 29 Target Plate Assembly

Projectile Design for Experiments. - The objective of this series of experiments was to establish a projectile configuration that would reliably impact a flat-disk type projectile normal to the target. Verification of attitude of the projectile was obtained from the image converters used to verify the velocity at stations C and D.

Since is was desired to obtain a high-velocity impact, the first test was made with a small projectile. A 0.050-in. diameter, 0.020-in. thick 1100 aluminum projectile was sabot-launched from a rifled 22-caliber launch tube. The image converter pictures showed the projectile to be unstable. A series of test shots from a .22-caliber rifled launch tube, with full bore projectiles 0.220 in. by 0.103 in. made from both 110 and 2024T4 aluminum were performed. These projectiles were deformed during launch and proved to be unstable. An attempt was made to reduce the damage to the projectile by employing a polyethylene disk behind the aluminum projectile. This proved to be futile also. Previous firings had been made with a full bore projectile from a smooth bore launch tube and they were also unstable, so they were not repeated in these tests.

A stable launch of a disk-type projectile was obtained on the eighth round in the tests. A 3/16-in. diameter, 3/32-in. thick 2024T4 projectile was sabot-launched from the rifled tube and was stable and provided a normal impact at the target. By increasing the projectile size and maintaining the same L/D ratio, the stability factor increases. In essence less spin is required to maintain stability for the larger projectile.

Using the same configuration with 1100 aluminum, the projectile was launched without deformation. Therefore, it was possible to conduct the experiment as NASA desired with flat impacting 1100 aluminum projectiles on 1100 aluminum targets.

In this series of tests a velocity instrumentation problem occurred. The normal sabot separation is between 2 to 3 in. on the diameter at the target end of the range. However, the added centrifugal force resulting from the rifled gun tube increased the separation pattern. This resulted in the sabot impacting baffle plates located at the velocity stations along the range. The impact flash from the impact was pre-triggering the PM's located at the velocity stations. Placing a sabot catcher plate and snorkel assembly just ahead of the B velocity station eliminated this problem. This required an additional alingment shot to be made before proceeding with Parts 2 and 3 of this phase.

Bubble Growth (Photographic and Radiographic). - The objective of this part of the experiment was to obtain sequential radiographs and photographs of the bubble growth resulting from flat impacts of the disk-type projectile on the thin aluminum targets. The projectiles used in this test were 0.188-in. diameter by 0.094-in. thick made from 1100 aluminum. The impact velocity was held constant within the limits of the launcher and projectile configuration between 20,000 and 21,000 fps. Aluminum 1100 targets were employed in these tests, with target thickness of 0.062 and 0.125 in. The impact resulted in holes for both target thicknesses with the flattened rolled-over lips on both sides of the target. The diameter of the hole remained constant for each target thickness, 1/2 in. diameter for the 0.062 in. and 5/8 in. diameter for the 0.125 in. target.

Three sets of sequential flash X-rays for the bubble growth for the 0.125-inch-thick target were obtained. Two were at normal impacts and the third was an unstable projectile impacting with considerable yaw. The effect of the yaw for round 15 is apparent in the radiographs of the bubble growth (Figure 30).

The impact on the 0.125-in. target shows an elongated two-stage-type bubble, as shown for rounds 13 and 14 in Figures 31 and 32. The leading edge of the bubble consist of very-fine low density particle sizes and cannot be resolved on the radiographs. The entire radiographs obtained in these three tests were of very low contrast. The photographic section intensified the records and improved the contrast, but still the complete bubble, in particular its leading edge, could not be defined.

The base portion of the bubble is clearly seen in the records, and also the base portion of the second stage of the bubble can be defined. Using the defined portion of the bubble as a guide, the remainder of the bubble is estimated by the dotted lines shown in Figures 31 and 32. Figure 33 shows the bubble growth history reduced from these records where the height of the bubble is based on the estimated shape It should be observed that the estimated height closely matches the data obtained from the 0.062-in. target (Figure 34).

Two rounds with flash X-ray coverage were fired against 0.062-in. targets. For these tests, the cassettes were moved in closer to the target. The bubble can clearly be seen in the early stages but, as it expands, and the particle density decreases it became difficult to resolve. It is faintly visible at 8 μsec and it appears to be reaching

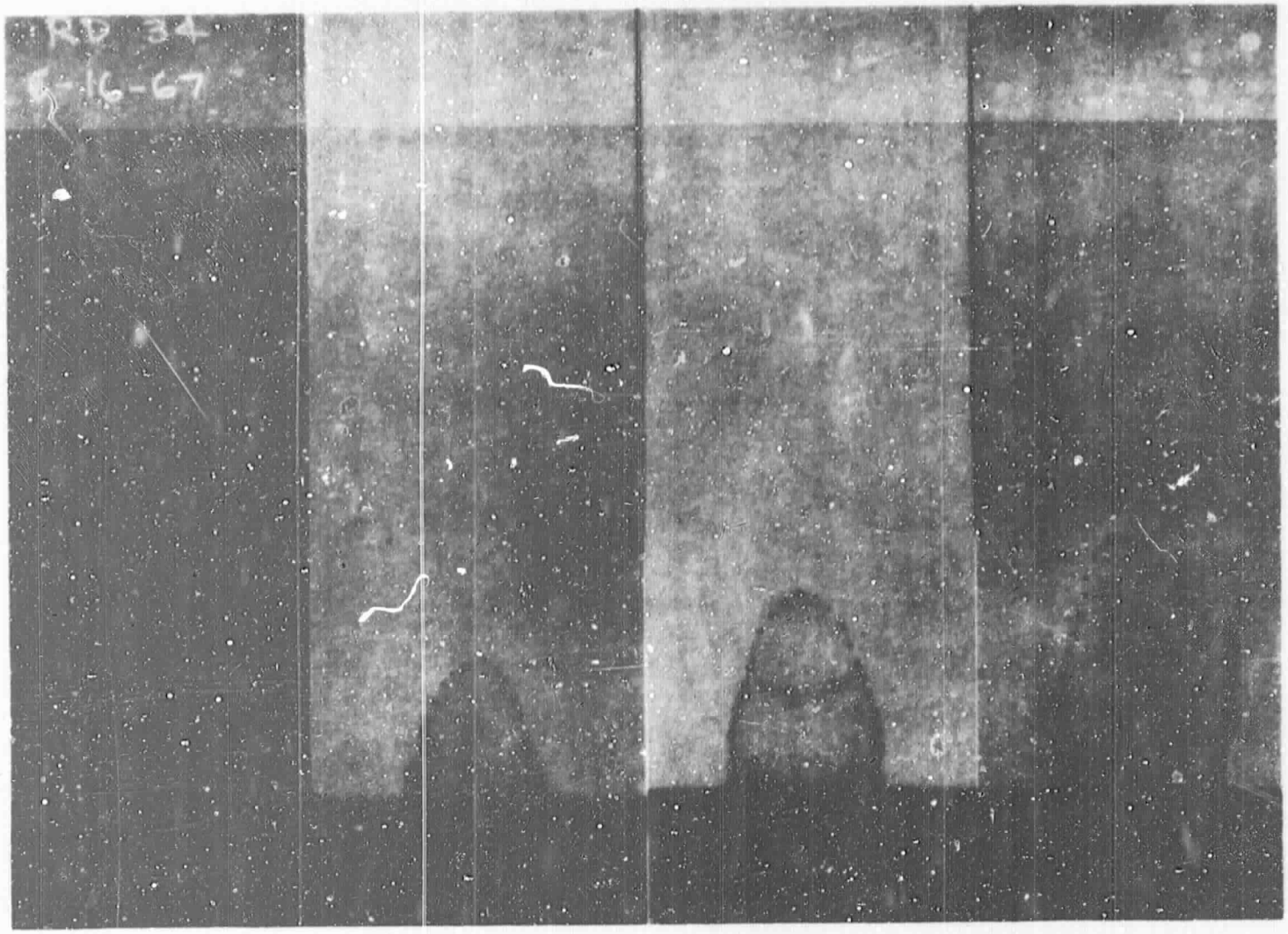

Figure 30 Radiograph, Round 15

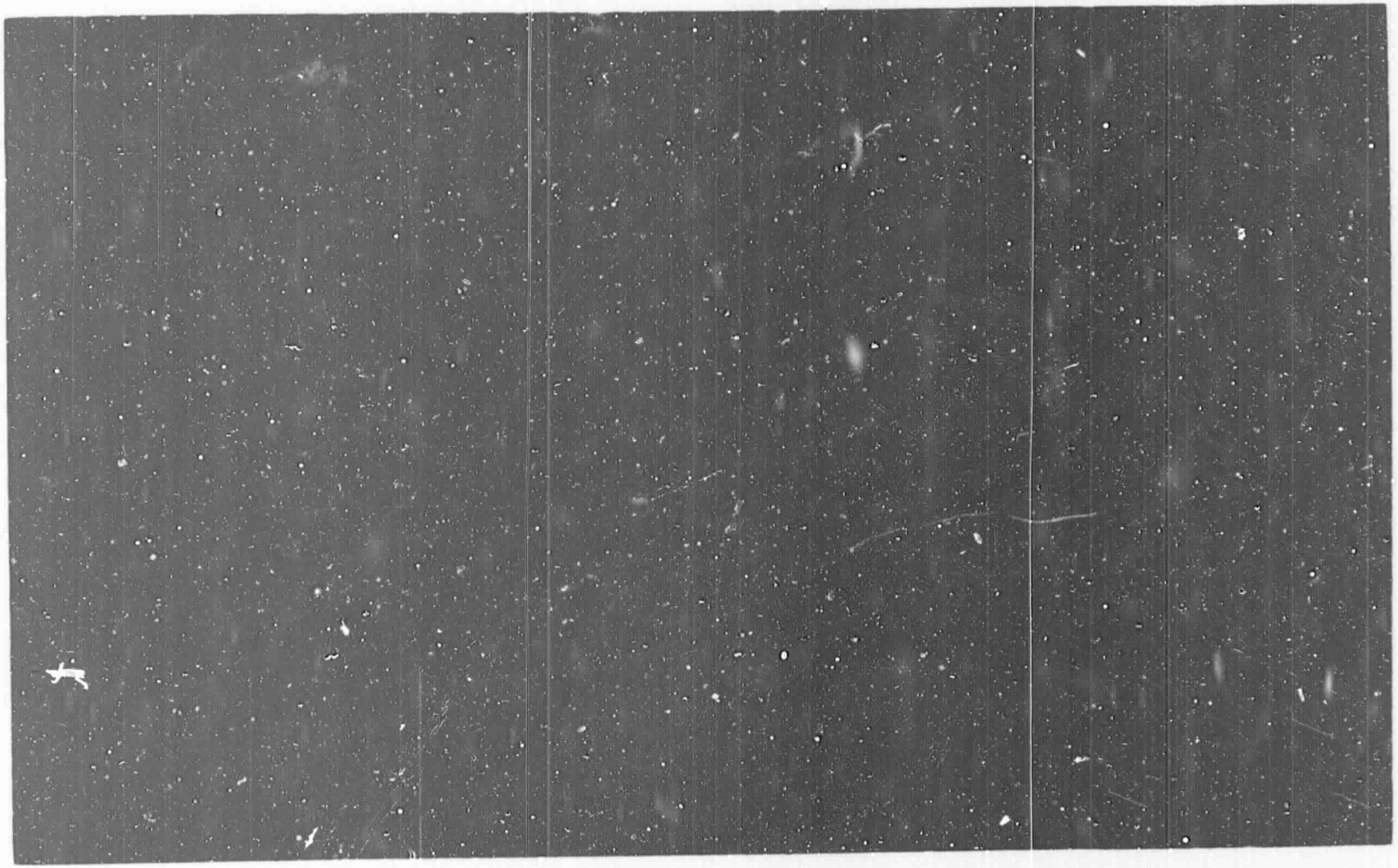

Figure 31 Radiograph, Round 13

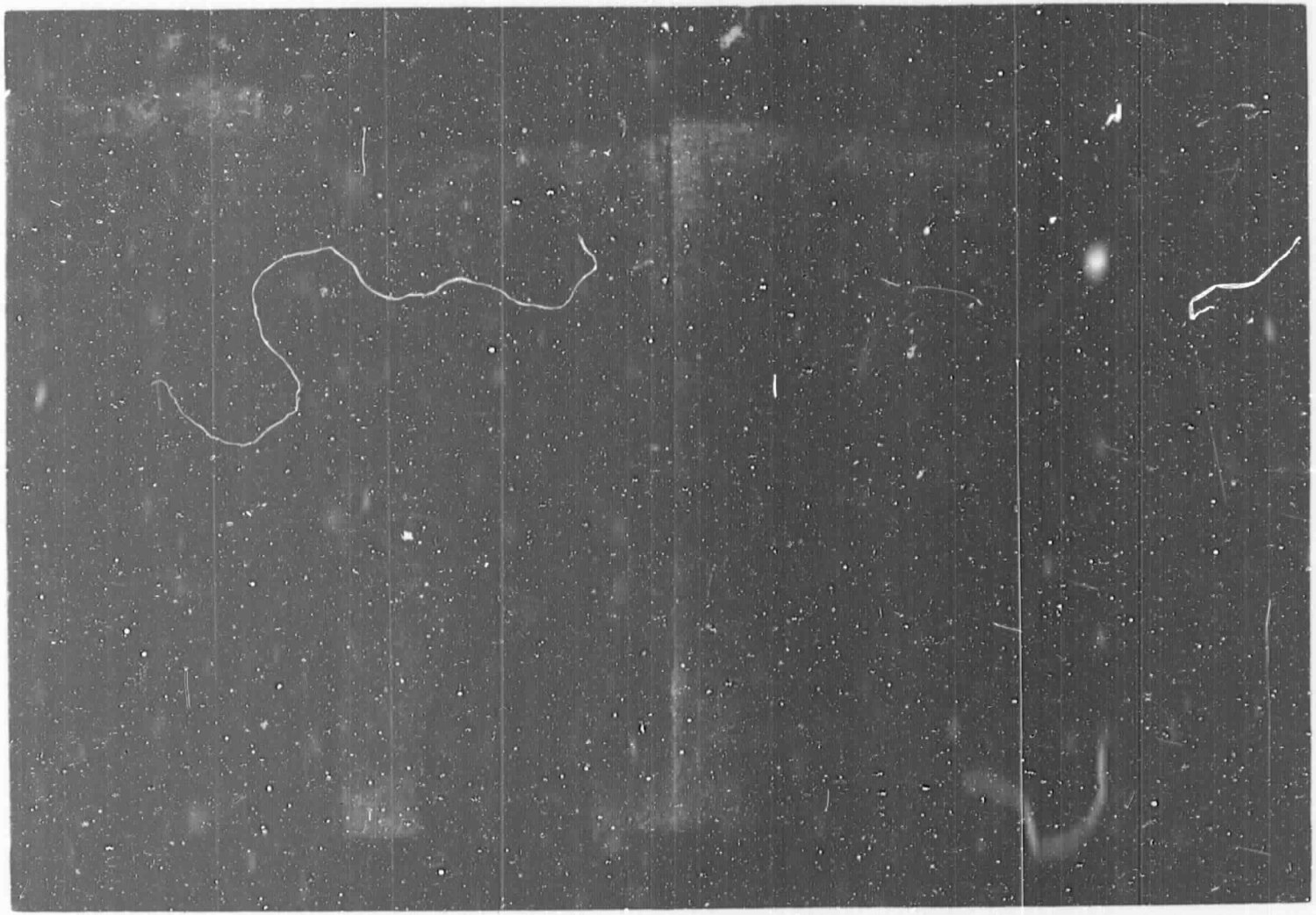

Figure 32 Radiograph, Round 14

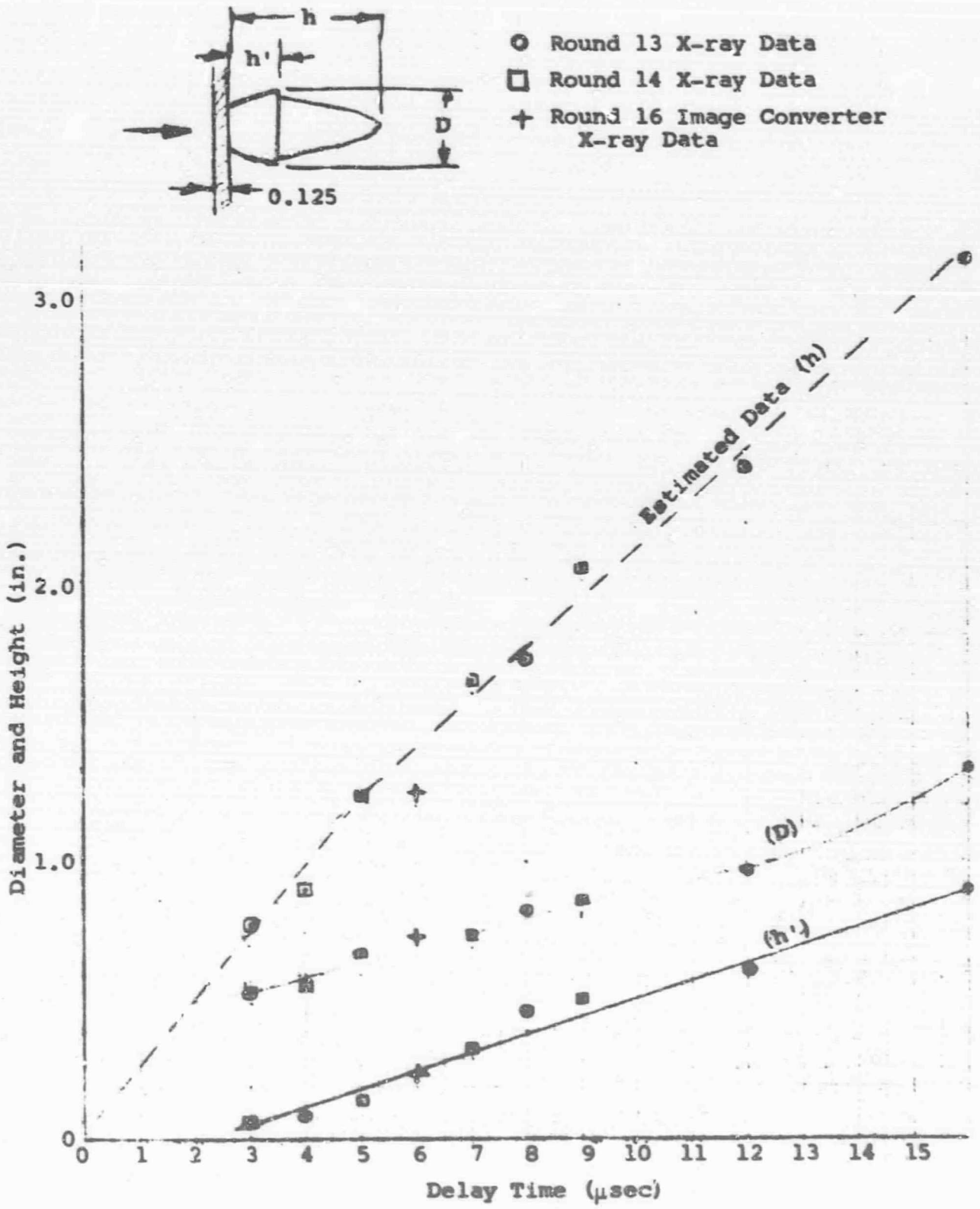

Figure 33 Bubble Growth for 0.188-in.-Diameter, 0.094-in.-Thick 1100 Al Projectile on 0.125-in.-Thick 1100 Al; Target Velocity 20,000 fps

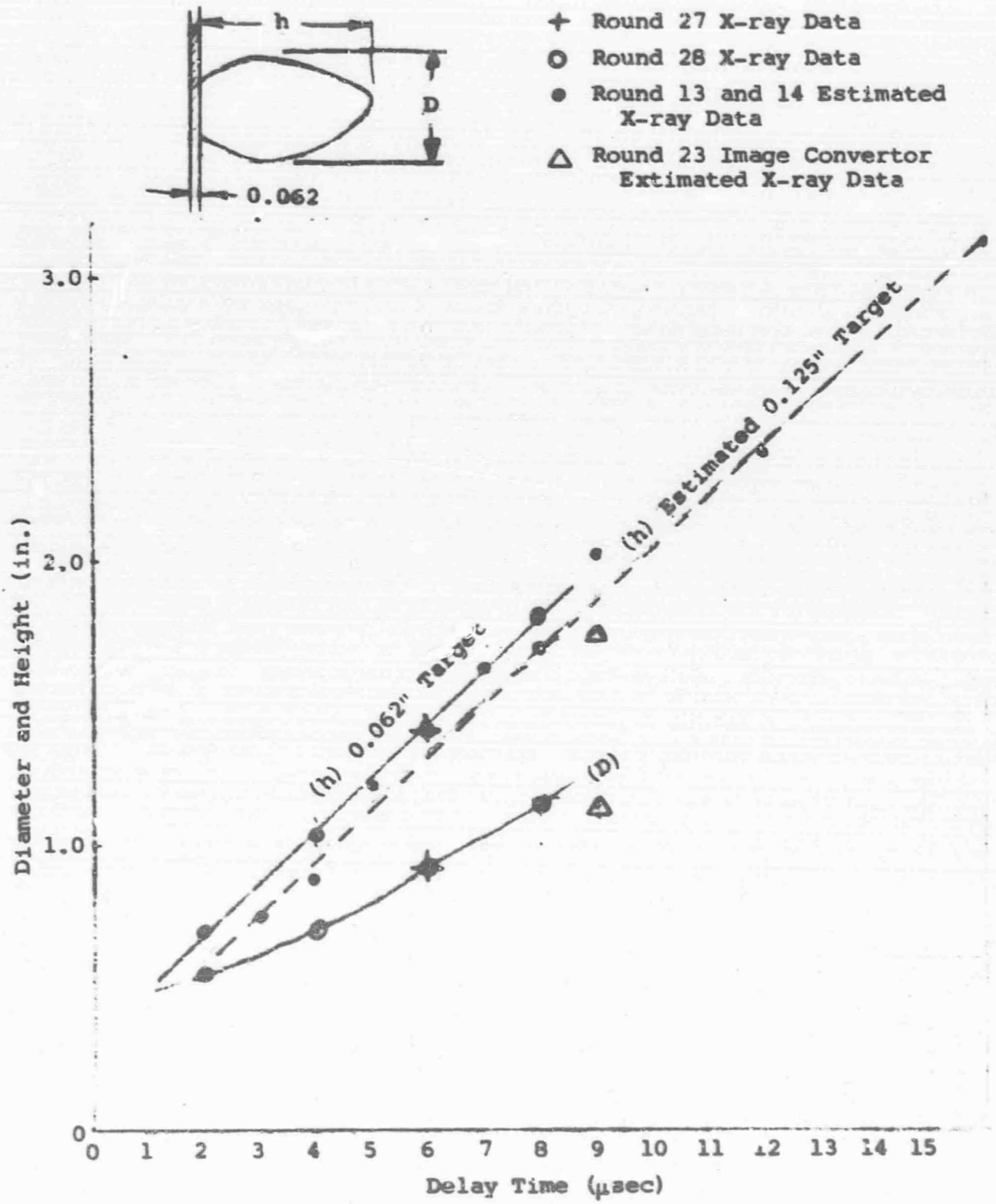

Figure 34 Bubble Growth for 0.188-in.-Diameter, 0.094-in.-Thick 1100 Al Projectile on 0.062-in.-Thick 1100 Al; Target Velocity 20,500 fps

a resolution limit beyond this point. Rounds 27 and 28 were fired at the 0.062-in.-thick target, with X-ray coverage. On Round 27, irregular triggering of the X-ray unit occurred and only one good radiograph (at 6 μsec delay) resulted. Readjustment of the sensitivity on the X-ray delay units corrected the irregular triggering and on round 28 four good radiographs of the bubble were obtained. The sequential radiographs for both rounds are shown in Figure 35. The resulting bubble on the 0.062-in.-thick target has the more normal symmetrical bubble associated with hypervelocity impacts, and does not indicate any sign of the two-stage bubble seen on the 0.125-in.-thick target. The data from the sequential X-rays are shown on Figure 34 along with estimated height of bubble obtained from the 0.125-in. target. Based on the comparison with the estimated data, the forward expansion of the bubble appears to be equal for both target thickness, however, the radial expansion for the 0.062-in.-thick target is higher.

The single-frame image-converter camera used to verify projectile velocity was incorporated to obtain comparative bubble growth data. To expedite the firings, the initial experiments were conducted with the target located at the second velocity station. A series of firings was necessary to obtain a sequential bubble-growth history for this setup. At this time, the number of experiments to be conducted was limited, and data on ionization and flash measurements were also desired. Therefore, a compromise had to be made and the number of experiments in this area was minimized.

The image converter camera is normally triggered by the PM located at the station. It was set up for these experiments to be triggered on the impact flash from the front face of the target. Data obtained were insufficient to determine the accuracy of this trigger source. In the first test, round 16, the event was backlighted and a good record of the bubble was obtained. This was with a 0.18-in.-diameter, 0.094-in.-thick disk-type projectile on a 0.125-in.-thick target. A delay time of 6 μsec showed a bubble with the two-stage shape that was observed with the flash X-rays, as shown in Figure 36. The size of the bubble from the image converter photograph and the X-ray data closely agrees, and is shown on the growth curves in Figure 34. This indicates a satisfactory triggering method.

In the next test, round 17, the light source was eliminated in an attempt to photograph the event by the illumination produced by the impact flash. A maximum exposure time was set for this experiment. With the same delay (6 μsec) as used in the previous test, the camera failed to record anything on the screen. The record indicated that the camera functioned at the proper time. Since

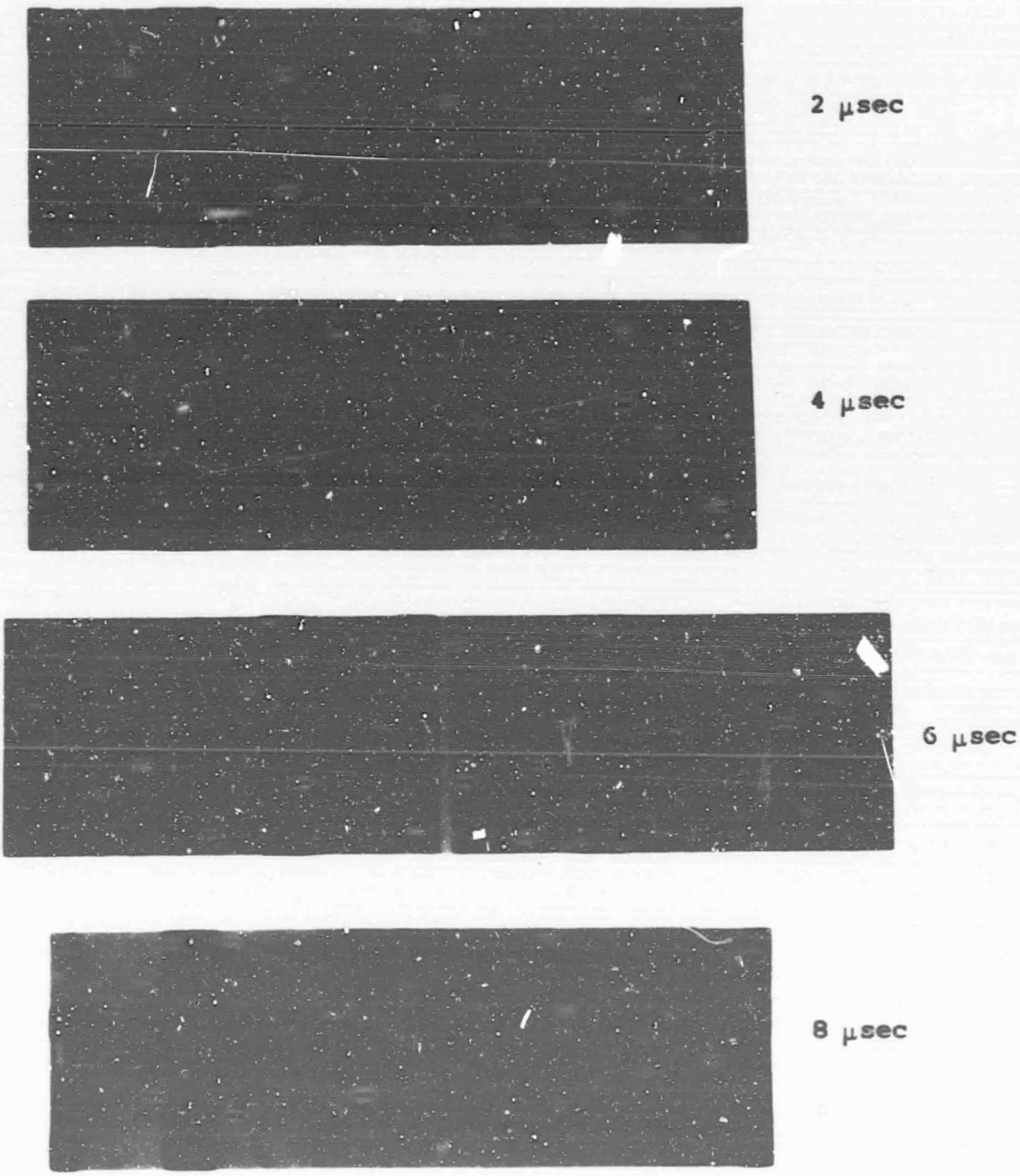

Figure 35 Radiographs, Rounds 27 and 28. 0.188-in.-Diameter, 0.094-in.-Thick Target against 0.062-in.-Thick Target

the event was not recorded, it was assumed that insufficient light was given by the flash to register on the image converter unit. However, when checking out the unit after this test, it was found that the voltage supply for the image converter unit was defective and may have been so on the test. Thus, it is possible that the failure to obtain a record may be the result of the image converter unit malfunction.

In this firing sequence, a hardware failure in the high-pressure section of the launcher occurred. This resulted in damage to the entrance of the rifled launch tube, and required rework. In realigning the launcher tube, the flight path was lowered. As a result of the low flight path only the upper portion of the bubble was obtained for round 25, which is shown in Figure 36. The delay time for this test against the 0.062-in.-thick target was again set at 6 μsec. Although the actual size cannot be determined from this photograph, it is apparent that the bubble is larger than that obtained for round 16 with the same time delay. Round 26 was a repeat of this test with the muzzle of the launch tube shimmed up to raise the flight path of the projectile. The catcher plate assembly was also shimmed to compensate for the higher flight path. However, the projectile nicked the entrance of the snorkel tube and the projectile broke up. Small pieces of the projectile were shown impacting on the target. No additional image converter tests were made with the camera located at the second image converter station.

The image converter was relocated at the viewing port of the vacuum chamber. Two additional attempts at self-illumination explosures were made. Round 29 was deflected and did not hit the target. On round 30, the records indicate a good trigger and no malfunction of the image converter unit, however, no photo of the bubble was obtained.

NASA furnished a TRW image-converter framing camera (three frames) for additional monitoring of bubble growth. The camera was brought in, set up, and operated by Mr. R. Naumann. The tests with this unit were primarily to check out the equipment evaluate its use for future tests in this application. Only three experiments were made with the TRW camera located at the viewing port in the high-vacuum chamber. All tests were with a 0.18-in.-diameter, 0.094-in.-thick projectile and a 0.062-in.-thick target.

Round 16 0.125-in. Target 6-μsec Delay

Round 25 0.062-in. Target 6-μsec Delay

Figure 36 Back-Lighted Image Converter Photographs of Bubbles Made with 0.188-in.-Diameter, 0.094-in.-Thick 1100 Al Projectile on 1100 Al Targets

On the first test (round 22) with this unit, the camera was triggered by a built-in light detector using fiber optics. The picture from the camera shows considerable light in the test chamber for all three frames. It appears that the light detector failed to trigger on the initial flash from the projectile impact but triggered on the secondary flash when the bubble particles impacted on the nickel charge-collection grid located 2 in. behind the target, thus the bubble cannot be defined in the Polaroid record, Figure 37.

An external light detector was employed in the following test with the TRW camera, using fiber optics to view the back face of the target. A good trigger pulse was recorded for round 23 and only one picture bubble was obtained, on the last frame of the record (Figure 37). The actual time between impact and explosure cannot be determined from the records. From the data that are available it is estimated that impact on the target occurs at 24 μsec after passing the trigger detector located 6 in. ahead of the target. The records show that the camera was triggered at 27, 29 and 34 μsec after passing the trigger detector station. Then the exposure times after impact would be 3, 4, and 9 μsec. The measured bubble height is 1-3/4 in. and the maximum diameter is 1-1/8 in. These points are plotted on Figure 34 and correspond relatively close to the X-ray data for the same impact conditions. There does not appear to be any logical reason why the bubble does not appear on the two missing frames at this time.

In the last test with the TRW camera, a make-switch was used to trigger the camera. The switch was mounted on the impact side of the target and employed the same circuit used with the X-ray instrumentation which had worked reliably. The records showed that the make-switch triggered 23 μsec after the projectile passed the trigger station ahead of the target, indicating a good trigger. The TRW camera pre-triggered, however, and no picture of the bubble was obtained.

Hypervelocity Impact Flash Observations. - The optical observations of the impact flash were viewed through 1/4-in.-thick fused silica windows (Corning "Optical Grade" No. 7940 fused silica). These windows transmit throughout the visible and ultraviolet wavelength region with a cutoff at about 2000 A. Three windows were mounted in ports around the experimental chamber at a radial distance of 9 1/2 inches from the projectile axis.

The optical measurements utilized two types of instruments. One of these was a multiplier phototube (RCA type 1P28) that viewed the impact area behind the target through a 1-in.-diameter aperature placed 4-1/4 in. in front of the

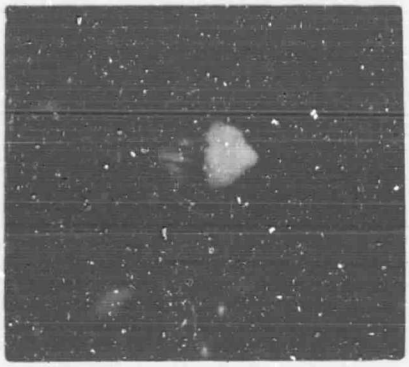

Round 22 Results with Late Trigger

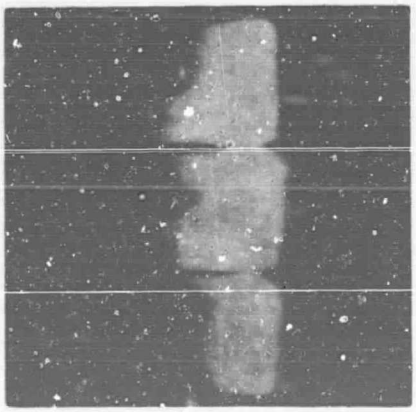

Round 23 Estimated Time after Impact
9 μsec; No Record for First and Second
Frames

Figure 37 TRW Framing Camera Results

photocathode. A protective light shutter was in front of the aperature. The shutter was opened immediately prior to the shot. The field of view (Figure 38) of this device at the target axis was about 1-1/2 in. in diameter. The multiplier phototube has an X-5 spectral response (sensitive between about 2400 to 6200 A), that defines its measurements as "broad band luminosity."

The other instrument measures four separate spectral channels simultaneously. A medium quartz prism spectrograph Hilger Model E498 with a wavelength range of 2000 to 10,000 A was used as the dispersive element and four multiplier phototube were placed at the camera plane of the spectrograph. Slits for each phototube were set at the desired wavelength and the spectral bandpass was obtained by adjusting the slit widths. The spectrograph was positioned such that it viewed an area of ~1-in. by 1-1/2 in. about the target axis.

The outputs of all multiplier phototubes used were coupled directly from their anodes to cathode followers and then to fast, high-sensitivity oscilloscope preamplifiers. The rise time of the system was of the order of 10^{-8} second, which was sufficient for time-resolved studies of the impact flash. All data were recorded by oscilloscope cameras. Neither of the optical instruments was calibrated for absolute luminosity. The major effort in the preliminary measurements has been to establish the observable signal levels and operating parameters.

The broad-band luminosity instrument was used on rounds 20, 21, 22, 23, 24, 29 and 30 in the Phase III tests. A summary of the results of these rounds is given in Table XVII. Data were obtained for rounds 24 and 30 and are presented in Figure 39. The zero of the time base in the figure is at 25 μsec after the trigger pulse from the light pipe PM trigger. The intensity ordinate is in arbitrary units for each curve. One major difference in the experimental setup for these two rounds is that the charge collection instrumentation was not in the target chamber on round 24.

The four-channel spectral detector was used only on round 30. In this experiment the wavelength bandpass of each channel was set at 100 A and the midpoints of the four channels were set at 3090, 3950, 4500, and 5900 A. These bands were chosen to detect aluminum and sodium line emissions and a point of the continuum radiation specifically. One of

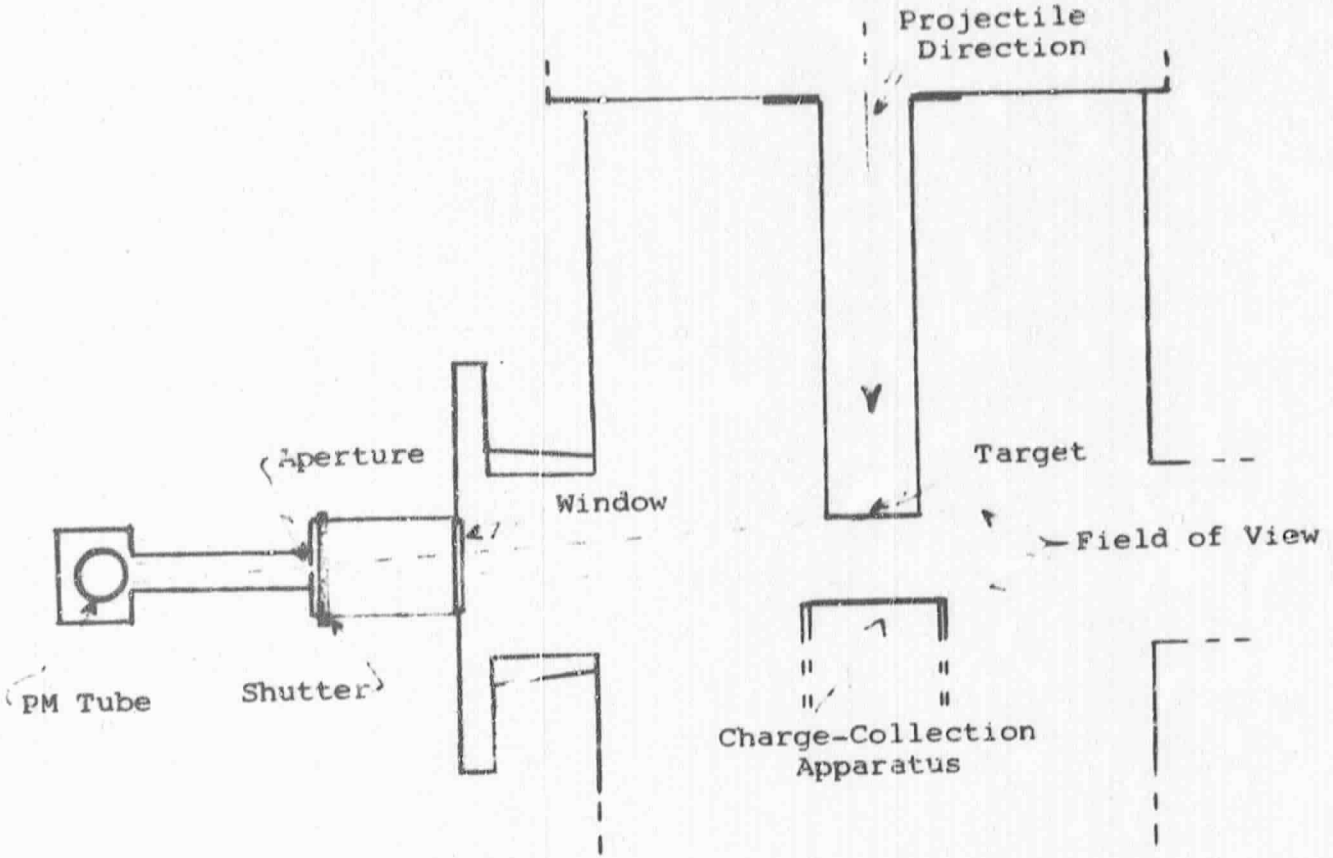

Figure 38 Experimental Geometry for Broad Band Luminosity Measurements

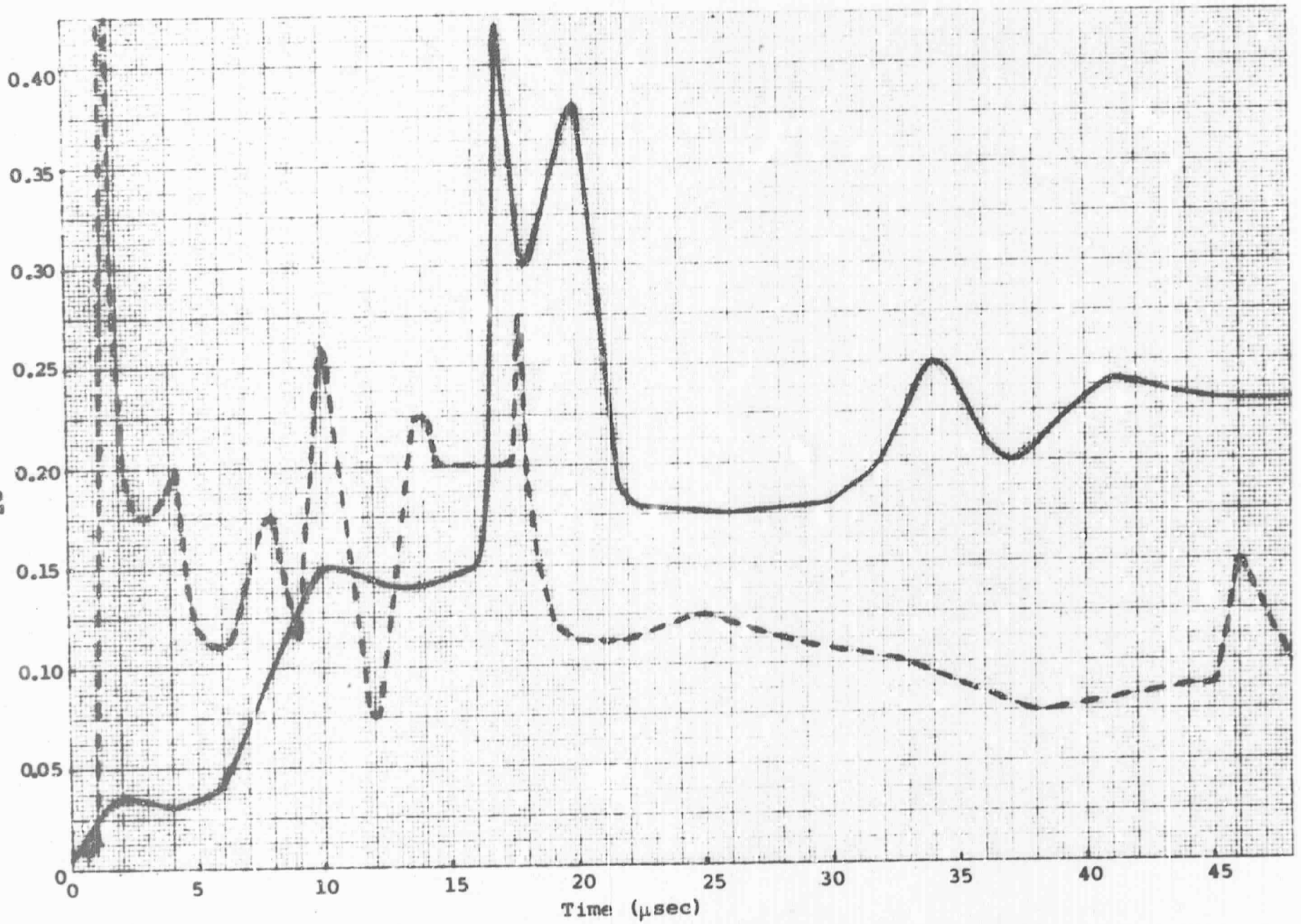

Figure 39 Broad Band Luminosity Results, Rounds 24 and 30

TABLE XVII

SUMMARY OF BROAD BAND LUMINOSITY RESULTS

Round	Results
20	Sensitivity set too high, signals off scale.
21	Oscilloscope triggered late, no data.
22	Protective shutter failed to open, no data.
23	Data obtained, usable for establishing signal levels.
24	Good data obtained.
29	Projectile did not hit target, no data.
30	Good data obtained.

the bans also includes several strong lines of the nickel emission spectrum. The characteristics of each channel are

Channel	Wavelength Band	Emission Detectable
1	3040 to 3140 A	Aluminum, Nickel
2	3900 to 4000 A	Aluminum
3	4450 to 4550 A	Continuum
4	5850 to 5950 A	Sodium, and/or Continuum

The results from this experiment are shown in Figure 40. The zero on the time base is again set at 25 μsec after the trigger pulse. Each curve is in arbitrary intensity units at this time; however, the experimental settings can be reproduced for future calibration. Some data were not recorded because signal levels were higher than expected.

There are gross differences in the broad band luminosity data between rounds 24 and 30, especially in the time region up to ~10 μsec in which it is expected that the primary impact flash event would have occurred. We have no definitive explanation for this difference in experimental set up between these two rounds; i.e., the charge collection instrumentation was not present in the target chamber during round 24. It is possible that the detector may have been out-of-line for round 30 and had its field of view obstructed by the charge collection apparatus, or that the charge collection apparatus does have some major effect upon the luminosity in the region between the impact target and the collection rig. Further experiments, both with and without the charge collection apparatus in place, will have to be performed to resolve these differences.

Regardless of the differences in the luminosity as a function of time curves between these two experiments, it is obvious that there is an appreciable light signal for long times after impact and that there are various maxima and minima in the luminosity-time history (none of the data has been taken for a time base long enough to determine the decay or extinction of the luminosity).

All channels of the spectral detector (Figure 40) exhibited maxima between zero and 5 μsec. However, the peak luminosity in each case was not reached until a time beyond 10 μsec. Since the data are incomplete, because of the higher-than-expected signal levels, it is not possible to add the individual signals from Figure 40 to see if the sum

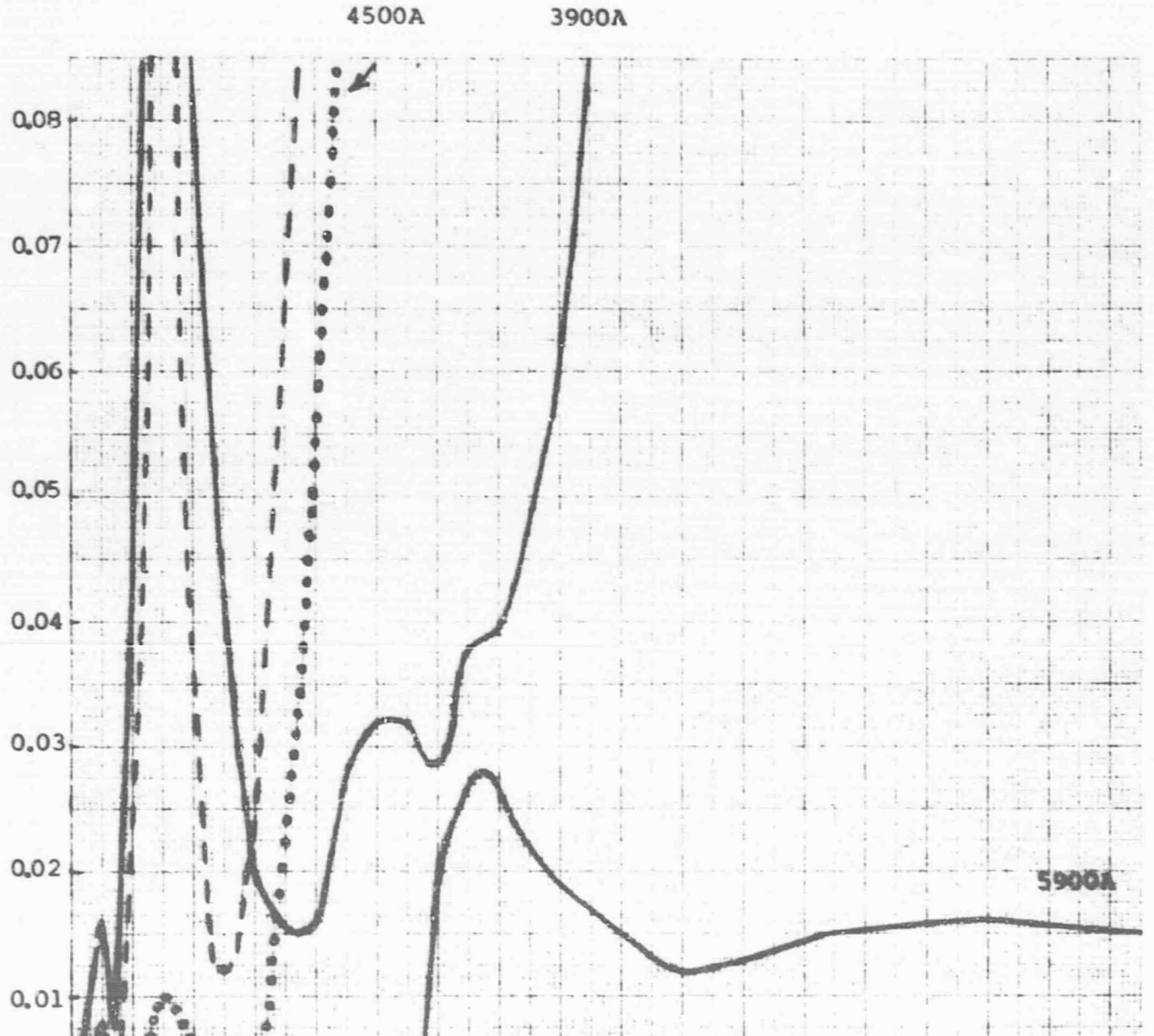

Figure 40 Spectral Data, Round 30

would agree with that obtained from the broad band luminosity measurement. It is noted that the signal for the 3090-A channel does not seem to follow the same time behavior as the 3950-A channel. If these two channels were seeing only the aluminum excitation radiation, one would expect them to have similar curves. The 3090-A channel will also detect nickel radiation from the charge collector cylinder. This should enhance the signal at later times, whereas it is seen that the relative intensity of the signal decreases at the longer times with respect to the 3950-A channel. On the other hand, if the 3950-A channel band pass settings were slightly off so as to include some of the CN (0,0) band starting at 3883 A, which is often a strong impurity, this would distort the meaning of the relative intensities. In future experiments, this channel will be narrowed in bandpass to exclude such a possibility.

In these experiments there are three conceivable sources of luminous emission in the target chamber: (1) the primary impact flash due to the projectile impinging on the target: (2) secondary impact flashes due to target ejecta impinging on the charge collection apparatus and/or the chamber walls; and (3) luminous gases passing through the impact hole in the target from the front side, i.e., from the higher pressure volume of the range. One would expect the time sequence of these three sources to be in the order of their enumeration. Impact flashes observed on the incident side of thick targets[1,2] are rather simple pulse-like flashes with a total time duration of ~10 μsec. While the experimental conditions reported herein are appreciably different from those of the references (observations are made on the back side of thin targets), one would not expect the total time duration of primary impact flash to be greatly different. It is suggested then that the luminosity observed at the longer times (20 to 40 or more μsec) is due to sources other than the primary impact.

It is obvious that further experiments are needed to correlate time and spectral data for the analysis of the observed luminosity. With such measurements, the color temperature and spectral line excitation temperature may be determined as a function of time.

1. R.W. MacCormack, "Investigation of Impact Flash at Low Ambient Pressures," VI Hypervelocity Impact Symposium, Vol. II, Part 2 (1963).
2. F.D. Rosen and C.N. Scully, "Impact Flash Investigation to 15.4 km/sec," VII Hypervelocity Impact Symposium, Vol. VI (1965).

The preliminary observations of the luminosity at the back side of thin aluminum targets impacted with hypervelocity aluminum projectiles show a very complicated luminosity history extending for times greater than 40 μsec. This observation was true both for broad spectral band detection and for a series of four concurrent narrow band (100A) detectors. It is suggested that the observed luminosity is due to more than the primary impact flash alone.

Further experiments are recommended utilizing both the broad band spectral detector and the four-channel spectrum analyzer to determine the spectral time history of the observed emission. It is also recommended that image data be obtained on the luminous source at various times. These experiments should be performed both with and without the charge collection apparatus in place in the experimental chamber.

Charge Collection. - Previous qualitative observations have indicated that electrically charged particles are emitted from the site of a hypervelocity impact. The ions and electrons thus produced can be collected by means of an electrical grid system. The quantity of charge emitted depends upon the initial particle velocity and mass, and upon the characteristics of the particle and target materials. This report describes measurements conducted using a 22,000 fps aluminum projectile impacting upon a thin aluminum target. An initial set of measurements of the charge accumulated on the projectile prior to impact and of the charge released as a result of the impact was made.

The two most obvious methods for detecting the charge on the projectile prior to impact are the capacitive and magnetic techniques. In the former, an induced voltage on, say, a small cylinder through which the charge projectile passes would be used to determine the charge magnitude. A likely difficulty here is that the capacitance changes because of the presence of the metallic projectile as it is passing through the cylinder, so that a unique determination of charge is not easily obtained. Because of this shortcoming, it was decided to proceed initially using the magnetic technique. In this case, use is made of the fact that a projectile carrying a charge Q and moving with a velocity v results in a current I. Thus, if a charged projectile with a known velocity passes through a coil, a current is induced in the winding which is proportional to the projectile charge.

For our application, a toroid geometry was used with 250 turns of #32 wire wound on a 1/4-in.-OD, 3/4-in.-ID core having a width of 0.38 in. A charge-sensitive amplifier was used to detect the charging of a capacitor by means of the current induced in the coil windings (the amplifier sensitivity, as given by the manufacturer, is 0.21 μvolt per electron). In addition to this instrument, a pulse-shaping amplifier, which provided additional gain for the overall system, was used. Calibration was performed using the scheme illustrated in Figure 41. The pulse generator, used to simulate the current pulse of the moving projectile, provided a 1-μsec-wide signal to the wire running through the detector coil. The resistor R_1 was used to vary the current within the desired range; this current was measured by monitoring the voltage drop across R_2. The emf generated in the detection coil due to the changing magnetic field associated with the current pulse was simultaneously measured with the charge-sensitive amplifier by determining the charge on capacitor C_1 (Figure 41). Table XVIII shows the output voltages obtained for the range of currents chosen. These currents correspond to projectile charges of from 1.25×10^{-15} to 6×10^{-13} coulomb based upon estimated hypervelocity range velocities and the coil dimensions. That is, if x is the coil width, v the projectile velocity, and Q the projectile charge, the current i is given by

$$i = \frac{Q}{t} = \frac{Q}{(x/v)}$$

This expression is not precisely accurate since x is really a mean magnetic field interaction distance and not exactly the physical coil dimension.

Figure 42 illustrates the scheme for calibrating the system used in determining the charge released by the impact. The Ortec pulser and capacitor simulate the charge production of the event as seen by a collector grid in the region of the impact. The pulser has a precision voltage divider and vernier control for accurate amplifier calibration. By adjusting the pulser output, the magnitude of the capacitor charge was made to cover the range 5×10^{-14} to 1.35×10^{-12} coulomb. This range was selected on the basis of previous related work as that which would likely include the charge magnitude produced by our thin-target impacts. Figure 43 gives the amplifier output as a function of charge collected on the simulated grid.

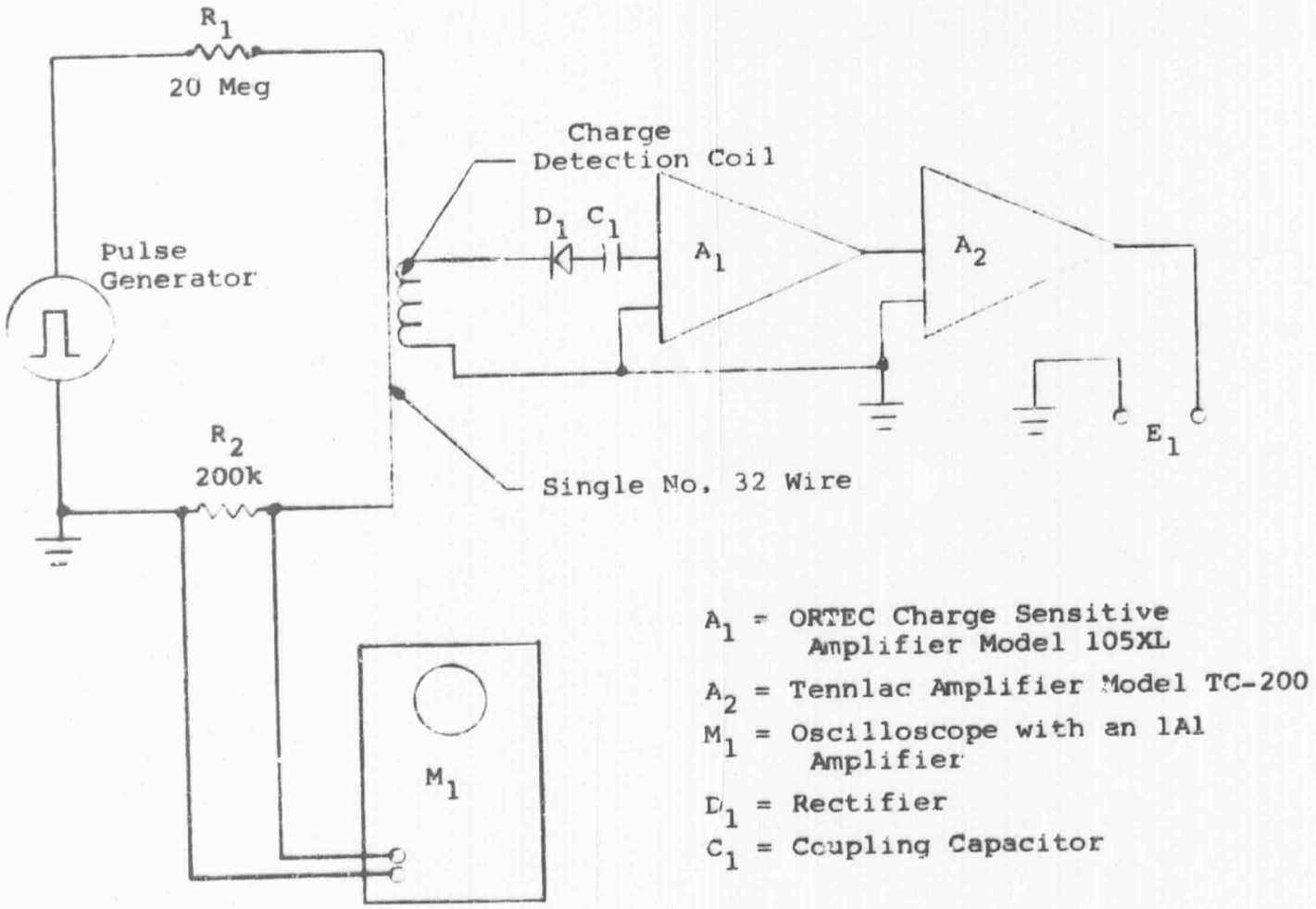

Figure 41 Projectile Charge Detector Coil Calibration Arrangement

TABLE XVIII

PROJECTILE CHARGE COIL CALIBRATION DATA

Voltage Across R_2 (mvolts)	Current in R_2 (Amp)	Output of TC. 200 Amplifier (Volts)	Effective Projectile Charge (Coulomb)
0.25	1.25×10^{-9}	0.02	1.25×10^{-15}
0.50	2.5×10^{-9}	0.04	2.5×10^{-15}
1	0.5×10^{-8}	0.06	5.0×10^{-15}
2	1.0×10^{-8}	0.15	1.0×10^{-14}
4	2.0×10^{-8}	0.30	2.0×10^{-14}
10	5.0×10^{-8}	0.80	6×10^{-14}
20	1.0×10^{-7}	1.5	1×10^{-13}
30	1.5×10^{-7}	2.5	1.5×10^{-13}
40	2.0×10^{-7}	3.5	2.0×10^{-13}
50	2.5×10^{-7}	4.2	2.5×10^{-13}
60	3.0×10^{-7}	5.0	3.0×10^{-13}
100	5.0×10^{-7}	7.5	5×10^{-13}
140	7.0×10^{-7}	10.0	6×10^{-13}

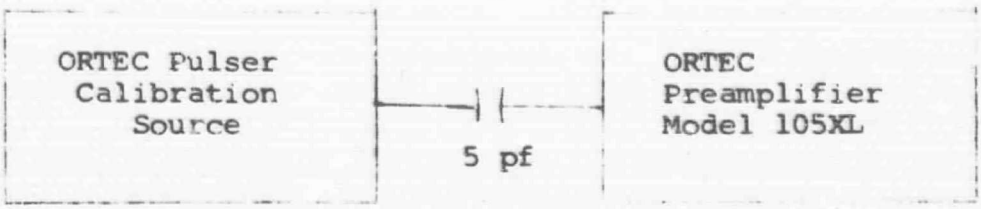

Model 105XL Sensitivity (0.21 μv/electron)

Figure 42 Impact Charge Collection Calibration Scheme

A vacuum chamber designed for pressures down to 10^{-6} torr was fabricated for the charge collection and radiation measurements. The chamber was attached to the end of the hypervelocity range with the aluminum target at the end of a re-entrant tube (Figure 44). This assembly maintained the pressure differential between the range and the target chamber. The target chamber pressure began to rise immediately upon impact and destruction of the target, but the transit time of the electrons (from target to collector) is much shorter than the characteristic pressure rise time due to expansion of the gas from the range into the chamber.

Also shown in Figure 44 is the fiber optic cable which permits the photomultiplier detection of the projectile. The signal thus obtained is routed through a time-delay network and used to sequentially trigger the two oscilloscopes that record the projectile charge and impact charge signals. Figure 45 shows the components of the recording system and their relation to the sensing elements in the vacuum chamber.

Five impacts were observed with partial or complete instrumentation. It should be noted that at the outset of these experiments there existed practically no basis for deciding upon instrumental gain and sensitivity settings.

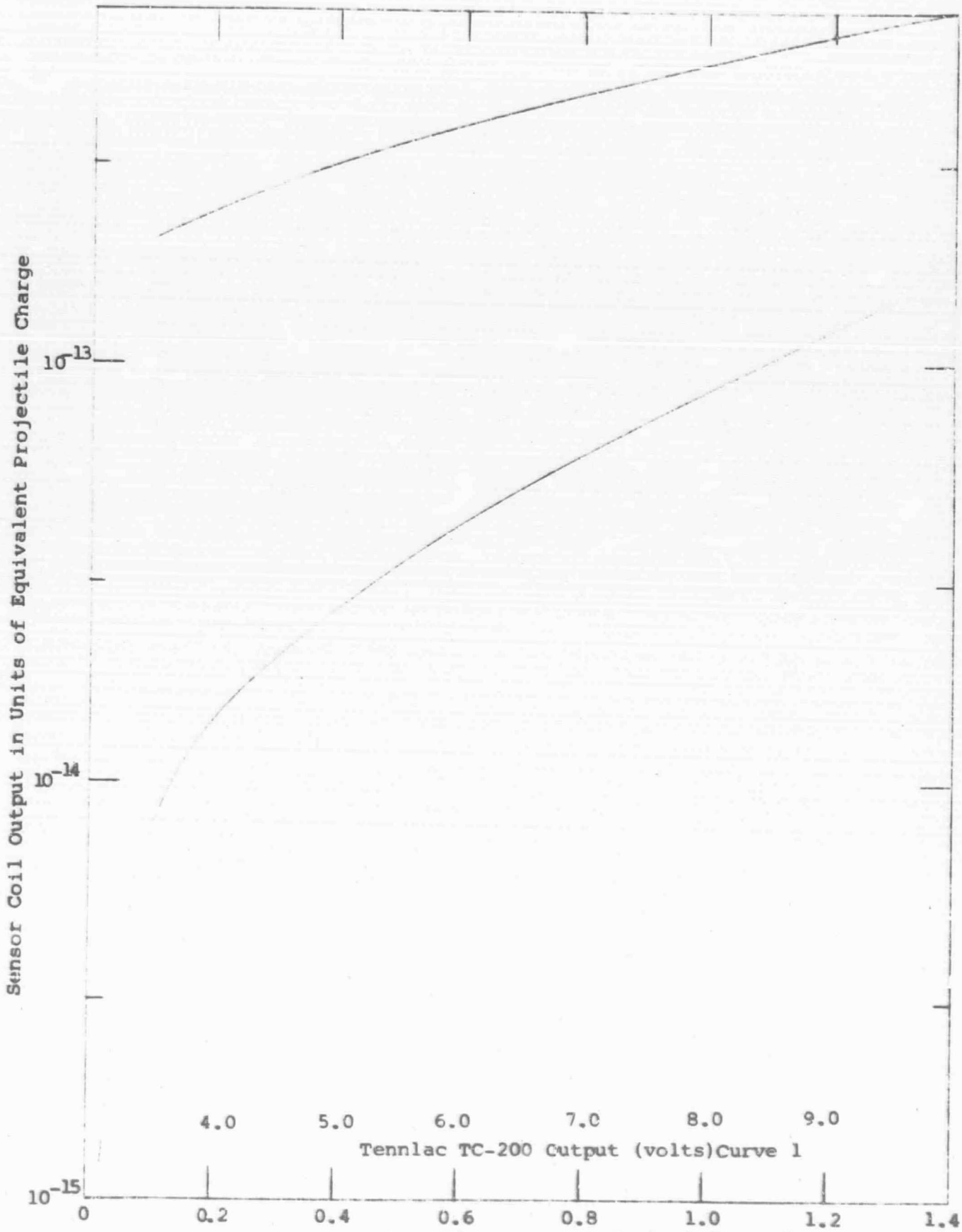

Figure 43 Sensor Coil Response

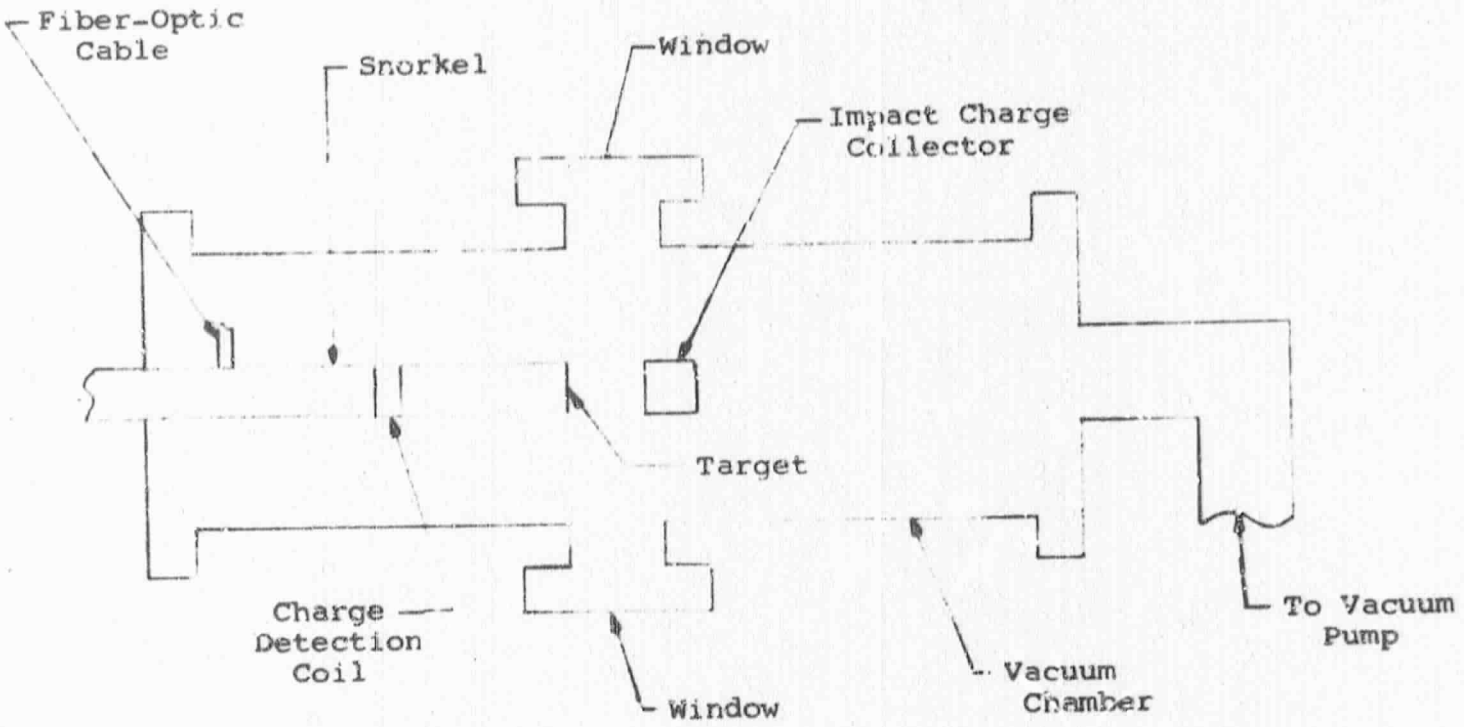

Figure 44 Impact Chamber

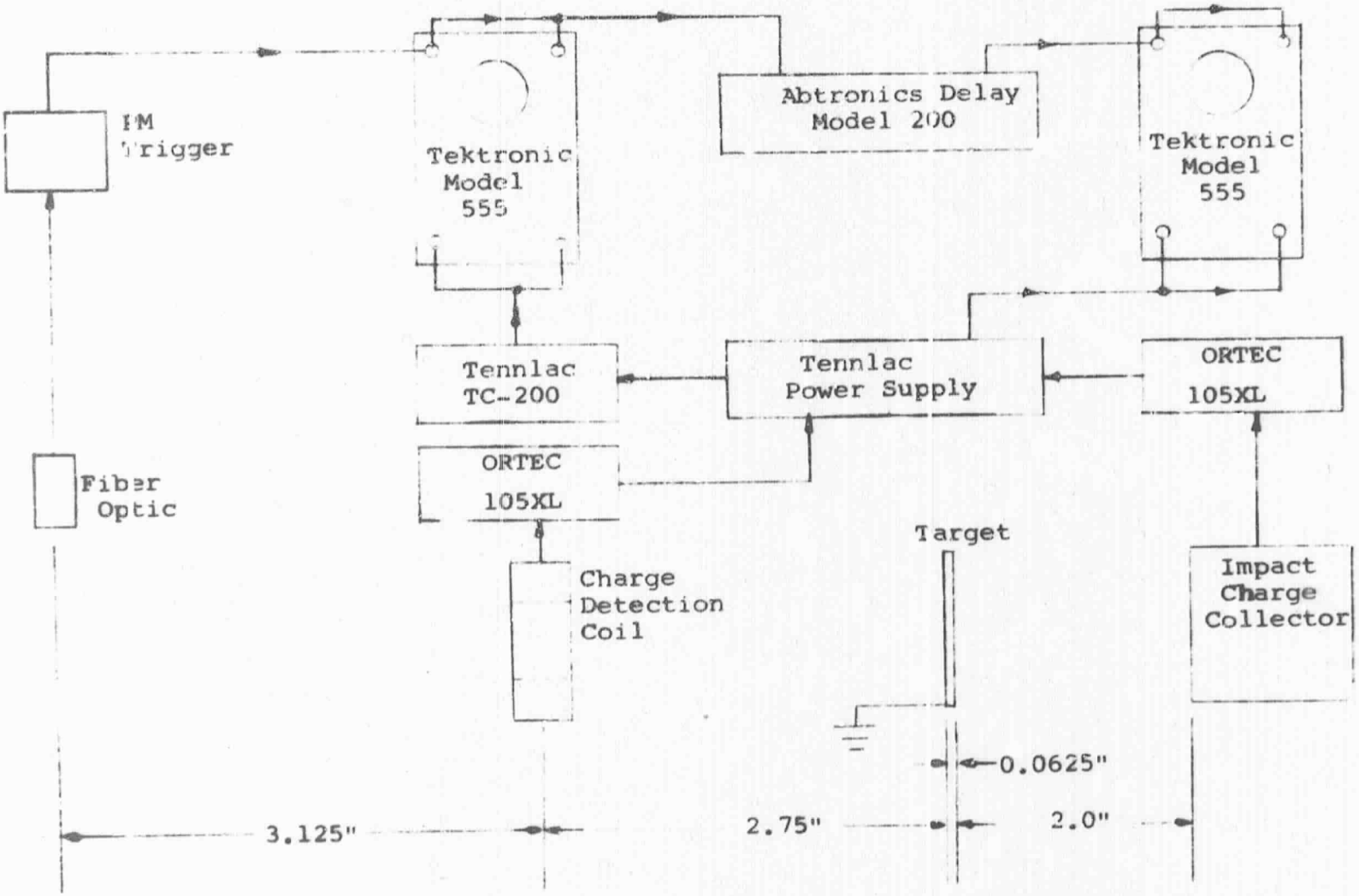

Figure 45 Charge Collection Instrumentation

Thus, we rather arbitrarily selected values for the first riring, and improved these as data were obtained.

An oscilloscope trace of the first particle charge experiment is shown in Figure 46. Both top and bottom traces indicate that the signal begins some 18 to 19 μsec after the primary PM tube trigger, a figure in agreement with the anticipated projectile velocity. Though the signal went off-scale, an extrapolation of the lower trace indicates the projectile had a charge of $\sim 9 \times 10^{-14}$ coulomb. The second and third experiments failed to produce any results, the former because a modification in the fiber optic aperture resulted in a trigger failure, and the latter due to what appeared to be an excessive amount of induced noise. Data could not be evaluated in either case. The final two experiments produced data indicating a projectile charge of nearly 7×10^{-13} coulomb.

The first of the five experiments, in which a 1/8-in. target was used, indicated a charge of 5.3×10^{-13} coulomb was produced by the impact (Figure 47). This charge was collected using a 2-in.-diameter flat disk grid biased at 100 volts. Subsequent experiments were either not instrumented for impact collection or resulted in signals which were off-scale at the detector.

It was found that an electrical charge is apparently produced by high speed ($\approx 2 \times 10^4$ fps) aluminum projectiles impacting on thin aluminum targets. To make the best possible quantitative measurements, a coil was used to determine the charge on the projectile prior to impact and a set of electrically biased collectors were placed downstream of the target to determine the total charge present immediately after impact. Since no previous quantitative results have been obtained for this sort of event and because of a very limited theoretical basis, instrumental gain and sensitivity adjustments were made rather arbitrarily at the outset of the work. The signal strength was generally larger than anticipated for the series of four or five events monitored, so that a very modest amount of data has been obtained.

The data that have been obtained for the projectile measurements indicate that a net charge of $\sim 10^{-13}$ coulomb is present prior to impact. For the one case where both projectile and impact charge was measured, the results were 0.9×10^{-13} and 5.3×10^{-13} coulomb respectively. This suggests that a little less than 20 per cent of the total charge generated at impact may be brought to the collision location by the projectile.

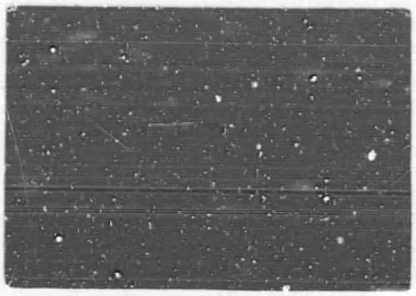

Time

Top Trace: Vertical Sensitivity = 0.5 volt/cm
Horizontal Sweep = 2 μsec

Bottom Trace: Vertical Sensitivity = 100 mv/cm
Horizontal Sweep = 5 μsec

Figure 46 Projectile Charge Impulse

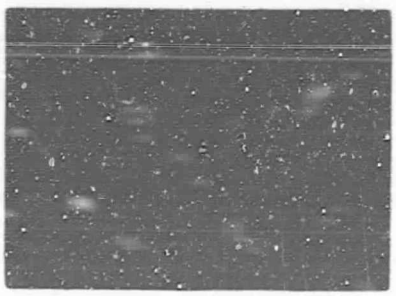

Time

Vertical Sensitivity = 0.5 volt/cm
Horizontal Sweep = 2 μsec

Figure 47 Charge Collector Impulse

Much more work is obviously needed to construct a meaningful model for events of this kind. An effort should probably be made to determine the dependence of charge magnitude on projectile velocity and projectile and/or target material. A brief analysis should also be made to correlate our projectile charge determinations with models of projectiles and their shock waves moving through the atmosphere. Of even more importance, perhaps, is a determination of the effect of spray or ejecta on charge collection measurements made downstream of a thin target. Additional high-speed photography should be most useful in this regard.

Summary of Phase III Experiments. - Phase III experiments have been completed with a high degree of success on various measurements desired by NASA. Reduction of the data has been completed and is presented in detail for each of the specific areas. The experiments were set up and conducted in three parts including some tests with supplementary instrumentation furnished by NASA.

Part 1, Normal Impact with Disk Projectile

To obtain normal impacts at the target with a disk type projectile, several methods of launching the projectile were investigated. Sabot and full caliber projectiles were included in both smooth bore and rifled launch tubes. A normal impact with a 3/16-in.-diameter half-caliber-long projectile was obtained. Launching the projectile from a rifled tube provided adequate stability. Verification of the projectile attitude was obtained with two image-converter cameras along the flight path.

Part 2, Bubble Growth (Photographic and Radiographic Measurement)

Sequential flash X-rays were obtained on the bubble growth for both 1/8- and 1/16-in.-thick targets. A single exposure of the bubble was obtained with the image converter back-lighted for both 1/8- and 1/16-in.-thick targets. Self-illuminated exposures were made but failed in obtaining a picture of the bubble. In the additional tests made with NASA's TRW image converter framing camera, a picture of the bubble by self-illumination was obtained.

Part 3. Ionization Measurements

Ionization measurements were made in a specially designed high-vacuum chamber at a pressure of between 2.5 - 4 x 10^{-5} torr. Data were obtained for both 1/8- and 1/16-in.-thick targets. The following type measurements were made in these experiments.

- The charge on the projectile prior to impact on the target.
- The charge resulting from the ionization associated with the bubble on the rear face of the target.
- Total integrated light from the bubble.
- Spectraldata recorded on film, and recorded for specific band passes monitored by photomultiplier tubes.

However, color temperature determination was not made because time did not permit obtaining the required spectral data for this effort.

Table XIX shows the firing summary, round by round, for Phase III. A total of eight firings was made to establish a stable-flying, flat-disk type projectile. Four additional rounds were then fired to set up a sabot catcher plate ahead of the velocity station. Rounds 13 through 30 were then fired to obtain data for parts 2 and 3 of this phase.

TABLE XIX

PHASE III FIRING SUMMARY

Round	Projectile	Target	Velocity (fps)	Instrumentation Coverage	Remarks
1	.050" dia. .020" thick Al (sabot)	1/2" Al	21,900	Vel. back-up with image converter	Check for normal impact - projectile not stable
2	.220" dia. .103" thick 2024-T4 Al (no sabot)	1" Al	20,000	Vel. with image converter	Check for normal impact pretriggered image converter camera - no picture of projectile
3	.220" dia. .103" thick 1100 Al (no sabot)	1" Al	20,000	Vel. with image converter	Same as above
4	.220" dia. .103" thick 1100 Al (no sabot)	1" Al	20,000	Vel. with image converter	Same as above
5	.220" dia. .103" thick 1100 Al (no sabot)	.032" Al	20,000	Vel. with image converter	Same as above
6	.220 dia. .103" thick 1100 Al + .220" dia. .110 thick Poly	.032" Al	17,000	Vel. with image converter	Poly disk behind Al disk-Image converter camera showed deformed projectile

TABLE XIX (Continued)

Round	Projectile	Target	Velocity (fps)	Instrumentation Coverage	Remarks
7	.220" dia. .110" thick 2024-T4 Al (no sabot)	.041" Al	17,000	Vel. with image converter	Projectile yawed and was deformed in launch
8	3/16" dia. 3/32" thick 2024 T4 Al (sabot)	.125" Al	19,000	Vel. with image converter	Projectile stable at 1st I.C. station - missed at 2nd - pcs of sabot impacted on target
9	3/16" dia. 3/32" thick 1100 Al (sabot)	.125" Al	20,000	Vel. with image converter	Projectile intact and stable
10	3/16" dia. 3/32" thick 1100 Al (sabot)	1/2" Al*	---	---	*Target located 3' from muzzle to establish location of sabot catcher plate Sabot pattern too tight at this location
11	3/16" dia. 3/32" thick 1100 Al (sabot)	1/2" Al*	---	---	Target located 7' - 9" from muzzle - sabot separation good
12	3/16" dia. 3/32" thick 1100 Al (sabot)	1/2" Al	20,000	Vel. with image converter	Located catcher plate with snorkel at impact point from above test & located target to determine impact point in test chamber

TABLE XIX (Continued)

Round	Projectile	Target	Velocity (fps)	Instrumentation Coverage	Remarks
13	3/16" dia. 3/32" thick 1100 Al (sabot)	1/8" 1100 Al	20,000	Vel. with image converter and X-ray	Good X-ray - poor detail on leading edge of bundle-missed I.C. picture of projectile
14	3/16" dia. 3/32" thick 1100 Al (sabot)	1/8" 1100 Al	20,000	Vel. with image converter and X-ray	Good X-ray data and stable projectile at I.C. stations
15	3/16" dia. 3/32" thick 1100 Al (sabot)	1/8" 1100 Al	20,000	Vel. with image converter and X-ray	X-rays indicated projectile yawed at impact - I.C. pretriggered on sabot impact at catcher plate
16	3/16" dia. 3/32" thick 1100 Al (sabot)	1/8" * 1100 Al	20,000	Vel. with image converter	*Target located at 2nd I.C. - good back lighted picture of bubble at 6μsec delay
17	3/16" dia. 3/32" thick 1100 Al (sabot)	1/8" * 1100 Al	20,000	Vel. with image converter	*Target located at 2nd I.C. failed to obtain self illuminated picture of bubble at 6μsec delay
18	3/16" dia. 3/32" thick 1100 Al (sabot)	1" Al *	---	Alignment test for reworked gun tube	*At catcher plate location entrance on launch tube damaged on previous test - required rework

TABLE XIX (Continued)

Round	Projectile	Target	Velocity (fps)	Instrumentation Coverage	Remarks
19	3/16" dia. 3/32" thick 1100 Al (sabot)	1/8" Al*	21,000	Vel. with image converter	Added sabot catcher plate assembly & obtained impact point to locate target assembly in high vacuum chamber
20	3/16" dia. 3/32" thick 1100 Al (sabot)	1/8" 1100 Al	20,000	Vel. with image converter charge collection impact flash (PM)	1st test in high vac chamber missed 1st I.C. picture - unit failed - good impact on target & data
21	3/16" dia. 3/32" thick 1100 Al (sabot)	1/8" 1100 Al	20,000	Vel. with image converter charge collection impact flash	Good impact & data
22	3/16" dia. 3/32" thick 1100 Al (sabot)	1/16" * 1100 Al	21,000	Vel. with image converter charge collection TRW framing camera EG & G flash (PM)	Good impact on target - 3 pictures on framing camera appear to be late. *Change target thickness
23	3/16" dia. 3/32" thick 1100 Al (sabot)	1/16" 1100 Al	20,000	Vel. with image converter TRW framing camera EG & G flash (PM)	Good picture of bubble on one frame of framing camera
24	3/16" dia. 3/32" thick 1100 Al (sabot)	1/16" 1100 Al	17,600	Vel. with image converter TRW framing camera impact flash	Framing camera & PM on impact flash pretriggered

TABLE XIX (Continued)

Round	Projectile	Target	Velocity (fps)	Instrumentation Coverage	Remarks
25	3/16" dia. 3/32" thick 1100 Al (sabot)	1/16" * 1100 Al	17,500	Vel. with image converter	*Target at 2nd I.C. - low flight path only upper portion of bubble obtained at 6μsec delay
26	3/16" dia. 3/32" thick 1100 Al (sabot)	1/16" *	---	Vel. with image converter	*Target at 2nd I.C. attempted to raise flight path by shimmying up gun tube & catcher plate assembly, projectile hit catcher plate
27	3/16" dia. 3/32" thick 1100 Al (sabot)	1/16" 1100 Al	20,500	Vel. with image converter flash X-ray toroid coil	4 X-rays obtained only on good record at 6μsec delay
28	3/16" dia. 3/32" thick 1100 Al (sabot)	1/16" 1100 Al	20,500	Vel. with image converter flash X-ray toroid coil	4 good X-rays of bubble growth
29	3/16" dia. 3/32" thick 1100 Al (sabot)	1/16" 1100 Al	20,500	Vel. with I.C. chge measurement spectro integrated light & self-initiated I.C. test	Projectile deflected and missed target
30	3/16" dia. 3/32" thick 1100 Al (sabot)	1/16" 1100 Al	21,000	Same as above	Good hit & data missed bubble with I.C. camera